Optimal Utilization of Neural Representations for Brain-Computer Interfacing

An investigation into candidate brain regions, brain functions
and signal features

Max van den Boom

Optimal Utilization of Neural Representations for Brain-Computer Interfacing

An investigation into candidate brain regions, brain functions
and signal features

Optimale Benutting van Neurale Representaties ten behoeve van Brain-Computer Interfacing

Een onderzoek naar kandidaat hersengebieden, hersenfuncties
en signaaleigenschappen

(met een samenvatting in het Nederlands)

Proefschrift

ter verkrijging van de graad van doctor aan de Universiteit Utrecht op gezag van de
rector magnificus, prof. dr. H.R.B.M. Kummeling, ingevolge het besluit van het college
voor promoties in het openbaar te verdedigen op maandag 20 juni 2022 des ochtends
te 10.15 uur

door

Max Alexander van den Boom

geboren op 17 augustus 1984
te Breda

Contents

Chapter 1

Introduction

Even in the most futuristic science-fiction, people tend to talk to computers much like we currently command our voice assistants; but surely humankind can do better! Why not interface directly with the brain?! The field of Brain-Computer Interfaces (BCI), although still in its infancy, attempts to achieve exactly that: to have a machine directly interpret the neuronal signals from the brain in order to utilize mental intent or brain states and control the world around us.

The first steps in this direction have already been made, both in knowledge and as proofs-of-concept. Examples include, but are not limited to, controlling an effector like a robotic arm or cursor on a screen using brain activity, or "deciphering" what is visually perceived from brain activity. Unfortunately, many such brain interfaces are not yet reliable enough, offer limited control, and are restricted to patients in a clinical or research setting for technical and ethical reasons. Should BCIs develop further — and potentially beyond use by patients alone — we could operate a computer, phone, car or drone with intentive thoughts, as natural and automatic as we currently exert manual or voice control. Even "reading" a mental image to convey a view or graphical design could belong to the possibilities, efficiently conveying complex information as "a picture is worth more than a thousand words". And so, much progress is still to be made.

1.1 Interfacing with brain activity

When interfacing with the human brain, we need to consider: (1) the technique with which brain activity is measured, (2) the brain function used to generate interpretable brain activity, and (3) the brain areas that are most involved when using a brain function, so where the most informative brain activity is located. Although not exhaustive, this section will mention the techniques, brain functions and brain areas that are currently the most relevant in the field of BCI and relate to my research.

Measurement techniques

Several techniques can be used to measure and digitize the activity from the human brain. Some of the most common techniques are functional Magnetic Resonance Imaging (fMRI), Magnetoencephalography (MEG), Electroencephalography (EEG), Electrocorticography (ECoG), Stereo-electroencephalography (SEEG) and microelectrode arrays (MEAs). While most of these techniques are well suited for research towards brain interfacing, only very few options are sensible when it comes to practical implementation and realistic daily use of a BCI. My research focuses on ECoG and fMRI for reasons explained in the following paragraphs.

ECoG has been proposed as one of the most suitable measurement techniques for a BCI solution to a patient at home. ECoG measurements come from strips or grids of electrodes placed subdurally or epidurally on the brain surface. Typical ECoG electrodes have an exposed diameter of a few millimeters, where each electrode measures the combined electrical potential from the ensembles of neurons underneath, providing a relatively direct measurement of brain activity. From a clinical perspective, permanent ECoG implants are aesthetically pleasing because the electrodes are placed underneath the skull with a small amplifier and transmitter device can be embedded within the chest or on the skull underneath the skin. Moreover, the signals are of exceptional quality and are reliable over an extended period [1,2], have less of an inverse problem, and require very little time to set up or calibrate. From a technical perspective, ECoG has the advantage of a high temporal resolution and can — depending on the ECoG electrode array that is used — have a good spatial resolution. In particular the direct high temporal resolution measurement of neuronal activity allows for the extraction of features (e.g. different frequency bands amplitudes) that provide reliable input to a BCI. Specifically changes in the high-frequency band (HFB; > 65Hz) power are understood to reflect the underlying firing of local neuron populations [3–7] and have shown to be highly informative for motor representations in the sensorimotor cortex [8–15]. The disadvantage of ECoG is that it is an invasive technique and therefore requires brain surgery. As a result, ECoG measurements are limited to a clinical or patient setting with comparatively little opportunity to answer fundamental questions on a broader range of brain functions, brain areas, and their properties for exploitation in a BCI.

In contrast to ECoG, fMRI is non-invasive, can capture the whole brain, is safe and widely used, and over recent decades has provided a large quantity of information on the workings of several brain functions [16]. fMRI measurements are made in an MRI scanner and rely on changes in oxygenation and blood volume in the cortical microvasculature [17,18], which in turn are driven by neurovascular coupling (i.e. regional changes in blood flow and oxygen consumption following local neural and glial activity). Due to the differential magnetic properties of oxyhemoglobin versus deoxyhemoglobin, these local haemodynamic responses and the concentration of deoxyhemoglobin during task performance can be quantified in a so-called Blood Oxygenation Level Dependent (BOLD) signal. fMRI is capable of reliably capturing activity over the entire brain at a high spatial resolution (on the scale of mm) but, being dependent on the relatively slow haemodynamic response, has a poor temporal resolution (on the scale of seconds). Owing to the low temporal resolution and non-portability, fMRI is not a realistic candidate for a practical everyday BCI. However, much of the (fundamental) research on brain activity in fMRI has shown to be a good approximation of ECoG measurements.

The electrophysiology measured in ECoG and the BOLD signal changes in fMRI have shown to be correlated both temporally [19,20] and spatially given the matching of HFB power and BOLD on peak activity [13,21–24], successful prediction of non-linearities in BOLD based on HFB power [25] and matching increases of BOLD response and HFB power across conditions [26–28]. As such, the research on brain functions and the properties of the brain signals in fMRI

research can be, and are, utilized in ECoG-based BCIs. For example, fMRI is used pre-operatively in patients with amyotrophic lateral sclerosis (ALS) or paraplegia to localize the functional region of interest (ROI) and placement of electrodes in and on the sensorimotor cortex [1,29–31].

I focus on fMRI and ECoG because I believe these techniques are complementary in the development of BCIs, such that fMRI allows me to investigate the utilization of brain functions, brain areas and their features for use in an ECoG-based BCI. Other techniques have their own advantages in different settings, which I will briefly mention to sketch a more general field of BCI. Scalp-EEG, for example, while safer than implanted electrodes, has a low spatial resolution, a low signal-to-noise ratio, is susceptible to signal contamination and requires much effort and time to be set up by a caregiver before each use. Despite minor improvements in spatial resolution and attempts to provide a home BCI using flickering screens and P300 error potentials [32], this technique has limited utility for a practical BCI and has little to no adoption by the medical BCI field. Another technique worth mentioning is the use of intracortical MEAs (also known as micro-electrodes, micro-arrays or Utah arrays), where an array of tiny needles is pushed into a small piece of the cortex. By doing so, sites along the needles or at the needle tips can measure extracellular action potentials from neurons, providing information at a very high spatial and temporal resolution. However, the movement of electrode sites relative to neurons results in a daily or sometimes even hourly need for recalibration. In addition, the loss of detected action potentials, impedance [33,34] and amplitude [35–37] over time due to material degradation or tissue reactions cause the quality of BCI control to degrade gradually [38,39], rending the period of usability short. Therefore this measurement technique is less suited for a sustainable everyday BCI. Still, research using intracortical MEAs is often aimed towards BCI applications and has led to many valuable insights and proofs-of-concept [29,30,40–48].

Brain functions and regions

A number of brain functions would allow for voluntary control, where brain signals can be deliberately regulated to provide interpretable and utilizable input to a BCI. Research has been done mainly on (the properties of) brain activity associated with the sensorimotor system, executive cognitive functions, auditory representations and the visual system. Although multiple brain functions could be used simultaneously to control a BCI, most research focuses on a single brain function. Using multiple brain functions could have several benefits, one of which is to provide alternative options of control over a BCI or increase the degrees of freedom of a BCI (extending from 1D to 2D or more). Another benefit may be to prevent false positives during the use of other brain functions.

The sensorimotor system is — by far — the most extensively researched and used brain system for brain-computer interfacing. This choice is motivated by a number of reasons: First, the primary motor area (M1) and primary sensory area (S1) offer a topographical representation of the body [49]. Second, particularly in ECoG, sensorimotor areas are often covered with electrodes for clinical purposes during (epilepsy) surgery. Third, only very little

co-activity related to other brain functions (such as the working memory or visual system) occurs in the sensorimotor cortex.

Since sensorimotor areas are largely dedicated to the voluntary movement and sensory input of specific body parts [49], we can easily distinguish and utilize the neural activity generated by the voluntary movement of those different body parts. Due to their relatively large representation within the sensorimotor cortex, two functional brain areas in particular stand out as a target for BCI research and utilization: (1) the hand/arm sensorimotor areas associated with finger/hand/arm movement or imagery [15,42,50], and (2) the mouth/face sensorimotor areas associated with executed or imaged articulator movements [51–54].

An alternative, primary and extensively investigated system is the visual system. Most research on the visual system naturally focuses on visual input and the processing thereof. The visual system is typically bottom-up driven and the brain activity is less voluntarily controlled. However, the act of mental visual imagery can be voluntary and its cortical activity has shown to be interpretable for low-level features such as motion [55], orientation [56–58], location [59] and shape [60,61]. Like the motor system, early visual areas have a specific mapping and are retinotopically organized [62–65]. This retinotopic organization may allow for the extraction of distinct neural activity related to different spatial areas of the visual field, making it possible to control a BCI. Interestingly, almost all patients who have lost or are losing their ability to speak (e.g. people with locked-in syndrome) already use computerized eye-tracking to spell characters and speak words or sentences. Given the widespread use by patients and the full dedication of the eyes for communication, the utilization of mental imagery could be a fast and more intuitive alternative.

Higher cognitive functions are seldom used directly to control a BCI. Such functions are often too complex, involve multiple (subcortical) brain areas and/or can be difficult to control voluntarily. While these factors apply to the cognitive function of working memory as well, some working memory areas can still be considered. The left dorsolateral prefrontal cortex (DLPFC) is an area that is involved in mental manipulations in human working memory. Interestingly, activity in the DLPFC can be voluntarily regulated [66,67] and therefore provides for a degree of control (i.e. less or more activity depending on the mental effort). As such, working memory activity could be utilized to control a BCI, either as an input signal directly (in ECoG [67,68]) or indirectly to prevent false positives. As of now, at least two patients are known to have permanent brain implants that cover the DLPFC with the purpose of BCI [1,68]. Studies with these patients confirm that a high degree of DLPFC-based control is possible, with participants reporting it as less tiring and requiring less mental effort than sensorimotor-based control [68], and that the DLPFC can provide a usable error-related potential [69].

1.2 BCI applications

Types of BCI control

The measurements from the brain, either the electrical potentials in ECoG or the oxygen levels in fMRI, can serve as the input needed to control a BCI application. Spatial, temporal and/or spatiotemporal features are extracted from the raw measurements, so that irrelevant input (noise) is reduced to a minimum and the most relevant input (signal) remains. The relevant — and in most cases voluntary regulated — features can then be utilized in a variety of ways.

One type of control translates input feature(s) to continuous output control, where the incoming feature(s) results in a value on a scale or dimension (e.g. translate the degree of activity in a specific brain area to control the position of a cursor on the screen). Such an approach has been applied in several ECoG studies, in 2D reaching and pointing [70], 2D cursor trajectory [71,72], grasp aperture [73] and individual finger flexion [10,74,75]. A similar type of output converts a continuous value, based on a threshold, into a binary "on" or "off" value (e.g. a brain click is produced by imagining the movement of a paralyzed hand when the brain activity crosses a specific threshold [1]).

Yet another type of control takes the input features and, based on a (pre-trained) model, classifies it as a discrete output class (e.g. imagining a particular hand gesture produces a specific spatiotemporal activity pattern in the brain, which then is interpreted as a character to be spelled). One or more input features can control one or more dimensions, and different types of controls can be combined in a BCI to provide more reliable input and/or more degrees of freedom to control a BCI application.

It is worth mentioning that some generative decoding models (e.g. linear gaussian or convolution neural networks) are capable of producing, instead of just discrete output, output with a significant level of detail. For example, they can generate an image of what people see based on their brain activity [76-81]. Such models mainly involve advanced engineering and require large amounts of spatially detailed brain data to work, and are therefore almost exclusively in the domain of fMRI.

Current state-of-the-BCI

Based on the available brain functions, brain areas and techniques, several BCIs have already been realized in humans. Most BCIs are currently proofs-of-concept at a research location, while only very few are being applied in a home setting.

As described above (1.1), neural representations of hand and arm movements measured from sensorimotor areas are often used in BCIs. Since these BCIs target patients who have lost a limb (e.g. amputees) or their ability to control limbs (e.g. quadriplegics), it intuitively makes sense to restore these functionalities by providing a relay to the limb's muscles [43] or control over prosthetic limbs (e.g. a robotic arm or an exoskeleton [29,31,47,82]). While some patients may have remaining functionality in the periphery (spine, remaining part

of limb) that could be utilized, we focus on prosthesis controlled by signals measured from the brain. As an example, a recent study [31] implanted a patient with quadriplegia with two 64 electrode ECoG arrays over the upper-limb sensorimotor areas of both hemispheres. The patient performed various tasks, building from generating a single brain click (that would start a pre-programmed leg-walking sequence of the exoskeleton) towards 8-dimensional continuous control over the arms (four dimensions on each arm; x, y, z translation + wrist rotation). Another study [29] implanted a patient with two intracortical MEAs in the motor cortex of the hand, allowing for robust control of a robotic arm to perform reach-and-grasp movements. While fascinating and responsible for drawing me into the field of BCI, neuroprosthetic limbs that are controlled by brain signals are often limited to a research setting due to their current lack of mobility (e.g. a robotic arm is a large device standing next to a participant, to be used only in a research/hospital location).

Another broadly pursued type of BCI aims to facilitate communication by translating brain signals to letters, words, sentences and (generated) speech. Communication BCIs often target locked-in patients (LIS) who have lost or are losing their ability to speak, such as patients with ALS or brainstem stroke. These patients often rely on eye-tracking as their last means of communication with the outside world. By sequentially gazing at letters on a screen (i.e. a virtual keyboard), they spell words and sentences, which are then spoken aloud by assistive software. Communication BCIs can complement or in-time replace eye-tracker communication, and because they can be portable (e.g. a small receiver on the chest and a tablet computer to spell on), they are one of the few implanted BCIs that are used independently by patients at home [1,2] and therefore directly benefit the patient. The Utrecht NeuroProsthesis [1], a fully implanted communication BCI for which I programmed the signal translation and patient software, currently serves several locked-in patients at home by means of a permanent ECoG brain implant over the hand-knob area in the motor cortex. Other studies use multi-dimensional virtual keyboard control [41,42,45], decode (imagined) speech articulators (i.e. tongue, lip, jaw and larynx) [51,53,54,83–91], or envision a BCI that allows for communication by decoding (sign language) gestures [14,92–95]. While promising, these efforts either require further development, have not been deployed in a home setting, or cannot yet be used independently for daily activities.

1.3 Outline of this thesis

The research presented in this thesis pursues the advancement of BCIs by exploring the optimal utilization of controlled brain activity in a variety of directions.

Most research on the electrophysiological properties and decoding of hand movements has been done in patients with a healthy moving hand. At the same time, BCIs often aim towards helping long-term amputees or patients who no longer have control over their muscles (e.g. ALS or brainstem stroke). The question remains how much of the hand representation remains intact in these patient groups. In **Chapter 2,** we were presented with a unique opportunity to investigate the motor physiology of the brain in a patient with an amputated hand using ECoG and show that the physiology is retained even in attempted movement of non-existent fingers.

Chapter 3 deepens further into the utilization of sensorimotor representations and investigates how different resolutions/scales of neuronal measurement (i.e. ECoG electrode grid configurations) would influence the acquisition of optimal information for decoding hand gestures using fMRI. In addition, a data-driven method is presented to pre-operatively assist in finding the optimal grid configuration and placement on the cortex.

While the bulk of BCI research focuses on the sensorimotor system, visual mental imagery is an underexplored avenue in the context of controlling a BCI. **Chapter 4** investigates the decoding of visual imagery from the early visual cortex and the properties of prolonged imagery using fMRI, exploring and evaluating the usability, opportunities and implications for visual imagery-driven BCIs.

Alternatively, DLPFC activity can be utilized for BCI-control, particularly in cases where motor cortex functioning is impaired due to stroke [96], injury [97], neurodegenerative disease [98,99], or when motor imagery is mentally too demanding [68]. However, in contrast to motor movement where brain activity is generated "automatically" by an intention to move limbs or otherwise contract muscles, working memory activity can be less intuitive to produce voluntarily. Instead, specialized tasks are often used to generate and control brain activity (e.g. counting backward in steps of 7). Suppose a BCI would rely on such a cognitive function and specific task for direct control, then there is the risk of a practice effect, meaning the automatization of cognitive processing over time [100,101]. A shift from controlled to automatic cognitive processing on a task could lead to less activity, resulting in less reliable control of a BCI. We hypothesize that continuous closed-loop feedback on brain activity could prevent this from happening. **Chapter 5** explores the degree to which we can voluntarily self-regulate brain activity when provided with closed-loop feedback on the left dorsolateral prefrontal cortex.

Taken together, these chapters contribute to the foundation of at-home BCIs with the potential to help patients.

Chapter 2

Chapter 2 - Typical somatomotor physiology of the hand is preserved in a patient with an amputated arm: An ECoG case study

Abstract

Electrophysiological signals in the human motor system may change in different ways after deafferentation, with some studies emphasizing reorganization while others propose retained physiology. Understanding whether motor electrophysiology is retained over longer periods of time can be invaluable for patients with paralysis (e.g. ALS or brainstem stroke) when signals from sensorimotor areas may be used for communication or control over neural prosthetic devices. In addition, a maintained electrophysiology can potentially benefit the treatment of phantom limb pains through prolonged use of these signals in a brain-machine interface (BCI).

Here, we were presented with the unique opportunity to investigate the physiology of the sensorimotor cortex in a patient with an amputated arm using electrocorticographic (ECoG) measurements. While implanted with an ECoG grid for clinical evaluation of electrical stimulation for phantom limb pain, the patient performed attempted finger movements with the contralateral (lost) hand and executed finger movements with the ipsilateral (healthy) hand.

The electrophysiology of the sensorimotor cortex contralateral to the amputated hand remained very similar to that of hand movement in healthy people, with a spatially focused increase of high-frequency band (65–175 Hz; HFB) power over the hand region and a distributed decrease in low-frequency band (15–28 Hz; LFB) power. The representation of the three different fingers (thumb, index and little) remained intact and HFB patterns could be decoded using support vector learning at single-trial classification accuracies of >90%, based on the first 1–3 s of the HFB response.

These results indicate that hand representations are largely retained in the motor cortex. The intact physiological response of the amputated hand, the high distinguishability of the fingers and fast temporal peak are encouraging for neural prosthetic devices that target the sensorimotor cortex.

2.1 Introduction

Deafferentation from the loss of a limb affects the inputs and outputs to and from sensorimotor areas in the brain. However, it is not yet clear what happens to the physiology of these cortical regions when a limb is amputated. Using electrocorticography (ECoG) measurements in humans, it has been well established that hand movements cause a spatially focal increase in high frequency amplitude in the sensorimotor cortex and a spatially distributed decrease in low frequency amplitude [3–5,22]. Furthermore, the individual finger movements can be distinguished topographically using the high frequency signals [9,13]. It is unknown whether these basic physiological changes are maintained after the amputation of a limb.

Several studies have reported that sensorimotor areas reorganize after amputation in humans using transcranial magnetic stimulation [102,103] and fMRI [104–106], and in macaque monkeys using electrical stimulation [107] or after lesioning [108]. These studies suggest that areas previously related to the amputated limb can associate with other muscle groups. However, there are several fMRI studies on upper arm amputations that show that some form of hand [106,109–111] and finger [112,113] representation are preserved in both the motor and sensory cortex, even over longer periods of time. In addition, sensory representations of the hand have been shown to be preserved in patients with tetraplegia using microstimulation of the somatosensory cortex [114,115] and EEG studies have shown that ERP responses related to motor inhibition remain intact [116].

Preserved motor physiology would be invaluable for specific clinical purposes such as Brain Computer Interfacing (BCI). Using BCIs, people with paralyses can use the electrophysiological signal from the brain, generated by attempted hand movement, to control communication devices [1] or other assistive devices [31]. Furthermore, establishing BCI control could potentially help reduce phantom limb-pain [117], it is therefore important to understand the extent to which motor physiology is preserved.

In this study we were provided with a unique opportunity to investigate sensorimotor physiology with ECoG measurements in a patient with an amputated arm. The patient was implanted with an ECoG array for clinical evaluation of phantom limb pain and we measured ECoG signals during attempted finger movements of the contralateral, lost, hand. We investigated whether the typical spatiotemporal organization of hand-movement physiology was preserved and whether information of separate finger representations was retained.

2.2 Methods

Participant

A 62-year-old male with a left above-elbow amputation secondary to a snowmobile accident underwent temporary placement of a subdural electrode array for a trial treatment of phantom limb pain by electrical subdural cortical stimulation [118]. Experimental data were collected during breaks in trials of different electrical stimulation parameters over a period of 10 days.

The patient was righthanded and had his left-arm amputated 3 years and 11 months before ECoG grid implantation. The patient reported waking from his initial left mid-forearm amputation with phantom arm and hand pain, and that his pain has persisted since that time. He underwent two additional surgeries, ultimately completing a shoulder disarticulation and full humeral amputation. His pain has resulted in functional impairment and reduced quality of life despite trials of opiate medications, mirror therapy, an intensive pain rehabilitation program, and treatment with an implanted spinal cord stimulator. After the monitoring period, the patient was equipped with a cortical stimulator. At a six months follow up, he reported that the phantom limb pain dropped from 8 to 9/10 severity to a typical range of 5–6/10, and no side effects were reported.

The study was approved by the Institutional Review Board of Mayo Clinic (IRB 15-006530) and the patient provided informed consent to participate in the study, in accordance with the declaration of Helsinki (2013).

Recordings

An electrode array of 36 circular platinum contacts (AdTech, 6 × 6 electrodes, 2.3 mm exposed diameter, 10 mm inter-electrode distance) embedded in a silastic sheet was surgically placed over the frontoparietal region, including the sensorimotor cortex (figure 1A). Electrodes were localized using a high-resolution CT-scan and projected (Hermes et al., 2010) onto a cortical surface rendering generated from the preoperative anatomical T1 weighted MRI scan (GE 3T Discovery). During recording, all electrodes were referenced to an inactive subgaleal electrode with the recording surface facing away from the brain. The signals were amplified and digitalized at 2048 Hz. Upon inspection of the electrode signals, two channels that contained severe noise were excluded from analysis.

Tasks

The subject was presented with two tasks: an attempted and executed movement task. During the attempted movement task, the subject was asked to attempt finger movements with the (left, contralateral) amputated hand; During the executed movement task the subject was asked to perform finger movement with the (right, ipsilateral) hand on the healthy arm. Both tasks featured the exact same design with 5 s of finger movement and 3 s of rest. The subject was cued via a bedside monitor with a picture of a hand and asked to (attempt to) move one of three fingers: the thumb, index or little finger. Finger movement involved the repeated flexion and extension of the cued finger for the duration of the trial, while no specific instruction was given in regard to the speed of the movement. Each run of a task featured 15 movement cues for each finger, which were presented at random, resulting in 45 randomized trials per run. The subject performed two runs of attempted movement and two runs of executed movement.

Analysis

The analysis and classification routines were implemented using custom MATLAB (Mathworks inc.) code that is provided alongside this article at: https://osf.io/vmxdn/. Before analysis, the two runs of each task were concatenated and a small number of trials, that showed large artifacts in the signal or in which the patient was distracted, were excluded (2 trials were excluded for attempted movement and 4 trials were excluded for executed movement). The data were re-referenced to the common average by regressing the common average out from each channel.

Since hand and finger movements are known to be controlled by the contralateral hemisphere, the focus of our analyses is mainly on the attempted/phantom movements. However, because there is research that shows that ipsilateral activity does occur during unilateral movement of the hand [119-123] and ipsilateral representations may become more apparent after deafferentation [124], we have - for the sake of completeness - also performed analyses on the ipsilateral executed movements. Furthermore, the behavioral measurements on the intact hand provide a reference for the performance of the invisible hand.

Spectral power change

The contralateral power changes during attempted hand movement were investigated by extracting an epoch of 1–4 s after cue onset as movement. During executed movement (ipsilateral), the movement epoch was set to start 100 ms before the actual movement of the healthy hand to the end of the actual hand movement based on the concurrent video; 100 ms was subtracted to account for the delay between the cortical signal and initiation of the movement [9,125,126]. An epoch of 2 s before cue onset was considered as rest in both attempted and executed movements. The power spectral density of each epoch was calculated every 1 Hz by Welch's method [127] with a 250 ms window and an overlap of 125 ms. A Hann window [128] was applied to each epoch to attenuate the edge effects. Per channel, the resulting power spectra were log10 transformed and normalized to the mean power over all epochs at each frequency. Based on previous ECoG studies into executed and attempted movement we expected frequencies below 30 Hz and above 65 Hz to be most informative [5,9–13,22,93,129]. The high frequency band (HFB) power was obtained by calculating the average power over 65 Hz to 175 Hz, whereas low frequency band (LFB) power was the average over 15 Hz to 28 Hz. The alpha range (8–13 Hz) has been included in supplementary figure 1 for the sake of completeness.

In order to plot the spectral power changes on the rendered brain surface, we calculated the T-statistics for both the HBF and the LFB per channel by testing the power of movement trials against the rest trials. A Bonferroni correction was applied while testing the T-values for significance ($p < .05$).

To visualize the electrophysiological response over time, we filtered each electrode signal using a third-order Butterworth filter for either the high frequencies (HFB, 65–175 Hz), or the low frequencies (LFB, 15–28 Hz). After filtering, the power of the amplitude was

calculated using a Hilbert transformation. Trial-epochs, of 2 s before to 7 s after cue onset, were extracted and normalized by subtracting the signal mean power of the 2 s before cue onset from each individual trial. An average across each condition was calculated and smoothed with a moving average window of 1 s.

Temporal window for finger movement classification

In order to investigate to what degree spatial finger-representations were preserved and distinguishable, single-trial classification was performed on the individual fingers. For executed hand movement, we used the signal when the patient was moving the finger on the healthy hand. However, during attempted finger-movement there is no external behavioral measurement available to assess when (after cue onset) the patient started to attempt the movements, where in time the strongest decodable response occurs and whether such a response is transient or sustained. In order to address these factors, we split the data in two halves. One half was used to explore decodability of the response over time and find the optimal time-window parameters for decoding. Next, these time-window parameters were used in the other half for further decoding analysis. The data was split at random after concatenating the attempted movement runs, while balancing the finger conditions evenly over the two halves. Details on the classification procedure can be found below (under "Classification"); the same procedure was used on both halves of the data.

We explored the response over time and optimized it for decoding by applying several different time-windows while decoding the finger movement, thereby restricting the information available to the classifier. These time-windows differed in size from 250 ms to 5000 ms and in placement from cue onset, ranging from the beginning to the end of the trial.

An optimal time-window for classification was determined by first applying Gaussian smoothing to the classification accuracies over the window size (σ: 2.5) and offset (σ: 0.5) dimensions. Smoothing prevents the selection of parameters with local classification accuracy peaks in the parameter optimization half of the data, and allows for the selection of temporal parameters that are optimal in general. After smoothing, the time-window with the highest classification score was selected, and its offset and size were used for further classification analyses.

Classification

For classification, the HFB power of the different channels at the trial-epochs were used as features in a Support Vector Machine (SVM) with a linear kernel [130]. The HFB power was calculated per epoch in the same way as described above (i.e. using Welch's method, log10 transformed and averaged over 65–175 Hz), except that the spectra were not normalized. The unnormalized HFB power was used since the SVM maps each input feature to its own (scaled) dimension, and allows us to classify on the movement-epochs alone. We achieved multi-class classification (3 fingers) by applying a one-versus-all classification scheme in which every class is classified against the data of the other classes together and the winner

(that is furthest from the hyperplane) takes all. A leave-one-out cross validation was used and resulted in a classification accuracy score, which is the percentage of trials predicted correctly.

Comparisons to a significance threshold only apply to the half of the data that was used to further investigate the decodability, after applying the optimal time parameters. Classification scores were empirically tested for significance using a Monte Carlo distribution based on 100.000 permutations [131]. Estimates of the P values were obtained using the equation p = (r + 1)/(n + 1), where n is the number of simulations and r is the number of simulations that produce a classification accuracy greater than or equal to the actual classification accuracy [132].

Spatial analyses

Searchlight analyses were performed to establish which area on the cortex was most informative for attempted finger movement and how many electrodes (i.e. which grid configurations) would be needed to reliably classify the individual fingers.

The most informative cortical regions to decode attempted finger movements were identified using a random search procedure. During the random search procedure, a subset of 1–36 electrodes was selected at random to classify from. This procedure was repeated 10.000 times and, for each electrode, the average accuracy over all iterations was calculated and z-scored.

Searchlight analyses were performed to identify which anatomical scale of coverage would provide the most information for classification. During the searchlight analyses, a searchlight (i.e. a block of electrodes) was used for classification. The searchlight, with a fixed block size (e.g. 2 × 2 electrodes) was placed at every possible position within the grid. Afterwards, for each electrode, the average over all the iterations in which that particular electrode was involved was calculated. Searchlight analyses were performed with all possible searchlight sizes and shapes, representing grids of all different sizes (1 × 6/6 × 1–6 × 6 electrodes).

2.3 Results

A typical electrophysiological motor response occurred upon attempted movement

In order to investigate to what extent the sensorimotor cortex showed typical physiology after deafferentation, we measured ECoG responses in a patient with an amputated arm. The patient reported vivid movements of the amputated hand and could describe in clear fashion how well the different fingers moved during the task. Figure 1A and B show the electrophysiological differences between attempted movement of the missing hand and rest.
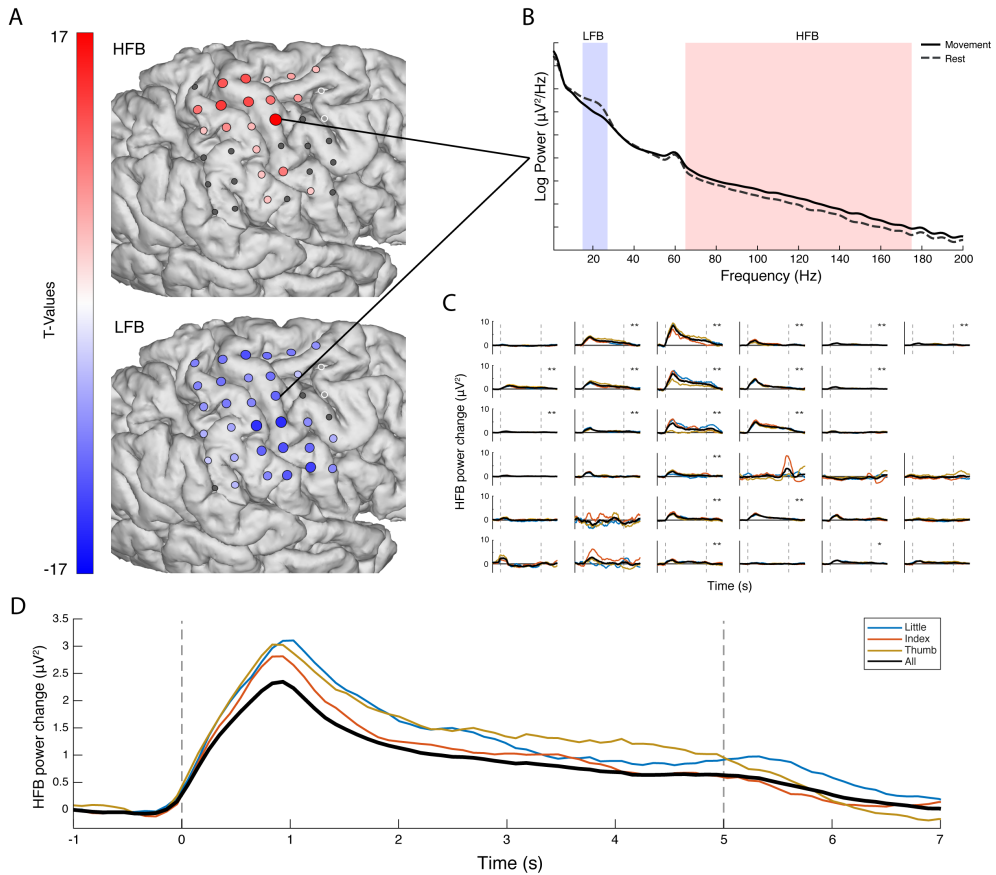
Figure 1. The electrophysiological response during attempted movement versus rest. (A). The changes in HFB (top, 65–175 Hz) and LFB (bottom, 15–28 Hz) for each grid electrode. Electrodes with a red or blue color had a significant change in band-power, whereas electrodes with an insignificant change in band-power are shown in grey; the two excluded electrodes are shown in white. (B) The power spectra of movement (solid line) and rest (dashed line) for a single electrode. (C) The HFB power changes over time, each graph represents one electrode. The black line represents all fingers, whereas the colored lines represent individual fingers. The two vertical dotted lines indicated the cue on- and offset. (D) The HFB power changes over time were averaged across those electrodes that showed a significant increase for a condition (blue: little, red: index, yellow: thumb, black: all fingers). The black trace has a lower amplitude because a different set of significant electrodes contributed to each trace, with more significant, but lower amplitude electrodes contributing to the black trace.

During attempted movement, a spatially distributed decrease of LFB power occurred in 91% of electrodes (t-test, $p_{corr.}$ < 0.05). Simultaneously, significant focal increases of HFB power were found in 56% of electrodes (t-test, $p_{corr.}$ < 0.05), most notably around the primary sensorimotor hand-areas. Strong decreases in power were observed in a narrow range of the lower frequencies (β band, 15–28 Hz), for completeness, supplementary figure 1 also illustrates the responses in the alpha range (8–13 Hz). High frequency power increases were

distributed over a broad range of higher frequencies (>65 Hz; figure 1B). During attempted movement there was no behavioral measurement available to determine when – after cue onset – the patient actually starts attempting the movement, nor where in time to expect the physiological response. Figure 1C and D present the changes in HFB power over time for each of the individual electrodes and the power averaged over all significant electrodes for each condition. A clear peak in HFB power is visible around 1 s second after the cue onset for all fingers.

Differential electrophysiological responses occur for the three individual fingers

Although each of the individual fingers provided a spatially different electrophysiological response, as shown in figure 2, it is difficult to distinguish a clear topographical order.
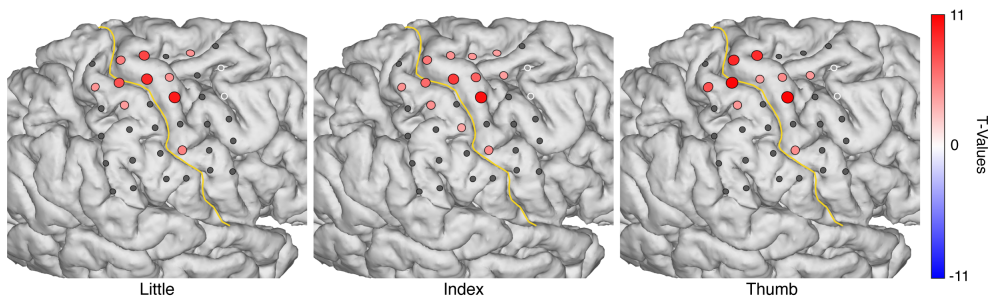
Figure 2. The HFB power changes upon attempted movement of each individual finger. Electrodes with a significant change in HFB band-power are shown in red, whereas electrodes with an insignificant HFB change are shown in grey, the two electrodes that were excluded are shown in white. The yellow line represents the central sulcus.

To investigate whether the representations of the individual fingers were preserved and sufficiently distinguishable we wanted to perform single-trial classification of the individual fingers. However, since there was no behavioral movement information available, we first needed to establish where in time the most information on attempted finger movement was present. By restricting the classification to the information within specific time-windows we could explore where in time the most information about attempted finger movement resided. Figure 3 shows the classification accuracies based on the HFB power within a specific window of time, ranging from 250 ms to 5000 ms, placing the window at different moments between the cue onset (t = 0 ms) and offset (t = 5000 ms).
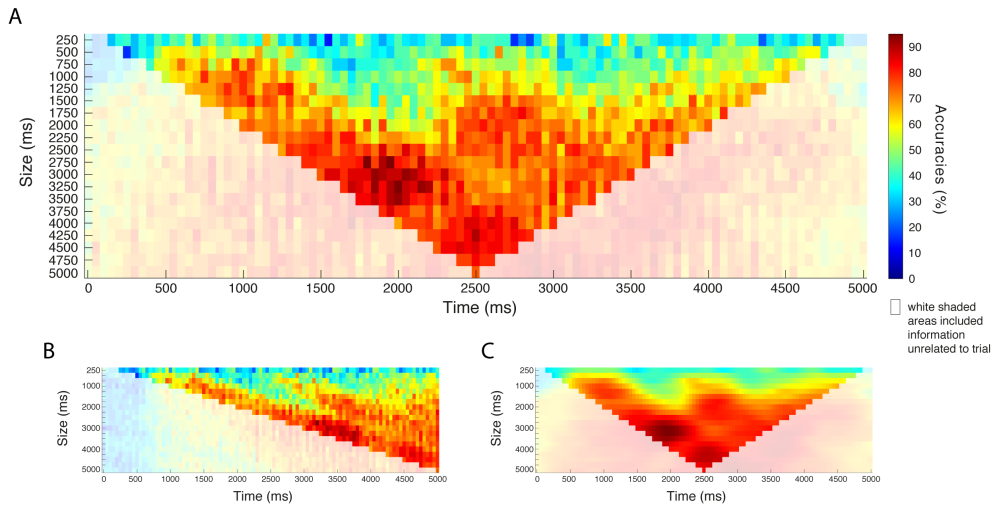
Figure 3. The classification accuracies at different window sizes (y-axes) and offsets from cue onset (x-axes), based on half of the data (~45 trials). (A) The x-axis indicates the center of each window. (B) The same plot shown, but with the x-axis indicating the right of each window, such that each time point includes the information present before that time. (C) Shows the classification accuracies smoothed with a Gaussian filter (offset σ: 0.5, size σ: 2.5). The white-shaded regions in each graph indicate the classification accuracies in which the window included information unrelated to the trial (i.e. rest before or after the trial).

Smaller time windows (<750 ms) seem to provide less good decoding accuracies (0-50%) in comparison to medium (750–2500 ms) or larger time-windows. Medium-sized windows can perform reasonably well (60-80%) depending on their offset in time. Window sizes of about 2500 ms to 5000 ms performed well overall (>~70%). In terms of window offset, the highest classifying windows take information from the beginning of the trial, regardless of window size. After Gaussian smoothing (figure 3C) of the classification results, the optimal window (i.e. the highest classification score) was found at a width of 3000 ms at 1950 ms (window center) after cue onset, which converts to an epoch window from 450 ms to 3450 ms after cue onset. The remainder of the results are based on this epoch and are performed on the half of the data that was not used for parameter optimization.

The second half of the data showed that the classification accuracy of attempted finger movements based on the spatial features of the HFB power was significant at 93% (above 45% chance level calculated with Monte-Carlo simulation; one-sided, p < .05). The sensitivity values for each of the individual fingers (Little: 87%, Index: 93% and Thumb: 100%), shown in figure 4, were also significantly above chance (one sided, each p < .05).

Figure 4. Confusion matrix with the classification scores of the individual fingers. Each column represents the finger of which movement was attempted. The rows represent how each of those finger movements was classified.

Topographical organization of attempted hand movement information

For all of the finger movements we investigated where on the cortex the related activity was located. Figures 1 and 2 already showed that most of the HFB power changes related to attempted movement occur around the hand and arm region of the pre and post central gyrus. Significant HFB changes extended beyond pre and post central gyrus to more anterior premotor regions as well. The random search classification results in figure 5C confirm that most information indeed resides in S1 and M1, specifically in areas of the pre and post central gyrus that are well known to represent hand and finger movements [49].

To test the spatial extent of finger movement information, searchlight analyses with different types of grid configurations were performed (figure 5A and B). Grid configurations with one or two electrodes tended to perform more poorly (~60%) compared to grids that include at least 3 electrodes (>60%). For electrodes strips (i.e. grids that have multiple electrodes only in one dimension), the orientation of the grid becomes important. Grids with 3–6 electrodes that are placed along the superior-inferior axis perform much better at >70% than grids are oriented on the anterior-posterior axis (at ~60%). This coincides with the topographical organization of the different fingers on the cortex, which is more superior-inferior oriented than anterior-posterior [9,13,133–135]. In accordance with the most informative area in figure 5C, grids perform best when 2–3 electrodes wide and at least 2–3 electrodes high, in order to cover enough area of the brain to include the most informative electrodes. Given the inter-electrode distance of 10 mm, the minimum required grid size to obtain a good (>=80%) classification would be around 13 mm × 13 mm (2 × 2 electrodes).
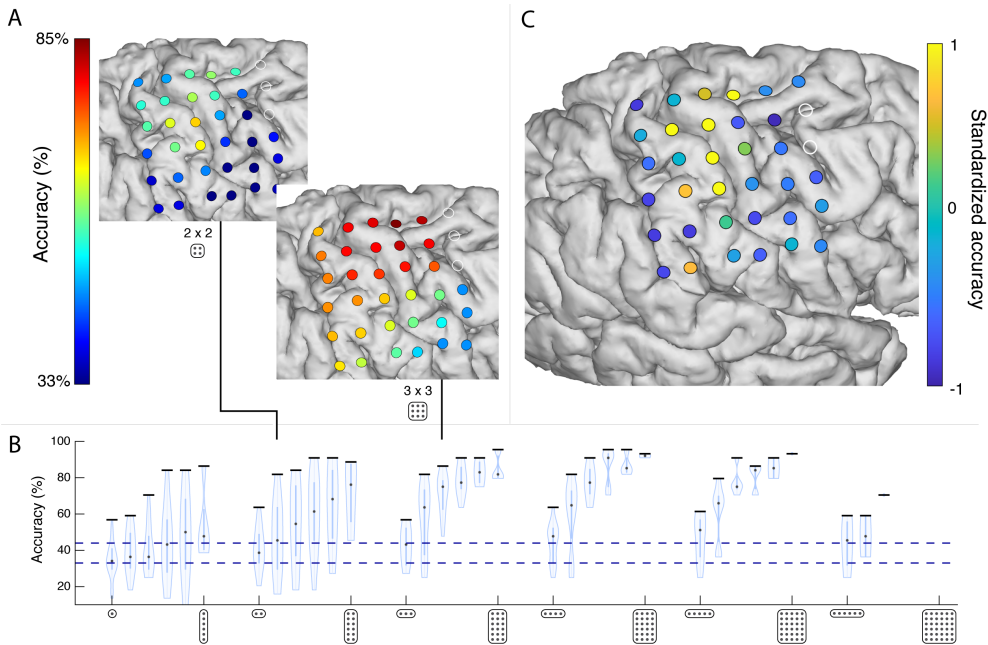
Figure 5. The spatial distribution of information. (A) Searchlight classification maps of searchlight with 2 × 2 (top) and 3 × 3 electrodes (bottom). (B) The classification results of the different searchlights, ranging from 1 × 6 to 6 × 6 grids in two directions (superior-inferior, anterior-posterior). Each violin plot represents the searchlight results with a specific grid configuration. The violin represents the distribution of the classification accuracies at the different searchlight positions within the grid, with a black horizontal bar to indicate the searchlight position that classified the highest. The lower dotted blue line shows the chance level at 33%, while the upper blue line indicates the threshold of 45% above which the decoding accuracy was significant. Note that, for the larger searchlight grids, virtual placements were limited or not possible due to overlap with the bad electrodes. (C) Most informative electrodes, identified by a random search classification on 10.000 subsets of electrodes.

Ipsilateral finger representations

In addition to attempted movement, the patient also performed runs of executed hand movements with the healthy, ipsilateral, hand. Frame perfect video annotations were used to quantify the movement of the healthy hand. An average delay of 0.44 s (std: 0.09) occurred between the cue onset and actual start of the movement. The patient moved his hand for about 3.69 s (std: 0.53) on average over all trials, with about 3–5 flexions of the finger per trial.

Only a few channels on the hand-area showed a strong ipsilateral increase in HFB power during executed movement, whereas some other channels showed a smaller, yet significant, ipsilateral decrease in HFB power (figure 6). An ipsilateral distributed decrease in LFB was found, but was less spread out over the cortex compared to attempted movement. The HFB power for executed movement showed a transient response with a temporal peak

between 0.5 s and 1 s, in line with the behavioral start of the hand movement and slightly earlier than the HFB peak in attempted movement at 1 s.
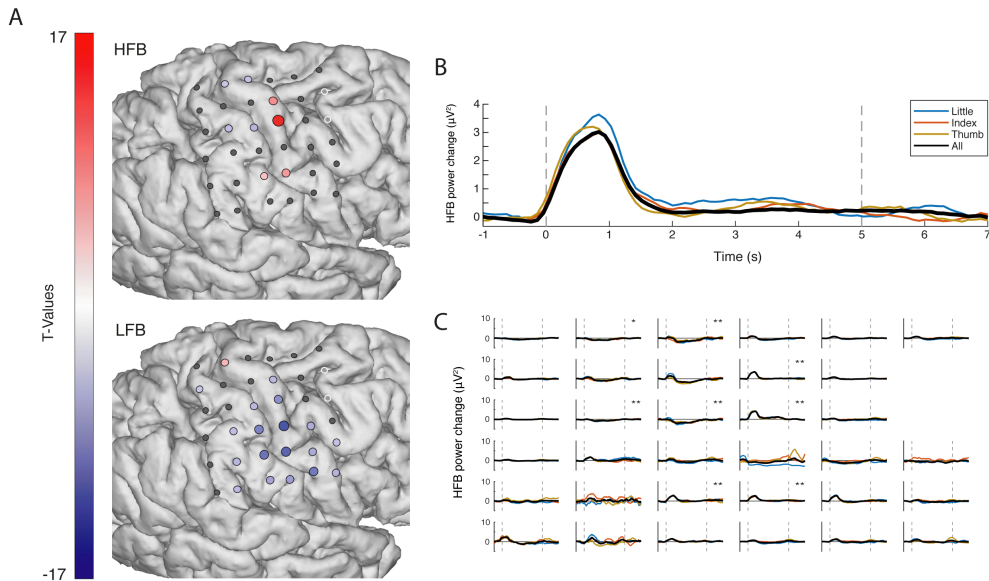
Figure 6. The, ipsilateral, electrophysiological response of executed movement versus rest. (A) The changes in HFB (top, 65–175 Hz) and LFB power (bottom, 15–28 Hz) for each grid electrode. Electrodes with a red or blue color showed a significant change in band-power, whereas electrodes with an insignificant change in band-power are shown in grey; the two excluded electrodes are shown in white. (B) HFB power changes over time averaged across those electrodes that showed a significant positive increase. The black line represents all fingers, whereas the colored lines represent individual fingers. The two vertical dotted lines indicated the cue on- and offset. (C) The HFB power changes over time, each graph represents one electrode.

Classification was performed on the ipsilateral response to the movement of the healthy hand. Based on the HFB power of all electrodes, finger movements could be classified with an accuracy of 56%.

2.4 Discussion

In order to understand whether somatomotor physiology is preserved after deafferentation, we investigated the contralateral electrophysiological responses of attempted finger movements in a single patient with an upper-arm amputation. With attempted movement, a spatially-focal increase was found in broadband high-frequency ranges (65–175 Hz) over the hand-area of the primary sensorimotor cortex. A spatially distributed decrease was found in the lower frequency bands (15–28 Hz).

The electrophysiological response in our patient with an amputated arm is similar to what is seen in many previous studies that have investigated ECoG spectral power changes

during finger movements. These studies show typical physiological responses, with a localized high frequency increase and a distributed low frequency decrease [3–5]. Finger somatotopy is represented in both the M1 and S1 and can be decoded from high frequency activity [9,10,13,14]. The similarity between our results and those in healthy people suggests that the motor physiology of the hand is retained. Still, it is important to understand whether this typical physiology is retained in different patient populations.

Studies that investigated the motor electrophysiology in patients with locked-in-syndrome (i.e. ALS, PLS or brainstem-stroke) using EEG, MEG or permanent ECoG implants found similar results. In these patients, a robust HFB response was retained [136]. Whether and/or how the LFB response was affected varied between studies. Some studies observed robust low frequency power decreases in patients with ALS and/or PLS [137–139]. Other studies reported reduced power decreases in ALS [140], or more variability between patients with ALS, tetraplegia and brainstem stroke, with only some patients showing robust low frequency power decreases [136,141]. These studies suggest that whether low frequency power decreases are retained depends on the disease (progression) and the influence of closed-loop feedback training. Here we have observed that there are strong and significant low frequency power decreases during attempted movement in a patient with an amputated arm.

The HFB response of attempted movement was both transient and sustained, similar to what was found in research on continuous/repeated executed finger movements [25,142]. For attempted movement, the HFB power peaked at ~1 s after cue onset and returned gradually back to baseline during the remainder of the trial. Part of the latency between the cue onset and the peak of the cortical response can be explained by the lag between the interpretation of the cue and movement initiation, which in the executed movements of the patient already accounted for ~0.5 s. Another factor that could have contributed to this ~1 s latency may be related to the fact that motor imagery can be demanding in terms of mental fatigue and effort [143,144]. In terms of decoding, both the transient and the sustained responses contained information about finger movements. The classifications of attempted finger movement over time confirmed that most information (i.e. the highest classification accuracies) was found around the peak of the response at 1 s after cue presentation. The classification accuracies were more variable when including only the sustained response. However, larger time-windows (>2500 ms) that included both the transient and sustained responses yielded higher classification accuracies than smaller windows (<2500 ms), implying that the inclusion of (part of) the sustained response can contribute to the decodability.

Each individual finger resulted in a strong HFB response in the hand-region of the sensorimotor cortex. Although each of the fingers elicited a different HFB response pattern, no clear topographical representation of the fingers was found. Regardless, using support vector machine learning, we were able to decode the attempted movement of three individual fingers significantly at a classification accuracy of 93% (well above the 33% chance level). Which is similar to the decoding accuracies of executed movement of the fingers [10,11]. Attempted movements of the thumb could be decoded at 100% accuracy, however the index

and little finger were less discriminable with sensitivity values of respectively 93% and 87%. Such decoding accuracies confirm that individual finger representations in the cortex are retained and can be distinguished in a patient with an amputated arm. These results align with earlier fMRI research on patients with long term upper arm amputations [112,113,145], while other fMRI studies have shown displacement of the cortical activation into the deafferented motor and somatosensory areas during lip [106], chin [104] and face/shoulder movement [105]. It is possible that the cortical representations of other body parts invade the cortical regions of an amputated limb, which would warrant further investigation. However, studies in the visual cortex have shown only a limited ability for the primary cortex to reorganize [146]. Our research similarly demonstrates that, while it is possible that representations co-exist, the electrophysiological signals related to finger representation of the missing hand are at least largely retained and not replaced by other functions.

        In contrast to tetraplegic or locked-in-patients, there are several important aspects to consider in patients with an amputated limb. For one, attempted movements by patients with an amputated arm could be considered as phantom movements, where potential residual output to muscles and input from nerve endings in the stump may play a role. In addition, this patient experienced phantom pain, and there may be a link between this pain and the neurophysiological responses we observed. Phantom pains are believed to arise from maladaptive cortical reorganization invading the cortical region of the missing limb [147,148], which is supported by several studies that show a (positive) relation between the displacement of cortical activity and phantom pains [105,106,149–152]. As such, various mirror or hand imagery therapies aimed towards the reengagement of the invaded cortical areas have been developed and shown to reduce phantom pains [153–157]. However, recent studies have shown that people with chronic pain can also exhibit greater activity during phantom movement [158,159]. Also, a study with a large sample of phantom limb patients did not report a relationship between phantom pain and cortical reorganization [160]. It appears that the relation between the chronic phantom pain and retained physiology is more complex and the exact workings are still debated [161,162]. Based on our experiment, it is not possible to draw conclusions on the effect of phantom pains on the representations of the missing hand. However, taking into account that, first, there are a number of fMRI studies that include patients with upper arm amputations that still have representations of their missing hand upon attempted/phantom movement while having no phantom limb pains [152] or low to medium phantom limb pains [145,159]. Second, studies into tetraplegia and stroke patients have shown that even without these "phantom" factors and without any peripheral information, finger and hand representations are preserved in primary sensory and motor areas [82,114,115]. Therefore, it seems likely that the increased high frequency activity, decreased low frequency activity and decodable finger movements are not merely driven by the stump or phantom limb pains. In addition, previous MEG research that uses a (virtual) prosthesis [117,163], suggests that the intact hand representations in the phantom cortex may be actively used in a BCI and could potentially reduce phantom limb pain.

In BCI applications, devices are often controlled with signals from the sensorimotor cortex using attempted movements [1,29–31]. Our data showed that we could decode finger movements after deafferentation, suggesting that these motor programs are retained by some degree and these signals can also be used to control a BCI. Understanding which signal properties allow for reliable decoding and BCI control is essential for these applications. Temporally, different parts of the electrophysiological signals can be included, but a tradeoff can occur between the speed of decoding and classification accuracy. A smaller window could allow for faster and more subsequent classifications, but could go at the expense of classification accuracy. Our data suggest that shorter (e.g. 1000 ms) time windows may already provide a good accuracy (~80%) for decoding 3 fingers, while larger windows (e.g. 3000 ms) will further improve accuracy (>90%). Patients may be able to use such short time windows, as one study in a patient with ALS already showed that movement versus rest can be decoded using a 1 sec window [1]. Understanding how well movement activity is retained after deafferentation may have implications for BCIs in patients with paralysis, as well as an amputated limb, as BCIs may reduce phantom limb pain [117].

Attempted movement after loss of function is different from imagined movements in healthy people, a distinction that is of particular importance for implanted BCIs. It has been debated whether motor imagery representation overlaps with overt movement in brain surface recordings [164,165], and whether motor imagery is a good approximation of attempted movement after limb loss or paralysis. One would intuitively expect that, in the case of a lost limb, the native map of representation would either be retained, or generally degrade. This patient's map shows that somatotopic distinction is retained several years after limb loss. Some types of motor imagery in healthy individuals may thus not be a good general approximation or motor representations after limb loss or paralysis for implanted BCIs.

An additional point of importance for BCIs is the electrode grid design and extent of cortical coverage, which can have a strong influence on BCI performance [1,94]. Our results show that most information about attempted movement is located on the hand-region of the primary motor and sensory cortex. In terms of cortical coverage, considering an inter-electrode distance of 10 mm, a good (>80%) classification accuracy can already be achieved with as little as 2x2 electrodes (13 mm × 13 mm) placed over the primary sensorimotor cortex. More electrodes could provide up to ~90% classification accuracy.

Finger movement activity on the ipsilateral cortex of the intact hand could be decoded, but less accurately compared to decoding the contralateral attempted finger movements, suggesting that the contralateral, phantom limb, still has a stronger representation compared to the ipsilateral hand. Only a few channels showed power increases during ipsilateral movements, while some electrodes also showed significant high frequency power decreases. Whether previous ECoG studies show similar ipsilateral high frequency power decreases during executed hand movements is less clear [166]. However, ipsilateral decreases in sensorimotor activity during hand movement in healthy subjects have been observed in the fMRI BOLD signal [121,123]. TMS studies similarly show evidence for contralateral inhibition [167,168]. The ipsilateral decreases in high frequency power we observed with ECoG may thus

potentially be related to inhibition resulting from activity of the contralateral hemisphere, or to some reorganization of function after the injury (as has been seen with patients after perinatal hemispheric stroke [164]).

2.5 Conclusion

This case study shows that the electrophysiology of attempted hand movement is preserved in the sensorimotor cortex after deafferentation of an amputated hand, with a typical focal increase of HFB power over the hand region and a more distributed decrease in LFB. Attempted finger movements provided a transient HFB peak around 1 s after cue onset, followed by a sustained HFB response. Classification analyses confirm that most decodable information on the finger movement can be found around this peak. Furthermore, HFB power can be used to decode finger movements with high (>90%) accuracy. Optimal decoding could be achieved based on the first 1–3 s of the signal and would only require 13–13 mm of cortical coverage. Our results demonstrate that the sensorimotor electrophysiology remains largely intact after long term (3 years and 11 months) amputation and therefore remains a viable region for BCIs that use the decoding of hand-gestures for control.

2.6 Acknowledgements

2.7 Supplementary material

Supplementary Figure 1. The electrophysiological responses in the spatial and time domain for both the 15-28Hz and 8-13Hz low-frequency bands during attempted movement (contralateral) and executed movement (ipsilateral). Electrodes with a red or blue color showed a significant change in band-power power, whereas electrodes with an insignificant change are shown in grey; the two excluded electrodes are shown in white. The time traces show the LFB power changes averaged across those electrodes that showed a significant decrease. The black line represents all fingers, whereas the colored lines represent individual fingers. The two vertical dotted lines indicated the cue on- and offset.

Chapter 3

Chapter 3 - Functional MRI based simulations of ECoG grid configurations for optimal measurement of spatially distributed hand-gesture information

Abstract

In electrocorticography (ECoG), the physical characteristics of the electrode grid determine which aspect of the neurophysiology is measured. For particular cases, the ECoG grid may be tailored to capture specific features, such as in the development and use of brain–computer interfaces (BCI). Neural representations of hand movement are increasingly used to control ECoG based BCIs. However, it remains unclear which grid configurations are the most optimal to capture the dynamics of hand gesture information. Here, we investigate how the design and surgical placement of grids would affect the usability of ECoG measurements.

High resolution 7T functional MRI was used as a proxy for neural activity in ten healthy participants to simulate various grid configurations, and evaluated the performance of each configuration for decoding hand gestures. The grid configurations varied in number of electrodes, electrode distance and electrode size.

Optimal decoding of hand gestures occurred in grid configurations with a higher number of densely-packed, large-size, electrodes up to a grid of ˜5 × 5 electrodes. When restricting the grid placement to a highly informative region of primary sensorimotor cortex, optimal parameters converged to about 3 × 3 electrodes, an inter-electrode distance of 8 mm, and an electrode size of 3 mm radius (performing at ˜70% three-class classification accuracy).

Our approach might be used to identify the most informative region, find the optimal grid configuration and assist in positioning of the grid to achieve high BCI performance for the decoding of hand-gestures prior to surgical implantation.

3.1 Introduction

The human brain can be explored at many different spatial scales, from (sub)millimeter to centimeter resolution. Each scale of measurement provides a unique window into the underlying neuronal activity [169]. As a result, research is often bound by the resolution at which information is captured. An empirical understanding of which resolution provides the most information for the interpretation of a particular brain function is essential for the development of brain–computer interfaces (BCI). Electrocorticography (ECoG)-based BCIs utilize properties of intracranial electrode grids to record the electrical field potential from neuronal populations [1,4,6,31,66,82,170]. The ECoG signals are translated or interpreted to understand brain activity or to control external devices. ECoG grids can be configured in a number of ways: spanning small or large areas of cortex with different electrode sizes and densities. Currently, several different grid configurations are used in research, varying from traditional clinical electrode grids and strips with 1 cm inter-electrode distance to high-density research grids [171]. The configuration of an ECoG electrode grid determines the resolution and scale with which the underlying neuronal activity is measured, and therefore which information is conveyed to a BCI. Therefore, it is essential to know which configuration provides the most useful information for control. In practice, comparing different electrode configurations on the same brain region in human subjects is not possible given the invasive nature of ECoG recordings and the fact that this is done in a clinical setting. Given the limitations in experimental testing and the need for regulatory approval of implanted BCI systems in humans [1,31,172], it is essential to understand which scale provides most information about brain functions used in BCIs.

Hand-representations are a promising target for use in BCIs [50,92]. During hand movement, a robust neurophysiological response occurs in the contralateral sensorimotor cortex [4,5] with a focal increase of high-frequency band (HFB) power and a more distributed decrease in low-frequency band/ power [22]. Subsequent ECoG research showed that the representations of different fingers can be distinguished in the primary sensorimotor cortex using a HFB component [9]. Given the increased interest in the use of hand-representations in BCI solutions [1,11,29,50,93,173] it is essential to understand which grid configuration would optimally capture hand movement information. Recent research has shown that the ECoG HFB signal correlates well with the BOLD response at the standard clinical scale [22], that the millimeter scale finger representations found in ECoG HFB activity are well matched with 7T fMRI [13] and that even non-linearities in 7T fMRI match the ECoG HFB responses [25]. Therefore, even though fMRI is a less direct measure of neuronal activity than electrode recordings, the two modalities do correlate well across multiple spatial scales, suggesting that we can leverage 7T fMRI to simulate different grid configurations and estimate the electrode scale and density that would provide the most information to decode hand movement.

In this study, we specifically investigate which ECoG scale captures the most information about hand-gestures. Using 7T fMRI measurements, we simulated the placement of different grid configurations on the exposed brain surface, varying the number of

electrodes, inter-electrode (center-to-center) distance and size in a similar manner to variations found in commercially-available ECoG implants.

3.2 Methods

Participants

Ten healthy subjects (age 23.9 ± 5.1 years, six female) participated in the experiment. All participants had normal or corrected-to-normal vision. The study was approved by the ethics committee of the University Medical Center Utrecht (ref 13-585) and participants gave written informed consent to participate, in accordance with the Declaration of Helsinki (2013). According to the Edinburgh Inventory [174], all were right-handed.

Task

Participants were asked to execute three hand gestures taken from the American Sign Language alphabet (the letters S, F, and L), shown in figure 1. The gestures were chosen to maximize the difference between flexion and extension of the finger combinations. All participants were naïve to sign language and were trained prior to the experiment on the three letter-gesture combinations. While in the scanner, one of the three letters was presented each trial. Each letter was shown for either 3, 5 or 7 s, followed by a fixation cross shown for 12 s. Participants were instructed to perform the corresponding gesture upon appearance of the letter and hold the gesture until the letter disappeared. A total of 45 letters were presented at random, ensuring 15 trials per letter. The different durations were equally balanced over the letter conditions.
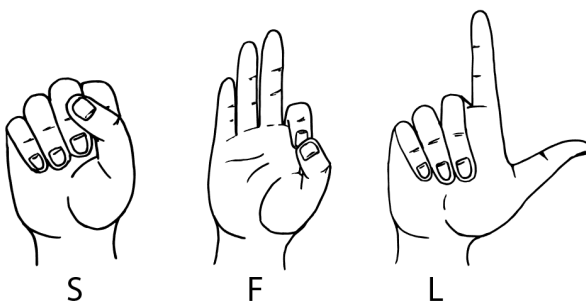
Figure 1. Hand gestures used in this study. The three hand gestures were taken from the American Sign Language alphabet and involved the S, F and L. Note that during the task only a letter was presented, while the participant performed the corresponding gesture.

MRI data acquisition

MRI data were acquired using a 7T Philips Achieva MRI system with a 32-channel head coil. Functional MRI data were recorded using an EPI sequence (TR/TE = 1600/27 ms, FA = 70∘, 26 slices centered around the motor cortex, acquisition matrix 144 × 144, slice thickness 1.60 mm with no gap, 1.47 mm in plane resolution); shared datasets can be found on OSF: https://osf.io/z6j3x/. A T1- weighted image (TR/TE: 7/3.05 ms; FA: 8; resolution 0.78 × 0.78 mm in-plane, slice thickness 0.8 mm, no gap) was acquired for anatomical reference. The cues were visually projected onto a mirror attached to the head coil. Each participant performed a single functional run of the task with 481 volumes (five dummy volumes) which took about 13 min.

Preprocessing

Preprocessing of the imaging data was performed with the use of SPM12, FSL and custom MATLAB (Mathworks Inc.) scripts. The anatomical image was skull-stripped using the white and grey matter segmentation output and converted to a 3D brain surface [175] using Freesurfer (http://surfer.nmr.mgh.harvard.edu/). Functional images were slice-time corrected, realigned to correct for motion and corrected for geometric distortions [176]. The corrected functional images were aligned to the anatomical scan by transformation of their affine matrices. No reslicing/resampling was done at this stage to prevent a potential loss of decodable information.

Grid simulation

In order to investigate which different ECoG grid configurations would capture hand-gesture information best, we simulated different grid configurations on the exposed (unwarped) brain surface convexity to assess how different grid configuration parameters influence decoding performance of the three gestures from fMRI data. To achieve the most realistic simulations, all analyses were done in the subject's native space. The process of simulation involved three steps: positioning the centers of the virtual grids (figure 2A), placement of different grid configurations around this center (figure 2B) and the decoding of gestures based on the underlying voxels from the functional volumes to evaluate the information that is captured by each grid (figure 2C).
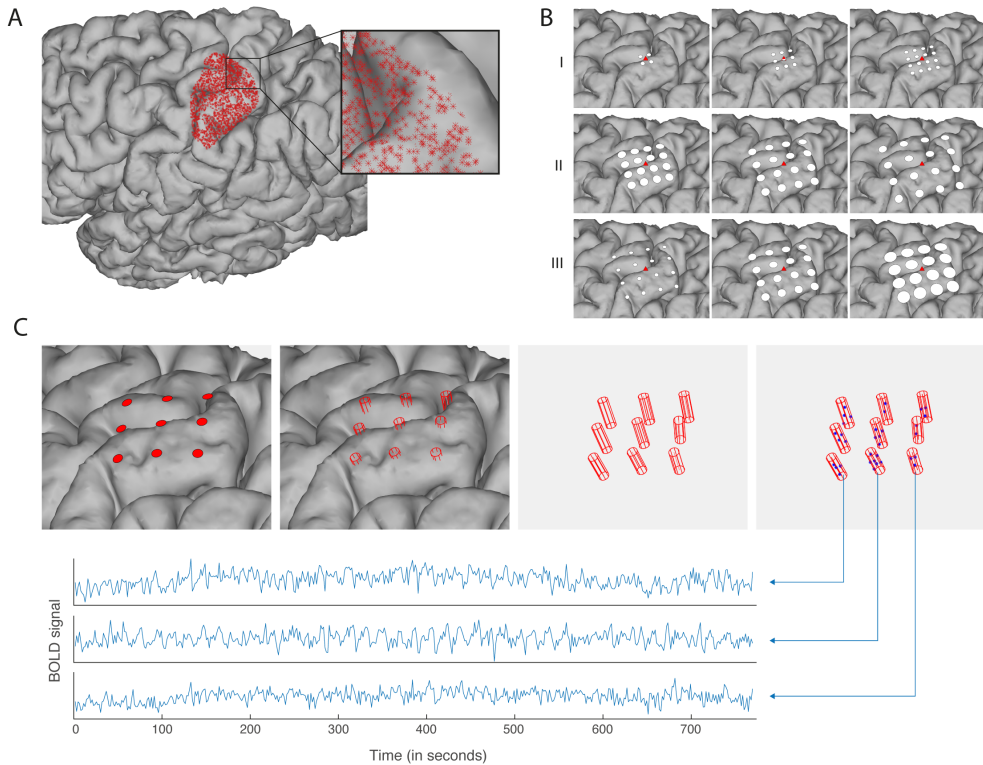
Figure 2. The grid simulation procedure (subject 7). (A) The centers of the virtual grids were positioned over an empirically-identified cortical hand-gesture area. A searchlight classification evaluated 200 000 potential center positions for underlying hand-gesture information. Positions that yielded classification above the 95% percentile were kept (~17 000 positions). A subset of 2000 positions were selected at random and served as the centers for the simulation of different grid configurations. (B) Different grid configurations were simulated at each of the 2000 positions. The center of each simulated grid is shown as a red triangle, the white discs indicate the placement of virtual electrodes given different grid configurations. Grid configurations varied in number of electrodes (2 × 2 ... 8 × 8), inter-electrode distance (4 mm, 6 mm, 8 mm, 10 mm center-to-center) and electrode size (radius of 1 mm, 2 mm, 3 mm). A total of 84 grid configurations were simulated per position. (C) All of the 2000 center positions, with each 84 grid placements, were evaluated by the classification of the hand-gestures. Classification was performed using a support vector machine (SVM), where each electrode represents one input feature. The signal for each electrode was the average BOLD amplitude of the gray matter voxels in the functional volumes that fell inside of the electrode cylinder.

The centers of the grids were positioned over an area in the brain that has meaningful information related to the hand motor task. In order to find that meaningful area, a convex brain surface hull was produced for each participant, covering the dorsal and lateral side of the frontal- and parietal lobe. Next, 200 000 potential grid positions were generated on the hull at random. Decoding performance for each position was evaluated by performing multivariate searchlight classification [177] using the voxels in the functional volumes within a 7 mm radius as features to classify on. A searchlight approach was preferred over the use of

activity amplitude as it provides a more qualitative estimation of the local information [177]. After the classification of all potential positions, only the positions with a classification accuracy score above the 95th percentile were kept and used as centers for the simulated grids. For every participant, this procedure resulted in a cluster of positions over the sensorimotor cortex roughly overlapping the hand-knob area, shown in supplement figure 1. For five participants, several smaller clusters of positions were identified in addition to the large cluster around primary sensorimotor areas. In such cases, only the largest sensorimotor cluster was kept. On average, a sensorimotor cluster contained ~17 000 positions. To limit the number of calculations, 2000 positions were picked at random for grid simulation (figure 2A).

During grid placement, each of the 2000 positions received a random rotation and served as the center for multiple grid projections, as demonstrated for a single position in figure 2B. Grid configurations varied in number of electrodes (2 × 2, 3 × 3, 4 × 4, 5 × 5, 6 × 6, 7 × 7, 8 × 8), inter-electrode distance (4 mm, 6 mm, 8 mm and 10 mm center-to-center) and electrode size (radius 1 mm, 2 mm, 3 mm). As a result, a total of 84 (7 × 4 × 3) virtual grids were 'placed' per position.

After placement, each grid was used to classify the three executed hand gestures by taking the signal from the grey matter fMRI voxels underneath each virtual grid electrode, shown in figure 2C. For each electrode, a cylinder with the radius of the electrode was projected perpendicular to the convex hull of the cortical surface reaching 5 mm downward and 5 mm upward. Only the gray matter voxels (according to the Freesurfer segmentation) from the functional volumes within each electrode cylinder were used for classification. Because the virtual electrodes were positioned onto a hull of the brain, it is possible that they fell slightly inside of the gyri; The inclusion of voxels upward from the electrode made certain that no gray matter voxels were excluded, which in reality would be underneath the electrodes. We required a minimum of two features (i.e. electrodes) in each grid configuration. In addition, to prevent grids with a large surface (i.e. high number of electrodes and/or inter-electrode distance) from covering and classifying from regions far outside of the primary sensorimotor, only voxels within 15 mm of the sensorimotor cortex (as defined by the Desikan-Killiany atlas [178]) were used during classification. The MATLAB scripts that were used to implement the grid simulations are publicly available through the open science framework (OSF: https://osf.io/z6j3x/).

Classification procedure

The classification procedure was implemented using custom MATLAB (Mathworks Inc.) code provided alongside this article (OSF: https://osf.io/z6j3x/). Before classification, the raw BOLD signal of each voxel was normalized (division by its mean and multiplication by 100) to reflect the percentage signal change, and detrended (linear, quadratic and cubic). Classification was performed using a SVM and a linear kernel [130].

The voxels or combination of voxels that were used as features in the SVM differed per step of the simulation procedure. During the step of grid positioning, a searchlight was

used, where each grey matter voxel within the searchlight served as a feature in the SVM. During the step of decoding grids, the gray matter voxels within each virtual electrode (i.e. cylinder) were averaged and each electrode average served as a feature in the SVM.

The BOLD response that we used in the SVM was determined as follows. For each trial, we took the time-period around the expected peak of the hemodynamic response ($t_{startHRF}$ - t_{endHRF}) based on the trial's duration (3, 5, or 7 s). Within that time-period, we calculated the average over all features $\underline{X}(t)$ and determined the time t_{max} that yielded the highest BOLD peak (where $\underline{X}(t)$ was maximum). The BOLD signal of each virtual electrode at that scan time X (t_{max}) served as a feature in the classification. Multiclass classification (three gestures) was achieved by applying a one-versus-all classification scheme, where every class is classified against the data of all other classes together, and the winner (furthest from the hyperplane) takes all. The decodability of the three gestures was determined using a leave-one out cross validation and is expressed as a classification accuracy score, which is the percentage of trials that were predicted correctly.

Two ways to position grids

In the first analyses, we placed the center of the simulated grid in the area with meaningful information about the gestures (figure 2A). However, as the number of simulated electrodes increases, grids become larger than the informative region and extend beyond it. To investigate whether classification could be optimized by restricting all electrodes in the stimulated grids to the informative region, we also ran the simulations while limiting the grids to entirely fall within the region of interest indicated by the searchlight.

Statistics

To determine whether a classification score was significantly above chance, we used the cumulative binomial distribution. Given 45 trials, a chance level of 33% and a cumulative probability of 95% (one-sided, α = .05), classification scores above 44% were considered significant.

The effects of the variations in grid configuration were evaluated by a full factorial analysis of variance (ANOVA). For each of the ten participants and each grid configuration (7 × 4 × 3 = 84), the average over the 2000 classification accuracy scores was used as the dependent variable. The ANOVA evaluated the effects of three properties (as independent variables): the number of electrodes (seven categories), the interelectrode distance (four categories) and electrode size (three categories).

3.3 Results

The effect of grid configuration on hand gesture classification accuracy

A total of 84 grid configurations were simulated with variations in the number of electrodes (seven variations: 2 × 2, 3 × 3, 4 × 4, 5 × 5, 6 × 6, 7 × 7, 8 × 8), distance between electrodes (four variations: 4 mm, 6 mm, 8 mm, 10 mm) and electrode size (three variations in radius: 1 mm, 2 mm, 3 mm). Different configurations produced different classification accuracies, shown for a typical subject (subject 7) in figure 3 and for all subjects in supplementary figure 2.

In each individual subject, the changes in number of electrodes, distance and size showed several effects: first, more electrodes resulted in a better classification accuracy. The largest increase in classification accuracy was observed when the number of electrodes increased from smaller (e.g. 2 × 2) to medium sized grids (e.g. 5×5), beyond which accuracy barely improved. Second, an increase of distance between the electrodes resulted in a decrease in classification accuracy in grids with a larger number of electrodes (more than ~5 × 5). Third, increasing the electrode size resulted in a better classification accuracy in all situations. These effects were highly robust across individual subjects (supplementary figure 2).
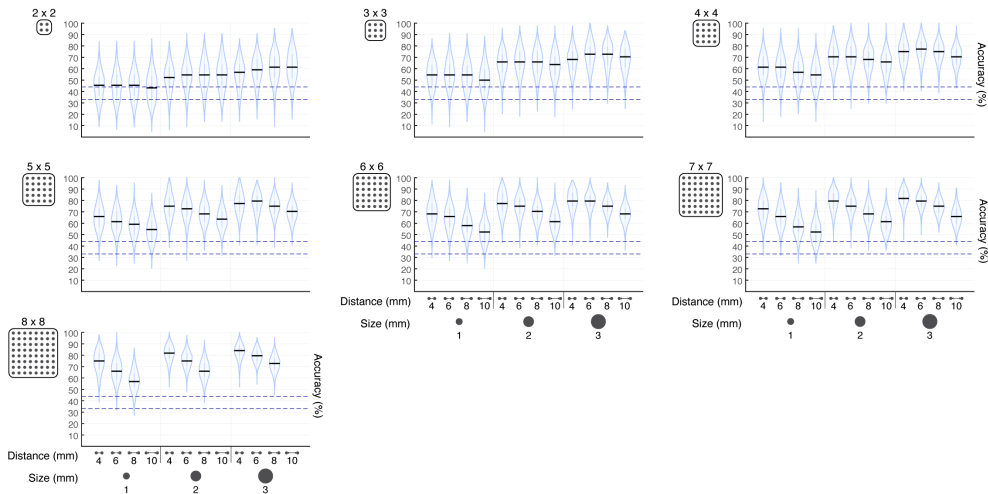
Figure 3. Classification accuracy as a function of grid configuration in a typical subject (subject 7). Each graph represents one variation in the number of electrodes. Each column in each graph represents a different inter-electrode distance (center-to-center) and electrode-size (radius) combination. Every violin reflects the distribution across the 2000 scores, with a horizontal black line in every column to indicate the median. The lower blue dotted line indicates the chance level at 33%, while the upper blue line indicates the threshold (at 44%) above which the accuracy was significantly above chance.

The effects seen in the individual subject can also be observed in the average group classification accuracies for each of the 84 simulations (figure 4) and the averages of the classification accuracies per significant factor (number, space, size; figure 5). Firstly, more electrodes result in a significantly higher classification accuracy (figure 5A, three-way ANOVA across all ten participants: $F(6, 711) = 47.42$, $p < .01$). Secondly, an increase in distance between the electrodes significantly lowers the classification accuracy (figure 5B, $F(3, 711) = 23.81$, $p < .01$). Thirdly, a larger electrode radius causes a significant increase in classification accuracy (figure 5C, $F(2, 711) = 162.02$, $p < .01$). The second effect, where an increase in inter-electrode distance caused a decrease in classification accuracy, was stronger for larger numbers of electrodes, shown in a significant interaction between the number of electrodes and electrode distance (figure 5D, $F(17, 711) = 2.52$, $p < .01$). The model accounted for a total of 47% of the variance in classification accuracy.
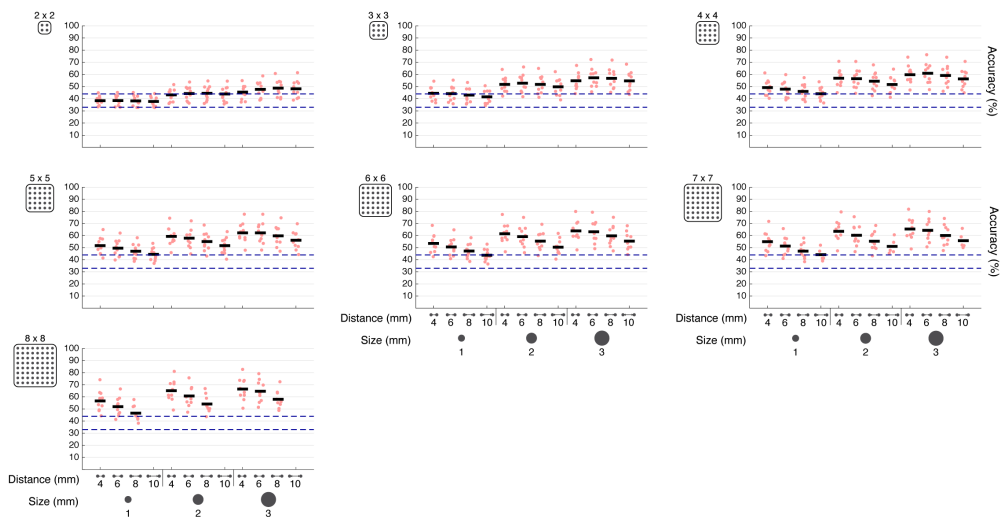
Figure 4. Classification accuracies for each grid configuration across the group. Each graph represents one variation in the number of electrodes. Each column in each graph represents a different inter-electrode distance (center-to-center) and electrode-size (radius) combination. The red dots indicate the average classification accuracy for every participant, with a horizontal black line in every column to indicate the average over all participants. The lower blue dotted line indicates the chance level at 33%, while the upper blue line indicates the threshold (at 44%) above which the accuracy was significantly above chance.
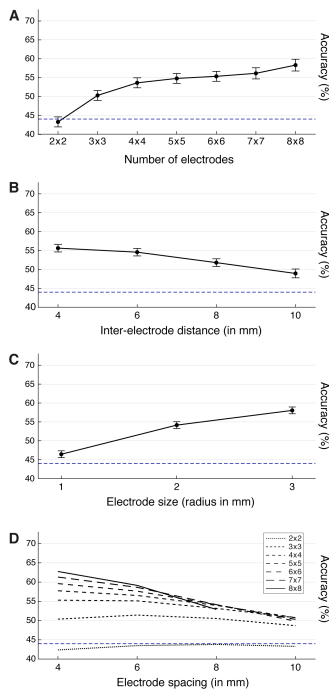
Figure 5. The average classification accuracy per grid configuration factor across the group. Group results showing the means for the three grid configuration parameters and the significant interaction effect. The error bars in the top three plots represent a 95% confidence interval. The blue dotted line at 44% indicates the threshold above which the accuracy was significantly above 33% chance level.

The effect of grid configuration on hand gesture classification accuracy with placement of the entire grid within the most informative area

To investigate whether classification could be optimized by restricting all electrodes in the stimulated grids to the informative region, we ran the simulations while limiting the grids to fall only within the region of interest indicated by the searchlight (figure 6). Some of the larger grids, with more electrodes and/or increased distances between electrodes, could not be simulated as they exceeded the region's boundaries (supplement figure 1). Increasing the number of electrodes up to 5 × 5 electrodes on the informative region significantly increased the classification accuracy (figure 6B, $F(3, 222) = 67.43$, $p < .01$). The effect of inter-electrode distance no longer reached significance, but became a trend (figure 6C, $F(3, 222) = 2.50$, $p = .06$) where more distance increased the classification accuracy (figure 6). Interestingly, within this area, a larger electrode radius still significantly increased the classification accuracy (figure 6D, $F(2, 222)=39.39$, $p < .01$).

 Note that while the number of electrodes improved classification accuracy (figure 6B), grids with less electrodes could also reach classification performance within the same range. Electrode grids of 5 × 5 electrodes, 4 mm inter-distance and 3 mm radius provided a classification accuracy of 73% (range 59–88) (figure 6A, bottom right); grids of 3 × 3 electrodes, 8 mm inter-distance, 3 mm radius provided a classification accuracy of 68%

(range 58– 80) (figure 6A, top right). Much smaller grids of 2 × 2 electrodes, however, showed a much lower range of classification accuracies and reached a mean accuracy of 52% (range 40–68) at 10 mm inter-distance, 3 mm radius.
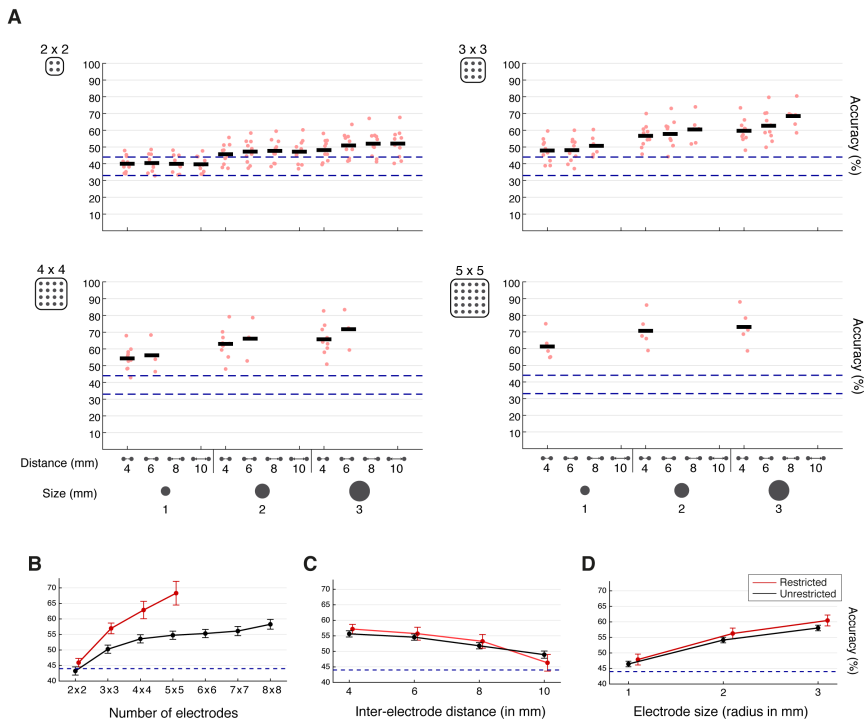
Figure 6. Classification accuracy as a function of grid configuration when limiting the grids to an informative region. (A) The classification accuracies on all grid configuration parameters. Each graph represents one variation in the number of electrodes, the columns represent variations in inter-electrode distance and electrode-size. Each red dot indicates a single participant, the horizontal black line indicates the average over participants. The two dotted lines indicate 33% chance level and the threshold above which the accuracy was significantly above chance at 44%. (B)–(D) The group means for the variation in number of electrodes (B), inter-electrode distance (C) and electrode size (D) are shown when the grid is placed in the informative area (red lines). For comparison, the data from figure 5 are also displayed in black. Note that the direction of the trend in electrode space (C) might be misleading, the higher inter-electrode distances are biased to grids with a low number of electrodes, because only these grids would fit in the informative region, and therefore might result in a lower average score. The error bars represent a 95% confidence interval. The blue dotted line indicates the threshold (at 44%) above which the accuracy was significantly above 33% chance level.

*Optimal grid placements can be identified to improve hand gesture classification
performance*

The simulation results may be used to predict grid configurations with high classification
accuracy in individual subjects for BCI purposes. In addition, some grids can exceed the
average classification accuracy of that configuration when positioned in the correct way. As
a proof of concept, we performed an agglomerative cluster analysis on the 2000 grid
placements within three specific grid configurations (3 × 3, 8 mm inter-distance, 3 mm radius;
4 × 4, 8 mm inter-distance, 2 mm radius; 5×5, 4 mm inter-distance, 1 mm radius). Within each
configuration, the 2000 grids were spatially clustered based on the 3D positions of two corner
electrodes, while limiting the Euclidean clustering distance to 2 mm. This results in clusters
of grids that have similar position and angle. Figure 7 shows, for three of the grid
configurations, the cluster that provided the highest average classification accuracy (over the
grids in that cluster) for a single subject (subject 7). Grid placement suggestions for all
participants are shown in supplementary figure 3. We required clusters to have at least three
grids. As demonstrated in supplementary figure 4, different Euclidean clustering distances
will provide different clusters, which consist of different numbers of grids. The clustering
method and parameters we have used here for this proof of concept is just one of the ways
to find the optimal position based on the simulated data. In terms of grid placement, the
simulated grids and clustering can be used to find a balance between the spatial margin of
error in placement (i.e. the number of grids in the simulation and their clustering distance)
and the expected classification performance.
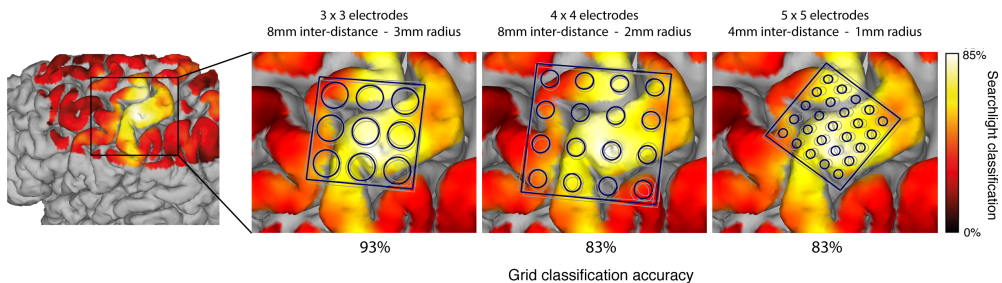
*Figure 7. Proof of concept for the optimal placement of three different grid configurations in subject 7. The
leftmost image shows a heat-map of the brain that indicates the presence of hand-gesture information based
on searchlight classification. The three images on the right show an optimal placement within three different
grid configurations. Each of the suggestions is based on an agglomerative cluster analysis on the 3D positions
of two corner electrodes of the 2000 grid placements within that grid configuration. Grids, limited to a
Euclidean distance of 2 mm, were clustered together. The grid-cluster with the highest average classification
accuracy (over all grids) is shown for each of the three grid configurations, the individual grids in that cluster
are shown in grey and their average position in blue. The average classification accuracies over the grids in
the cluster is shown underneath the image.*

3.4 Discussion

This study investigated how different simulated ECoG grid configurations capture information on executed hand-gestures from the brain surface. To this end, 7T fMRI data were used as a proxy for neural activity, allowing for virtual placement of a range of grid configurations and parameterized assessment of electrode number, size and distance. Our simulations show that increasing the number of electrodes improves hand-gesture decoding accuracy, with the largest improvement seen up to 5 × 5 electrodes. Reducing inter-electrode distance and increasing electrode size (to 3 mm in radius) improved hand gesture decoding accuracy.

Decoding accuracy was further optimized when grids were restricted to an informative region for hand-gestures as identified in individual subjects by searchlight classification. We found good classification scores (68%, with chance at 33%) for grids with 3 × 3 electrodes, 8 mm inter-electrode distance and a 3 mm electrode radius. Adding electrodes up to 5 × 5 at 4 mm inter-distance and 3 mm size provided small increases in classification accuracy (73%). These grid resolutions are commensurate with the reported resolution of finger representations in human sensorimotor areas. Within the sensorimotor hand area, detailed finger representations have been demonstrated with electrical stimulation [49], fMRI [133,134,179–181] and ECoG [9,13]. Within these sensorimotor hand areas, clinical ECoG grids with a standard resolution (mostly 4 × 8 – 8 × 8 electrodes, spaced 10 mm center-to-center with ˜2.3 mm exposed surface diameter) have been used to differentiate between finger representations [9], decode separate finger movements [8,10], decode five distinct hand postures [11], two different grasp types [173], decode reaching movements [182] and simple hand/elbow movements [82] using the changes in the high frequency band. One study [13] found that the activation foci of the different fingers (thumb to little finger) span ˜10 mm in both fMRI and ECoG, with an estimated distance of 3–4 mm between thumb, index and little finger. Another study [133] found a similar span in the center-of-mass distance estimates in fMRI, ranging from 6.6 mm to 16.8 mm. With regard to the distance between finger representations, the distance between centers of mass does not necessarily mean those yield optimal decoding performance, since overlapping finger representations between centers [134] may not affect center of mass location but it does affect discriminability of separate finger movements. As a result, one may expect optimal distance to be larger for decoding than for mapping. A study that decoded facial expressions from the sensorimotor cortex showed that only part of a high-density grid surface (15 × 15 mm to 20 × 20 mm based on 6 × 6 electrodes having 3 mm or 4 mm interelectrode distance) was enough to provide good decoding accuracy [183]. This supports the idea that a limited number of electrodes with optimal inter-electrode distance on the most essential area is enough to provide high decoding performance.

Grids with more electrodes at denser interelectrode distances (e.g. 5 × 5 electrodes, 4 mm distance, 3 mm size) provided only small increases in classification accuracies in comparison to smaller grids with a higher inter-electrode distance (e.g. 3 × 3 electrodes with 8 mm distance, 3 mm size). Similar to ECoG studies with standard grids, studies using high-density grids on sensorimotor cortex (4×8 and 8 × 8 electrodes, distanced 3 mm apart with 1.3 mm exposed surface diameter) were able to distinguish finger representations [13] and

decode four hand-gestures [14,93] using HFB changes. However, it remains difficult to directly compare the performance between low and high-density grids in individual subjects. We can only speculate on how an even denser grid would perform. A spatio-spectral analysis using 64 electrode-strips with an inter-electrode distance of 0.5 mm indicated an optimal distance of 1.25 mm [184]. A study combining spatio-spectral analyses from rat recordings and a dipole model suggested a minimal spacing of 1.7–1.8 mm for subdural and 9–13 mm for epidural grids to minimize signal overlap between electrodes [185]. However, current levels of fMRI voxel resolution are not likely to be accurate enough to simulate such electrode distances, given a certain point-spread due to non-discrete anatomical properties of the microvasculature that gives rise to the BOLD effect. Still, the decoding of more gestures, movements, or more complex behaviors [51,83,90,186] may benefit from denser grids. The methods we share here can be used by others to evaluate the decoding of more complex behaviors for BCI purposes.

Larger electrodes (up to 3 mm in radius) decoded better. There are two aspects that may play a role in this optimal simulated size: the averaging of fMRI signals across voxels, and the averaging across neuronal populations. First, fMRI BOLD signals contain noise that is reduced by averaging across voxels [187,188]. In our simulation, the electrodes with a larger radius included more underlying voxels. For classification, each virtual electrode served as an input feature to the classifier based on the average signal of all the voxels underneath the electrode. Therefore, larger electrodes average over a higher number of voxels, increasing the signal-to-noise ratio of every feature in the classifier. The increase in signal-to-noise ratio has likely contributed to classification accuracy. Second, field potential studies have shown that sampling neurophysiological signals from a larger patch of cortex can be highly informative [89,189,190]. A recent study [190] showed that ECOG recordings can provide more relevant information and higher decodability than microelectrode recordings. ECoG electrodes could effectively average over a neural population, negating the noise in the signal while preserving the common relevant information. Since the BOLD signal in a voxel is a representation of a neural population, the increase in classification accuracy that comes with larger electrode size (i.e. more voxels) might not be solely due to fMRI specific vascular noise, but could also be attributed to a reduction of noise by sampling from a larger neuronal population.

Although the fMRI BOLD signal is a more indirect measure of neuronal activity, it may serve as a good approximation of ECoG measurements. Several studies have shown that electrophysiology and BOLD signal changes correlate across time [19,20], that HFB power and BOLD correlate spatially with matching peak activity [21-23], that the non-linearities observed in fMRI can be predicted by ECoG HFB signal [25] and that the level of BOLD increase matches the level of ECOG HFB power increase across conditions [26-28]. One study [13] specifically combined fMRI measurements (voxel size of ~1.5 mm) and high-density ECoG measurements (8 × 4 electrodes, spaced 3 mm with a diameter of 1 mm) and found distinguishable finger representations that matched between the two techniques. The simulations based on the BOLD responses are likely to be indicative for what would be found with ECOG measurements.

The optimal grid resolution and placement is important for intracranial BCI applications that target patient populations. While our study included healthy participants, previous research suggests that hand representations are maintained in patients with an amputated arm [145]. Moreover, ECoG based BCI applications can benefit from fMRI localizer tasks to provide non-invasive identification of the informative region prior to surgical implantation [1]. Several BCI systems in patients with ALS or paraplegia have used fMRI to place grids on sensorimotor cortex [1,29–31] and visual cortex [191]. While fMRI is normally used only to identify the relevant region, the method described in this article can also advise on the optimal placement and configuration of a grid.

When an ECoG grid is implanted for BCI purposes, it is important to consider a reduced number of electrodes, given practical considerations such as the cost and complexity of high channel-count implantable amplifiers and real time signal processing [192,193]. In addition, the surgical procedure and implant could potentially carry a risk to the patient. Implanting a larger grid requires a larger surgical exposure, which may impose a slight risk for complication [194]. As our results suggest, the grid should be focused on the region of the brain that contains the most hand-gesture information. Our results provide a principled way of computing the tradeoff between grid size, density and decoding performance. The pipeline that we used for simulation could be used pre-surgically to locate the most informative area, find the grid configuration that would lead to the best performance and suggest one or more optimal positions on top of the most informative area for individual patients.

3.5 Conclusion

Most of the information encoding hand gestures is densely packed within a small area of the sensorimotor cortex. Our results show that optimal decoding of hand-gestures is achieved by placing a grid within this informative region. Grids of 3 × 3 electrodes with an inter-electrode distance of 8 mm and electrode size radius of 3 mm provided good classification accuracy. It has been assumed that densely-packed, small diameter, electrodes will provide the best resolution of functional representation. Based upon this fMRI-modeling approach, we might reassess this assumption. These densely spaced configurations might provide only a marginal benefit while being less practical in terms of complexity and cost of high channel-count implantable amplifiers, real-time processing and clinical invasiveness. As one might expect, positioning of the electrodes on the most informative area has a strong influence on the classification accuracy. The simulation techniques outlined in this article can be used more generally in clinical and research settings to identify optimal grid configurations and placements for neural prosthetics.

3.6 Acknowledgments

3.7 Supplementary material

Supplementary Figure 1. fMRI BOLD activity, information-mapping and most informative region during performance of hand-gestures per participant. The top row shows significant activation (based on a GLM with a single regressor, gesture vs rest, Bonferroni corrected). The middle row shows the averaged classification result of 200,000 searchlights that were placed at random dorsolateral over the frontal and parietal lobes. The bottom row shows only the positions of the searchlights with a classification accuracy above the 95th percentile, limited to the largest cluster. Together, these positions empirically identify the cortical hand-gesture area and were used as the centers for the placement of the grids that were simulated.
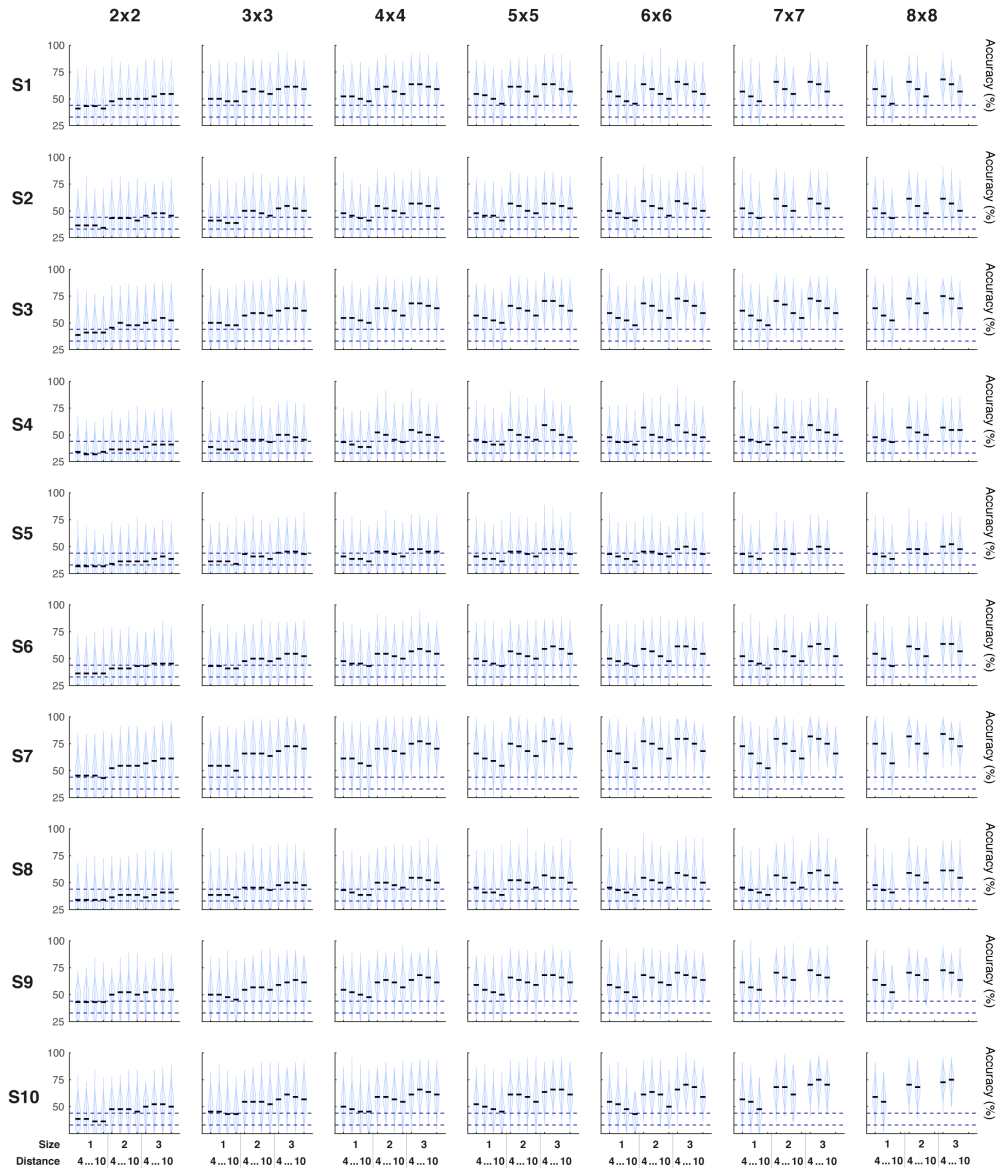
Supplementary Figure 2. Violin plots showing the classification accuracy scores for all grid configurations in all subjects. Placement was not limited to the most informative region. Rows represent the 10 subjects, columns the number of electrodes. Each column in each graph represents a different inter-electrode distance (4mm, 6mm, 8mm, 10mm) and electrode-size (1mm, 2mm, 3mm) combination. The violin reflects the distribution of scores, with a horizontal black line in every column to indicate the median. The lower blue dotted line indicates the chance level at 33%, while the upper blue line indicates the threshold (at 44%) above which an accuracy score is significantly above chance.
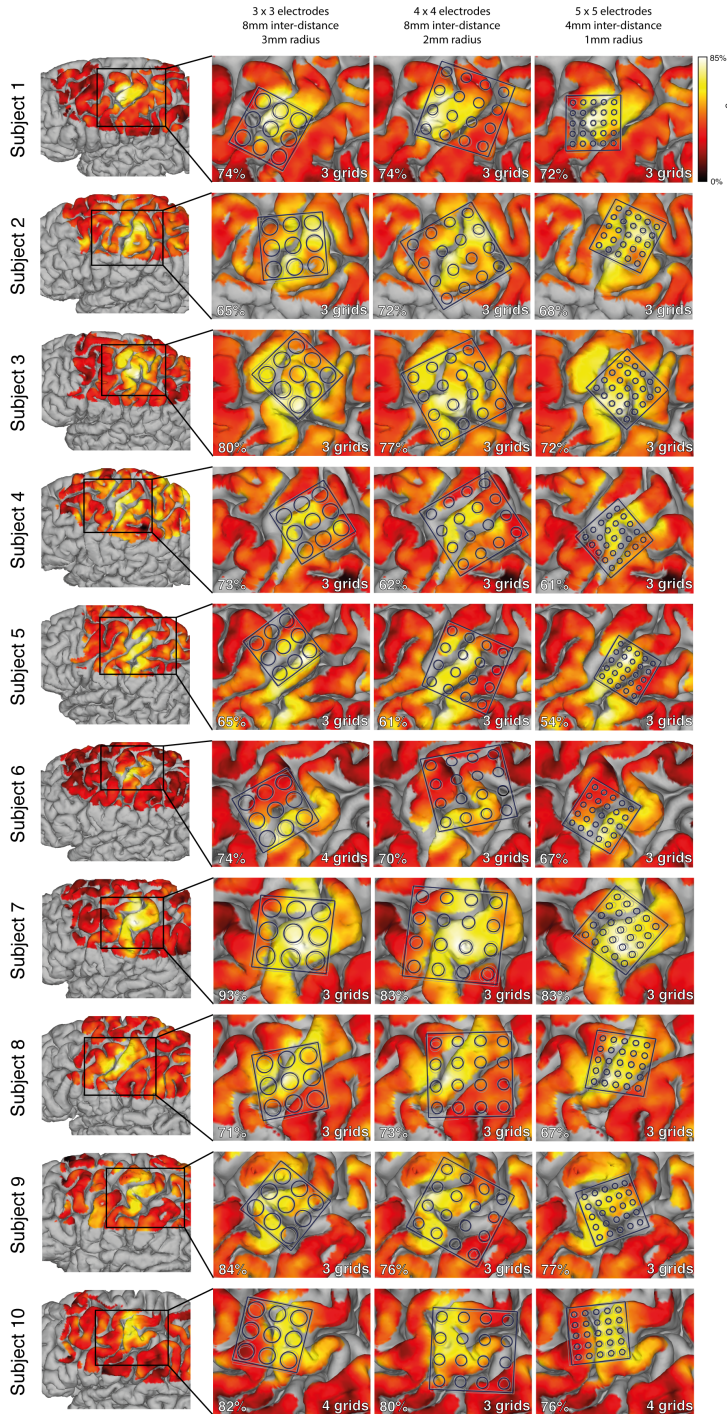
Supplementary Figure 3. Suggestions for the placement of three different grid configurations in all subjects. Each row represents one subject. The first column shows the presence of hand-gesture information over the brain based on searchlight classification. The other three columns suggest an optimal placement of three different grid configurations. Each of the suggestions is based on an agglomerative cluster analysis on the 3D positions of two corner electrodes of the 2,000 grid placements within a grid configuration. Grids were clustered together by euclidean distance with a cutoff distance of 2mm. Each image shows the grid-cluster that - within one grid configuration for a specific subject - had the highest average classification accuracy. The individual grids in that cluster are shown in grey and their average position in blue. The average classification accuracies over the grids in the cluster are shown in the bottom-left of each image, the number of grids that make up a cluster is noted on the bottom-right.

Clustering distance (euclidean)
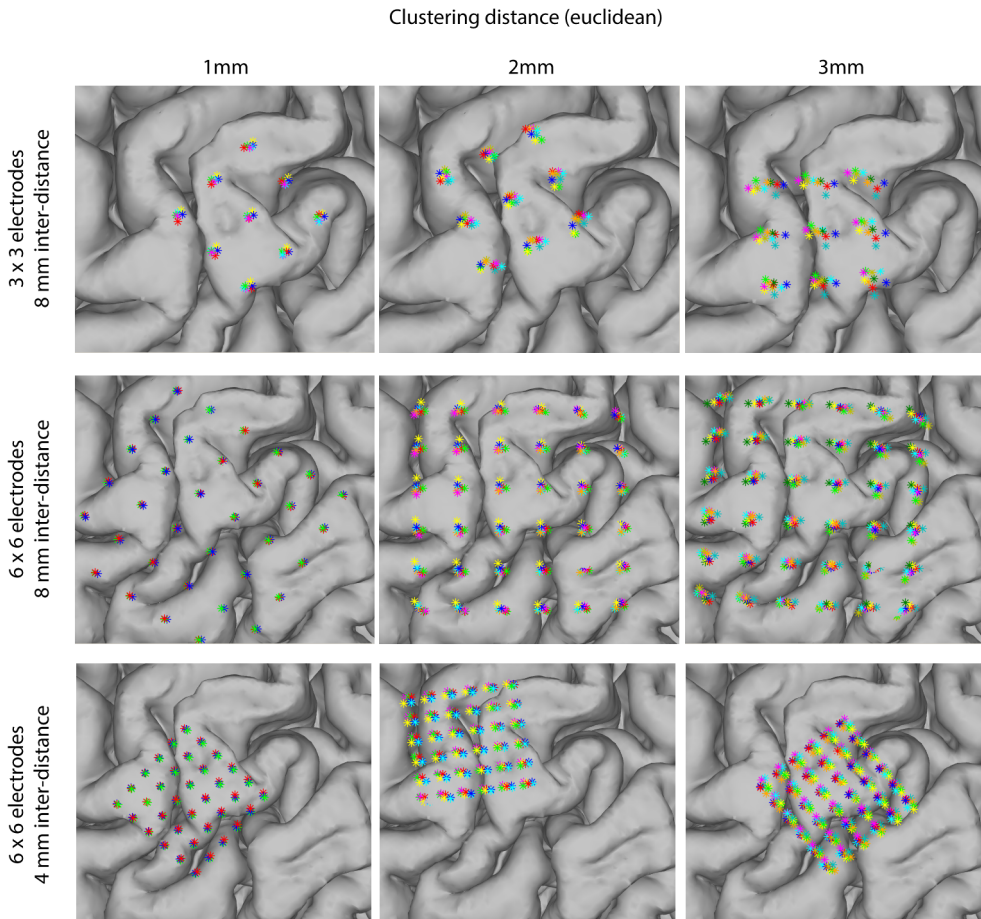
Supplementary Figure 4. Different euclidean clustering distances, number of electrodes and inter-electrode distances result in different clusters. The rows represent three different grid configurations that vary in number of electrodes and inter-electrode distance, for subject 10. The columns represent the three euclidean distance clustering parameters (1mm, 2mm and 3mm). For each image, the cluster with the highest number of grids was selected; each color represents a single grid in that cluster. The images illustrate how the resulting cluster will differ depending on the clustering method and parameters in combination with the grid configuration. Choices should be made, taking into account the margin of error in placement and the predicted classification performance.

Chapter 4

Chapter 4 - Towards an intuitive communication-BCI: decoding visually imagined characters from the early visual cortex using high-field fMRI

Abstract

In electrocorticography (ECoG), Brain-computer interfaces aim to provide people with paralysis with the possibility to use their neural signals to control devices. For communication, most BCIs are based on the selection of letters from a (digital) letter board to spell words and sentences. Visual mental imagery of letters could offer a new, fast and intuitive way to spell in a BCI-communication solution. Here we provide a proof of concept for the decoding of visually imagined characters from the early visual cortex using 7 Tesla functional MRI. Sixteen healthy participants visually imagined three different characters for 3, 5 and 7 s in a slow event-related design. Using single-trial classification, we were able to decode the characters with an average accuracy of 54%, which is significantly above chance level (33%). Furthermore, the imagined characters were classifiable shortly after cue onset and remained classifiable with prolonged imagery. These properties, combined with the cortical location of the early visual cortex and its decodable activity, encourage further research on intracranial interfacing using surface electrodes to bring us closer to such a visual imagery based BCI communication solution.

4.1 Introduction

People with locked-in syndrome (LIS) are locked into their own body due to severe paralysis. LIS is characterized by intact cognition, but a nearly complete loss of voluntary muscle control, including the ability to speak [195]. Typically, voluntary control over the eyes is retained, and eye movements or blinking are used in combination with a (digital) letter board to select letters and construct words to communicate. However, in certain situations (e.g. outside [1]) and for certain people (e.g. in cases of oculomotor impairment due to ALS [196]), eye control is not adequate or feasible. A promising alternative approach for communication in LIS is a brain-computer interface (BCI). BCIs record neural signals from the brain using dedicated sensors and translate features of the neural signals into control signals for a computer or other type of assistive technology [197].

Over the past decades, several BCI solutions for communication have been developed and tested, employing popular paradigms such as P300 evoked potentials, steady-state visually evoked potentials, sensorimotor rhythms and slow cortical potentials [197,198]. Similar to devices controlled by eye movements or blinking, these BCI systems often rely on a digital letter board, but instead of eye gaze, use a neural control signal to select the letters on the screen and spell words. A completely different and conceptually intuitive concept for controlling a communication-BCI could be based on visual mental imagery. Visual mental imagery is the experience of perceptual information in the absence of the appropriate retinal input; in other words: seeing a mental image. Using a visual imagery-based communication system, a user could imagine a character and thereby generate a unique brain activity pattern. Based on the recorded neural activity pattern, the BCI would be able to identify which character was imagined. The user would spell out words and sentences by sequentially imagining characters.

The early visual cortex is a logical source of signals for the decoding of visual imagery. It is known to be retinotopically organized [62–65] and is, therefore, likely to show distinguishable activation patterns. Indeed, it is possible to reliably reconstruct the BOLD response pattern for visually perceived characters from this area [76,77]. Moreover, several studies suggest that visual imagery involves the same neural mechanisms as visual perception [199–201] and generates similar retinotopically organized activity in the early visual cortex [202–205]. Research on the cortical representation of visual imagery confirms that aspects of scenes [206,207] and object-categories [59,208] are represented in extra-striate and higher-order visual areas, whereas the low-level features of the scenes are encoded in (pre-)striate visual areas V1 and V2. Research on the imagery of low-level features shows that motion [55], orientation [56–58], location [59] and shape [60,61] are represented in visual areas V1, V2, V3 and V4. Together, these data indicate that ample imagery-related information should be presented in the early visual cortex for the decoding of characters.

As a first step towards using visual mental imagery for communication-BCIs, we investigated whether it is possible to decode imagined characters from the early visual cortex. We used data acquired with a 7 T fMRI scanner, which allows for high spatial specificity (beneficial to decode neural activity patterns [13]) and a high signal-to-noise ratio [209]. We

measured the BOLD activation patterns associated with the visual imagery of three different characters and applied multivoxel pattern analysis (MVPA) to discriminate between these patterns.

4.2 Method

Participants

Sixteen healthy participants (14 female, age 24 ± 2.9 years) participated in the study. Four of the participants (3 female, age 26 ± 2.6 years) were asked to repeat the experiment in a second session. Participants gave written informed consent to participate, in accordance with the World Medical Association Declaration of Helsinki (2013) .

MRI data acquisition

Functional MRI scans were acquired using a 7 T Philips Achieva MRI system with a 32-channel head coil. Functional data was recorded using an EPI sequence (TR/TE 1500/25 ms, FA 70 degrees adjusted for the B1 transmit field in the visual cortex, 25 slices, acquisition matrix 96 × 96, slice thickness 2.00 mm, no gap, 1.98mm in-plane resolution). A T1-weighted image (TR/TE 7/2.76 ms, FA 8 degrees, resolution 0.98 × 0.98mm in-plane, slice thickness 1.0 mm, no gap) was acquired for anatomical reference. Participants were provided with in-ear headphones through which auditory cues were presented. Additional hearing protection covered both the ears and headphones. Computer tasks were projected onto a mirror attached to the head coil.

Tasks

Two tasks were administered during the experiment: a visual mental imagery task ('imagery task') and a visual perception task ('perception task'). During both tasks the participants were presented with a grey screen that contained the outline of a black square (~11 degrees visual angle) with a black dot in the middle. Participants were asked to keep their eyes open and to look at the dot at all times. During every trial of the perception task, one of three characters was shown in white, full size inside the black square (figure 1). During the imagery task, participants were asked to imagine the character inside the black square (figure 1). We used three characters: the letter 'x', the plus sign '+' and the letter 'o'. The characters 'x' and '+' were chosen for their strong visual-topographical contrast (i.e. horizontal versus diagonal). The 'o' character was added as it cannot be rotated to another character.
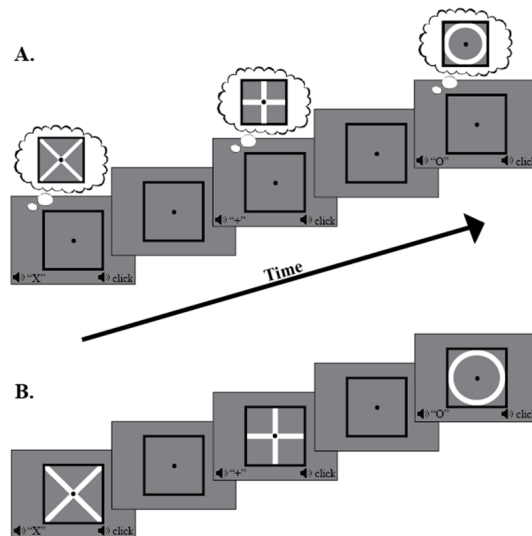
Figure 1. Schematic overview of the imagery task (A) and perception task (B). A spoken audio cue indicated whether the letter 'x', the plus sign '+' or the letter 'o' should be perceived or imagined inside the square while fixating on the black dot. The requested symbol had to be imagined or perceived until a soft click sound was played.

Each task consisted of 45 trials and took approximately 12 min to complete. In both tasks, at the beginning of each trial, an audio cue indicated which character would be presented or should be imagined. A click sound indicated the end of the trial, when the character would disappear or a person would have to stop imagining. In the imagery task, the duration of each trial (i.e. the time between cue and click sound) was either 3, 5 or 7 s, with an inter-trial-interval (ITI) of 10 s. In the perception task, the duration of each trial was either 1, 3 or 6 s for the first 8 participants; and was later changed to a constant of 5 s for the remaining participants as the task proved to be reliable regardless of duration variations. An ITI of 12 s was used for all participants in the perception task.

The three characters and their different durations were presented at random within each task. Due to technical reasons, datasets of four tasks spread over three participants were incomplete. However, a bias towards any of the characters or durations was prevented by randomization and the data could still be used.

Procedure

Before entering the scanner, participants were instructed on both tasks, which included a short presentation of the perception task. The experiment started with a first run of the imagery task, followed by one run of the perception task, the T1 weighted anatomical scan, and a second run of the imagery task. We deviated from this task order in two participants: for one participant, the anatomical scan was acquired first, and another participant first performed the perception task. For another two participants, logistic reasons prohibited the acquisition of the second imagery run.

Based on their decoding performances in the first session, the two worst and the two best scoring subjects were invited and repeated the experiment in a second session to assess the reproducibility of the performance difference.

Preprocessing

All preprocessing steps were performed using SPM12. Anatomical scans were segmented to produce MNI-to-native deformation fields, which were used to map an early visual cortex mask to native space (see below in Signal selection). Functional scans were realigned to correct for motion, and activation t-maps were generated for each character using a GLM analysis where each of the three characters was taken as a separate regressor. All analyses were carried out in native space without smoothing since spatial transformations or averaging could result in the loss of decodable information.

Signal selection

Signal processing, analysis and classification procedures were implemented using custom MATLAB (Mathworks Inc.) scripts. In order to limit the region of interest (ROI) to the early visual cortex (i.e. V1, V2 and V3), a mask was created in MNI space using a probability map that reflected the likelihood of a voxel being assigned to a specific visual area [210]. All voxels with a likelihood of 20% or higher to be V1, V2 and V3 were included in the mask. The mask was manually edited to include missing voxels that were completely surrounded by included voxels and was extended posteriorly to ensure that all V1 voxels would be included after transformation into native space. For every subject, the early visual cortex mask was converted from MNI space to the native anatomy, coregistered and applied to the aligned functional scans.

Feature reduction for classification was performed by selecting for each participant, the 105 voxels with the highest t-values of each character per task. The number of 105 voxels was chosen based on the mean decoding performance of the perception task over all participants. The union of the voxel selections per character was used as feature set in further analyses. The raw BOLD signal of each feature was subsequently detrended (linear, quadratic and cubic) and normalized (division by it's mean and multiplication by 100) to reflect the percentage signal change. In most analyses, the two imagery runs were combined

(see classification below) and the union of the voxels from the t-maps of both runs (i.e. six t-maps with 105 voxels each) were used as features.

Analysis

Decoding the characters in both the perception task and imagery task(s) was performed using the same classification method and parameters. The perception task was used to establish an optimal number of voxels for feature reduction, to be used over all participants for both tasks.

For classification, the first five volumes of each run were discarded to exclude a task-onset BOLD response. In the time-domain, for each trial, the functional volume with the highest average BOLD signal over voxels in the ROI was selected under the assumption that this timepoint would be the most informative. Since it is not known at which moment in time the peak of the neuronal response would occur, we limited the search for the highest average BOLD signal per trial to the period between the predicted HRF peak assuming a transient response and the theoretical HRF peak assuming a sustained response (given the duration of the trial). This time window was then extended to include one additional volume before and after the window, to cope with potential variation in the behavioral onset. Per trial, only the timepoint with the highest average BOLD signal was selected and used in a Support Vector Machine (SVM) with a linear kernel for training and classification. Multi-class classification was achieved by applying a one-versus-all classification scheme, where every class is classified against the data of all other classes together and the winner (furthest from the hyperplane) takes all. The decodability was determined using a leave-one-out cross-validation and is expressed as a classification accuracy score, which is the percentage of trials predicted correctly.

Before concatenating the data of the two imagery runs, we first classified the runs separately and tested their performances using a two-tailed paired sample t-test to ensure no systematic difference existed between the runs. The decodability of the three characters from the early visual cortex was tested by classifying the characters from the unified imagery runs. In the two cases where participants performed just one imagery run, we based the decodability on that single run. Classification scores were tested for significance using a Monte Carlo distribution based on 20.000 permutations per dataset [131,211].

To investigate the variance in classification accuracy, we considered the scores on both the perception and imagery task. Perception requires no action from the participant and should be perfectly decodable [76,77]. A lower classification accuracy on the perception task would imply the influence of factors unrelated to the visual system, such as mental fatigue or head motion. Therefore, we investigated whether there was a correlation (across subjects) between head movement in the scanner and the classification scores in the perception and imagery tasks. This is relevant, since no smoothing was applied and even small motions are known to influence the prediction accuracy of supervised learning models used for classification [212]. To quantify head movement, the motion correcting values produced by SPM12 in the realignment of the imagery runs were used. As a measure of translational

movement, we took the (x, y and z) motion correction values between time points and averaged their Euclidean distances. A head rotation measure was obtained by taking the mean over the absolute (pitch, yaw and roll) rotational corrections between time points.

The classification performance of imagery was further evaluated by focusing on the individual characters. Confusion matrices were produced to provide detail on the classification accuracy per character and classification errors. For each character, the sensitivity was used to indicate how well that character was classified. We performed chi-square tests on each character combination per participant to test whether the classifier was able to distinguish the correct character from each of the other characters. The chi-square tests were corrected for multiple comparisons using the false discovery rate method [213].

Decodability over time and the effect of imagery duration on classification performance was investigated by grouping trials with the same duration (3, 5 or 7 s) together. Only the participants for whom classification of imagined characters was significantly above chance were included in these analyses to prevent non-imagery related noise. For each subject, each group of trials was classified at sequential time points from trial onset. To test whether a specific trial duration would result in a higher score, we performed a within-subject ANOVA on the scores in the different duration groups, taking for each duration the point in time at which (on average over participants) the classification accuracy was maximal. To test the decodability over time, a repeated-measures ANOVA was performed, taking both the trial duration and time from trial onset as within-subject factors. Since the first time-points after trial onset cannot contain decodable information yet and their accuracy scores will only add noise to the ANOVA's mean, we included only the time-points in the analysis from the point where the averages of all trial durations are above chance level.

4.3 Results

For all participants, the classification accuracy on the perception task was significantly above chance level with an average of 94% (N: 16, SD: 6%, range: 80–100%). For the imagery task, most participants scored significantly above chance level (figure 2) with significant averages of 54% in the first imagined run (N: 16, SD: 19%, range: 30–93%) and 52% in the second imagined run (N: 14, SD: 18%, range: 30–77%). The performance between the two imagery runs was consistent (r = .54, p = .024; table 1) and did not differ significantly (paired t-test, t(13) = .180, ns). Therefore, we combined the first and second imagery runs for further analyses. Classification of the combined imagery runs resulted in a significant average accuracy of 54% (N: 14, SD: 23%, range: 25–95%).
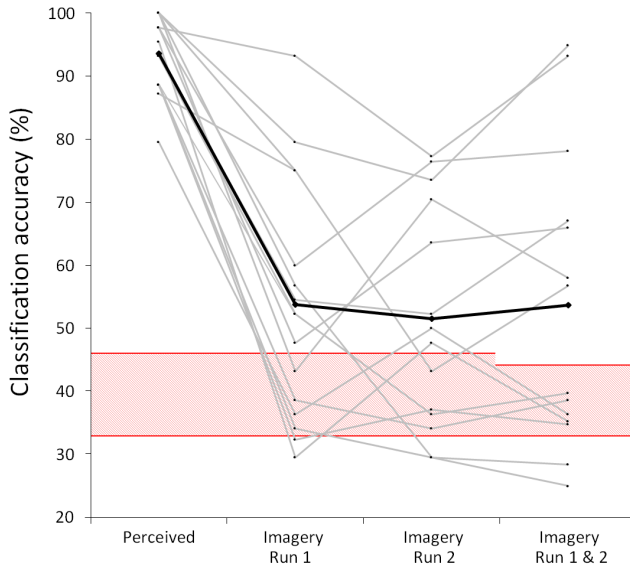
Figure 2. Classification accuracies of the perception run and the imagery runs. The grey lines represent the accuracy scores of individual participants, the black line the average over participants. The lower red line shows the chance level at 33%, while the upper red line indicates the threshold above which the decoding accuracy was significant (46% for single runs and 44% for the combined imagery runs).

Table 1. Correlations between the classification accuracies in the perception and imagery runs.

	Imagery run 1	Imagery run 2	Imagery run 1 & 2
Perception	r = .45, n = 16 *p* = .041 *	r = .44, n = 14 *p* = .058	r = .51, n = 14 *p* = .031 *
Imagery run 1		r = .54, n = 14 *p* = .024 *	r = .78, n = 14 *p* < .001 **
Imagery run 2			r = .89, n = 14 *p* < .001 **

** Correlation is significant at the 0.01 level (1-tailed)
 * Correlation is significant at the 0.05 level (1-tailed)

Classification accuracies on the perception task displayed a modest variance (SD: 6%), while the imagery task showed a relatively large variance (SD: 23%). The significant positive correlation (r = .51, *p* = .031; table 1) between the scores on the perception task and imagery task suggest that there are subject or session-specific factors which influence the performance on both tasks. Head-motion inside the scanner was considered as one. However, only in the imagery runs did head-motion have a significant negative influence on classification scores (translation: r = −0.41, *p* = 0.025; rotation: r = −0.58, *p* = 0.001; figure 3). In the perception task, there was no significant correlation between head-movement and the classification scores.
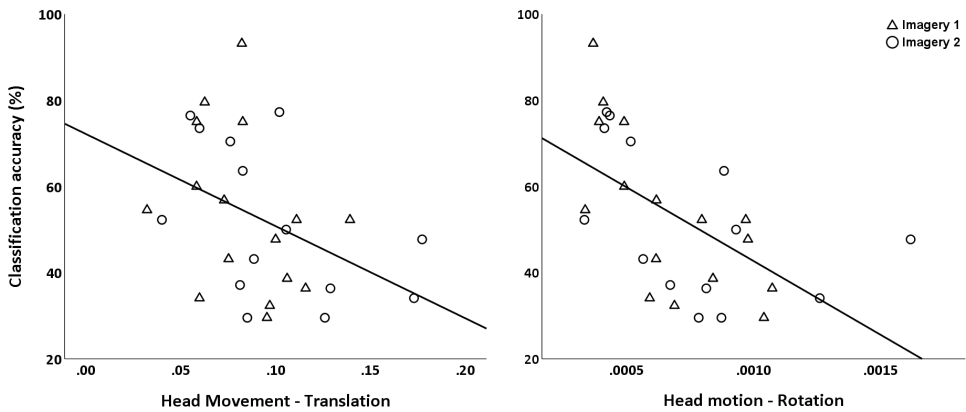
Figure 3. Classification accuracies plotted against the head motion parameters. The left panel shows the relation of accuracy against the average head translation over time in millimeters (r = −0.41, p = 0.025). The right panel shows the relation to average head rotation degrees (r = −0.58, p = 0.001). The black lines indicate the trends in the data.

The classification accuracy per imagined character was investigated using a confusion matrix (figure 4). The matrix demonstrated that all three characters showed moderate, yet significant, sensitivity values (54%, 51% and 56%). There was no significant difference between the classification accuracy of the three characters (ANOVA, F(2, 39) = .132, *ns*).

Figure 4. Confusion matrix with the average classification scores of the separate characters for imagery. Each row represents the imagined character. The cells in each row represent how that character was predicted by the classifier.

Chi-square tests on the classification scores for each character combination (x+, xo and +o; figure 5) per subject showed that it was only possible in a subset of six participants to significantly distinguish all characters from each of the others; while in six participants

none could be distinguished significantly. The 'x' and the '+' were classified wrongly (confused) in slightly more participants than the other combinations.

	Participants															
x +		■	■			■						■		■	■	
x o		■	■			■			■	■		■		■	■	
+ o		■	■	■		■			■			■		■	■	

Figure 5. Discriminability between characters for each participant. Each column represents one participant. The rows indicate the results of chi-square tests between the different characters; each cell indicates whether a character pair was significantly distinguishable (blue) or not (white) for each participant.

To examine the classification accuracies over time, we included seven participants who showed significant classifications on the combined imagery runs and two participants who classified significantly but had only a single imagery run. Figure 6(a) shows the average BOLD responses on each of the trial lengths over the voxels used for classification, showing that the BOLD response of each trial length peaks 6 to 7 s after trial onset.

The classification accuracies over time (figure 6b) show that 6 s after trial onset the BOLD signal carries enough information to decode imagined characters above chance level for all trial lengths (3, 5 and 7 s). Comparing only the timepoint that held the maximum score for each duration showed that there was no significant difference ($F(2, 16) = 1.62$, *ns*) in maximum classification accuracy between the durations.
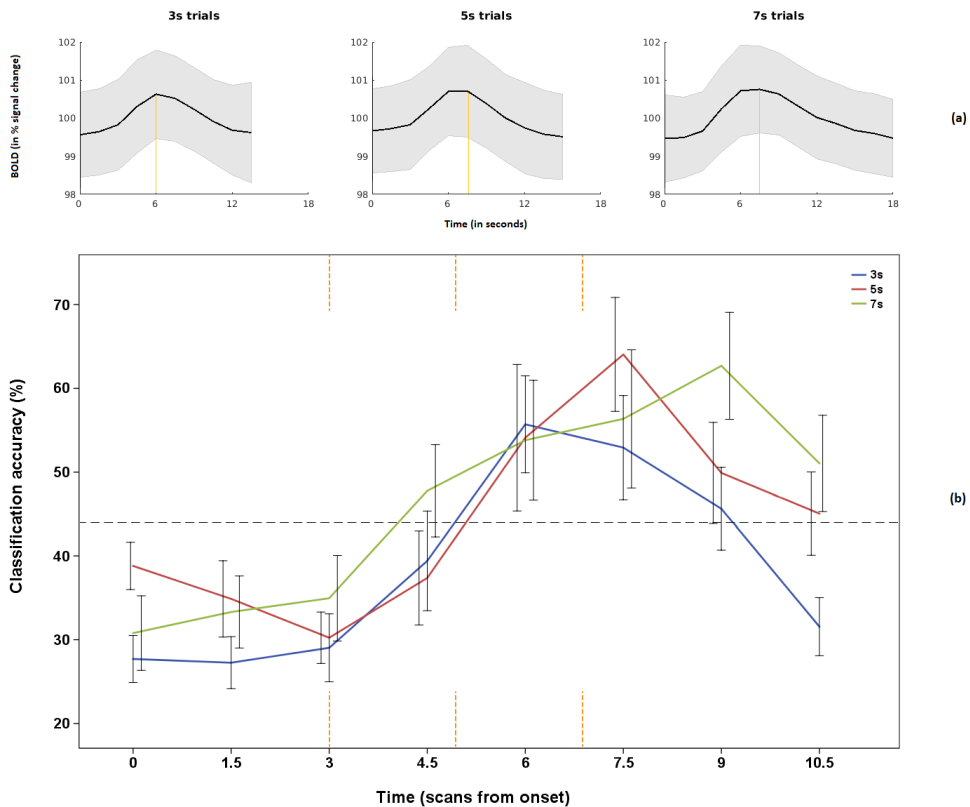
Figure 6. (a) The BOLD response patterns to visual imagery over time for different trial durations over the voxels used for classification (n = 9, best performing subjects). The black line indicates the amplitude of the BOLD signal in the voxels, averaged over trials. The shaded area indicates the standard deviation of the data. The vertical orange lines indicate the maximum. (b) Classification accuracies of imagery durations (trial lengths) classified at sequential times from trial onset. The significant threshold is shown as a dotted black line. The vertical orange lines indicate the trial offsets for 3, 5 and 7 s. Bars denote the standard error.

To test the decodability over time, a repeated measures ANOVA was performed taking the scores on four points in time into account (from 6 s after onset, to 10.5 s after onset). Trial duration was not a significant determinant of classification accuracy ($F(2, 16) = 1.827$, *ns*), whereas the moment of classification after trial onset was a significant factor ($F(3, 24) = 5.503$, $p < .01$).More importantly, a significant interaction existed between trial duration and time of classification ($F(6, 48) = 3.519$, $p < .01$); contrasts revealed that when comparing 3 s trials to 7 s trials, the 7 s trials performed significantly better 10.5 s after trial onset, in contrast to 6 s after trial onset where this was not the case ($F(1, 8) = 12.479$, $p < .01$, r = .61).

Four participants were invited to repeat the experiment in a second session and showed consistent performance on the imagery task (figure 7).
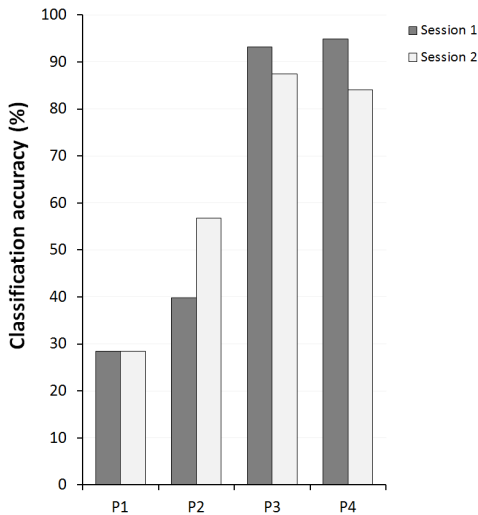
Figure 7. Classification accuracies of the imagery tasks for the participants who performed the experiment a second time.

4.4 Discussion

This study investigated whether visually imagined characters can be decoded from the early visual cortex. Using support vector machine learning, we were able to classify single trials of three imagined characters significantly above chance level for the majority of the participants. On average, each of the imagined characters could be classified equally well, with accuracies ranging between 51% and 56%. Within subjects, the classifier seemed less able to discriminate between 'x' and '+' in slightly more participants than other character combinations. Although speculative, this may be explained by the fact that both the 'x' and '+' cross the center of the retina, whereas the 'o' does not; or because they are rotated versions of each other. Given the retinotopical organization of imagery [202-205] people might imagine a version closer to the other, resulting in less distinguishable neural activity patterns.

The classification accuracy results showed a considerable variation between participants, particularly of the imagined runs (between 25% and 95%). To explain the variance in the imagery task, we first investigated the performance on the perception task. Since perception should be highly decodable [76,77] without an effort from the participant (except passive watching), each participant should score high on the perception task. However, our results showed that, while the average accuracy on the perception task was very high (95%), it still varied between 80% and 100%. The presence of lower than 100% scores could indicate an influence of factors unrelated to the visual system (e.g. mental fatigue or head motion). In addition, correlational analysis on the classification accuracies of the perception and imagery tasks revealed a moderate yet significant positive relation. Therefore, it is plausible that the same factors have a negative impact on the performance of both tasks. One of such factors was head-motion inside the scanner. A correlational analysis on the motion correction values and classification accuracies in the imagery task revealed a

significant negative relation, indicating a negative influence of head-motion on classification accuracy. Results of the perception task had no significant relation to head-motion. This suggests that there is either a ceiling effect in the scores of the perception task which precludes finding a clear relation between head motion and classification accuracy, or head-motion is a factor that influences solely the imagery task.

Although head-motion explains part of the variation in the imagery task, much is still unaccounted for and could be attributed to imagery specific factors such as vividness of visual imagery, which is known to be strongly related to early visual cortex activity [214,215]. In addition, physiological differences between the brains of the participants could be of influence. The cerebral blood flow in the primary visual cortex is related to the mental processing of imagery [216] and the size of area V1 is associated with the strength and precision of visual imagery [217]. Moreover, it is suggested that humans are capable of mentally representing visually imagined information in more than one way [218–220], which is likely to affect decodability. One approach to minimize this source of variance could be task practice. Participants in this study did not practice beforehand. A study that performed single-trial classification on complex hand movements showed that decoding accuracy is predominantly limited by the consistency between classes [92]. It is likely that a covert task, such as visual imagery, is bound to this limitation to an even larger extent, indicating that practice of the task could provide more consistency and better decodability.

The results on decodability over time showed that all trial lengths - including the short 3 s trials - were significantly decodable at 6 s after trial onset. Decodability did not seem to benefit from prolonged imagery, as longer trial lengths did not result in higher classification accuracy scores. However, the duration of the trial did significantly influence the decodability in time, in that longer trial durations remained significantly classifiable at time points later in time than shorter trial durations. Exploration of the BOLD signal in the voxels that responded to visual imagery showed that each of the trial durations resulted in a peak in the BOLD signal 6 to 7 s after onset. This coincides with the first decodable timepoint, confirming the link between the neural activation and decodability.

The neural characteristics of imagery and decodability over time are relevant for a BCI. The immediate neural responses and rapid decodability after trial onset on all trial lengths correspond with the typical timing of the BOLD response reported for visual stimulation experiments [221,222], suggesting that there was barely any delay in the visual imagery process and that the time difference between cue onset and the imagery related BOLD response is largely determined by the nature of the BOLD response itself, rather than by the cognitive aspects of the visual imagery task. This would provide a BCI with an immediately decodable response that conceptually allows for consecutive decoding (i.e. spelling) of imagined characters. The prolonged decodability over time can be used to find an optimal balance between spelling speed and reliability by using more or less timepoints in the decoding algorithm, however, this is not investigated in the present study.

The most viable communication-BCI for locked-in patients would allow patients to spell consecutive letters in order to build words and sentences. Visual imagery would fit this

requirement in an intuitive way by allowing patients to simply visually imagine the letters. Yet, there are three issues to consider when translating our results into a visual imagery based BCI. First, our study uses the fMRI BOLD signal for decoding visual imagery, while the most practical option for a patient will most likely involve the measurement of electric potentials. Measuring electric potentials has the benefit of a higher temporal resolution and more mobile equipment. Importantly, it has been demonstrated that hemodynamic measurements in fMRI correlate well with electrical measurements of neuronal activity [19,22,223] and can be used to pre-surgically determine the location for subcranial electrode grids [1,67,165]. It is therefore probable that the ability to decode fMRI signals will translate to the ability to decode intracranial electrical potentials. Secondly, outside of the experimental setting, visual perception is likely to interfere with the decoding of visual imagery. One solution to this problem would require the patient to look at a plain black surface when using the BCI or close the eyes. The difference between high early visual cortical input during perception and low input during imagery (while looking at a black surface) could be used by a BCI solution to tell whether the patient actually intends to use the BCI solution to spell. And third, our experiment featured the decoding of three characters. For a BCI spelling device, it is essential to extend the number of characters to allow for the spelling of meaningful words.

Our findings on decoding imagined characters from the early visual cortex are in line with earlier studies that demonstrated the decodability of visually imagined motion [55], orientation [56–58], location [59] and - by using an encoding model on low-level features - scenes [207]. Another study has tried to decode imagined shapes but reported only on decodability from the anterior and posterior subregions of the lateral occipital complex [60]. Notably, one study asked participants to imagine the sounds and scene corresponding to an auditory cue (either forest, people or traffic), and was able to decode the scene category from both the auditory cortex and the early visual cortex [224]. Recent work with six well-trained subjects using sophisticated methods gave promising results, where perception was used to train models that could predict the voxel activation patterns of imagery [225]. Our results extend on these earlier findings by showing that symbols can indeed be decoded from the early visual cortex without training and remain decodable with prolonged imagery.

An important limitation of the study is the covert nature of visual imagery, in which there is no behavioral performance to monitor. Another potential source of performance variability in both the perception and imagery task is related to changes in eye gaze. If participants were to ignore the instruction of fixating their view on the dot in the middle of the screen during trials, then strategic eye movements might cause classification to be based on differential activation patterns elicited by eye movements. Unfortunately, due to the strong magnetic field and small bore size of the 7 T MRI scanner, it was not possible to perform eye-tracking to control for eye-movements.

4.5 Conclusion

Our study confirms that visually imagined characters can be distinguished from one another using the BOLD signal changes in the early visual cortex. The results indicate that maximum classification accuracy can be reached already shortly after the onset of mental imagery (i.e. it does not take much time to generate a mental image before it can be classified) and that the imagined character remains classifiable with prolonged imagery. Given the close relationship between the hemodynamic measurements in fMRI and electrical measurements of neuronal activity, the concept of visual imagery may be suited for techniques that measure from the cortical surface (e.g. ECoG) and therefore has the potential to be used as a BCI solution for patients. Future research should extend on the number of characters and investigate whether practice reduces the large variability in performance and improves the decoding accuracy.

4.6 Acknowledgments

Chapter 5

Chapter 5 - Rapid acquisition of dynamic control over DLPFC using real-time fMRI feedback

Abstract

It has been postulated that gaining control over activity in the dorsolateral prefrontal cortex (DLPFC), a key region of the working memory brain network, may be beneficial for cognitive performance and treatment of certain psychiatric disorders. Several studies have reported that, with neurofeedback training, subjects can learn to increase DLPFC activity. However, improvement of dynamic control in terms of switching between low and high activity in DLPFC brain states may potentially constitute more effective self-regulation. Here, we report on feasibility of obtaining dynamic control over DLPFC, meaning the ability to both in- and decrease activity at will, within a single functional MRI scan session. Two groups of healthy volunteers (N = 24) were asked to increase and decrease activity in the left DLPFC as often as possible during fMRI scans (at 7 Tesla), while receiving real-time visual feedback. The experimental group practiced with real-time feedback, whereas the control group received sham feedback. The experimental group significantly increased the speed of intentionally alternating DLPFC activity, while performance of the control group did not change. Analysis of the characteristics of the BOLD signal during successful trials revealed that training with neurofeedback predominantly reduced the time for the DLPFC to return to baseline after activation. These results provide a preliminary indication that people may be able to learn to dynamically down-regulate the level of physiological activity in the DLPFC, and may have implications for psychiatric disorders where DLPFC plays a role.

5.1 Introduction

Working memory (WM) function is conceptually associated with temporary information storage and processing [226]. Many higher cognitive abilities such as reasoning, planning and problem solving are dependent on WM. A number of behavioral studies have shown that both the storage capacity and the ability to process information are limited [227-229]. With practice of certain WM tasks, performance improves, while brain activity in the associated network of regions declines [100], suggesting that brain activity adjusts to the need for cognitive control [101]. Various psychiatric disorders have been associated with WM dysfunction, in which the dorsolateral prefrontal cortex (DLPFC), a key region of the WM system, could play a role. Patients with schizophrenia show impaired WM performance, where the DLPFC responds differently to WM demands in comparison to healthy people [230-232]. Individuals with depression show increased DLPFC activity on WM tasks [233,234]. For Major Depression, neuromodulation of the DLPFC using rTMS is currently applied therapeutically [235,236]. Disruption of WM function has also been associated with drug dependence [237]. As such, the DLPFC can be regarded as a potential target for treatment of WM deficits associated with psychiatric disorders, where the ability to learn to self-regulate activity of the DLPFC is of interest for the development of novel treatment options.

The results of neurofeedback studies suggest the possibility that WM function can be improved through the use of neurofeedback in real-time (rt-) fMRI experiments [238]. In such experiments, the blood oxygenation level-dependent (BOLD) signal or pattern in a specific region of interest (ROI) is translated into information that can be used by the subject in real time [239]. It has already been shown that self-regulation of activity through neurofeedback can be trained for brain areas such as the anterior cingulate cortex (ACC) [240], amygdala [241], premotor areas [242], visuospatial attention [243,244] and auditory cortex [245].

The DLPFC has been attributed a pivotal role in WM [66,246-248]. Neurofeedback studies that target the left DLPFC have predominantly focused on the possibility to increase activity [249-252]. However, WM function may also benefit from direct dynamic control of brain activity levels, in other words the capability to increase and decrease activity in brain regions when needed.

In the current study, we used neurofeedback to examine the possibility to learn to dynamically control DLPFC activity. The magnitude of left DLPFC activity, generated during performance of a WM task in a 7T MRI scanner, was visually presented to healthy volunteers in real time. Training encompassed practice of control over a figurine in a game setting, where the level of activity in left DLPFC determined the vertical position of the figurine. A control group performed the identical task, but with sham instead of real feedback. We used a 7T MRI scanner to obtain a sufficiently accurate and strong measure of local neural activity to allow for real-time dynamic control learning.

The DLPFC is part of the dorsolateral prefrontal circuit, which projects from the DLPFC to the dorsolateral caudate nucleus, the lateral dorsomedial globus pallidus and connects via the ventral anterior and mediodorsal thalamus back to the DLPFC. It is possible that

neurofeedback on the DLPFC influences other regions in this circuit. Therefore we perform a cluster analysis to see if other brain regions are affected.

We hypothesized that subjects would be able to learn to regulate DLPFC activity using the information provided by the rt-fMRI neurofeedback. In order to understand how neurofeedback practice affected the ability to regulate activity, we analyzed the temporal characteristics of the BOLD signal before and after the practice periods. In addition, we explored whether other regions besides the DLPFC are affected as a result of the neurofeedback.

5.2 Experimental procedures

Participants

Twenty-four healthy participants between the age of 19 and 30 years (11 male, 13 female; mean age 23.54; SD 2.81 years) were included in the study after giving written informed consent. Exclusion criteria were history of psychiatric illness, pregnancy, metal objects in or around the body or claustrophobia. The study was approved by the local medical ethics committee, in accordance with the Declaration of Helsinki (2013). One participant was excluded from analysis due to scanner failure. Participants were randomly assigned to an experimental or control group. Thirteen participants were included in the experimental group and eleven in the control group. The groups are not exactly equal due to dropout resulting from MRI scanner issues.

MRI

FMRI was performed using a 7T Philips Achieva system, with a 32-channel head-coil. Functional data was recorded using an EPI sequence (TR/TE: 2.0 s/25 ms, FA: 70, 39-axial slices, acquisition matrix 112 voxels × 112 voxels, slice thickness 2.2 mm no gap, 2.19 mm in plane resolution). A T1-weighted image was acquired for anatomy (TR/TE: 7/2.76 ms; FA: 8; resolution 0.98 ×0.98 ×1.0 mm). Computer tasks were projected onto a mirror attached to the head coil.

Tasks

During the experiment a neurofeedback task and a count-back task were administered. Both tasks require mental calculation to reliably activate the left DLPFC [67].

The neurofeedback task consisted of a man on a ladder positioned against an apple tree. The position of the man on the ladder was controlled in real-time by the magnitude of DLPFC activation, allowing it to ascend or descend (see figure 1). By modulating DLPFC activity, participants were able to pick the apples at the top of the tree and bring them back down, requiring the crossing of a top and bottom threshold, respectively. To activate the DLPFC participants were to covertly count back in steps of 7, and to deactivate participants

were to let their mind wander freely. Instruction was to pick as many apples (alternately crossing the two thresholds) as possible in 2.5 min. The number of apples picked within each 2.5 min run was used as a behavioral performance score.
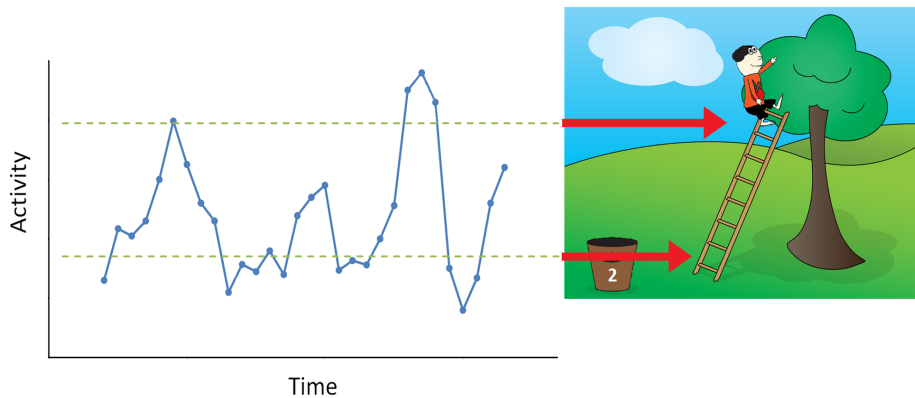
Figure 1. Neurofeedback task. The DLPFC normalized signal mean translated to a position on the ladder.

The count-back task was used to assess the pattern of activity in the DLPFC. Participants alternated between 20s of rest and 20s of counting back for 3 min. To assist participants, a random number between 600 and 900 was displayed on the screen as a starting point during count-back blocks.

Procedure

Table 1 gives an overview of the runs and tasks in the experiment. The experiment was single blind with both groups receiving the same instructions. Participants were informed that during the neurofeedback tasks there would be a delay between their cognitive effort (rest vs counting backwards) and the visual representation of the brain signal due to the nature of the BOLD signal. With regard to the training tasks the participants were asked to experiment within the count back paradigm in order to improve their performance on the task.

Table 1. Experiment setup

Scan run	Duration	Task	Purpose
0	3 min	-	Preparatory scans and setting the scan field
1 (EPI)	3 min	count-back	Localization of ROI for neurofeedback tasks
2 (T1)	5 min	-	Acquisition of anatomy image
3 (EPI)	30 min	count-back	Determine subject specific range of activation in ROI
			Pre-test brain activity
		Neurofeedback	Pre-test neurofeedback performance
		neurofeedback (5x)	Training
		Neurofeedback	Post-test neurofeedback performance
-	5 min		Rest
4 (EPI)	3 min	count-back	Post-test brain activity

After giving informed consent participants were positioned inside the scanner. Instructions were given between tasks. During the first (preparatory) scans the participants were asked to relax. They then performed the count-back task for the first time, followed by a 5 minute rest period during which an anatomical scan was acquired. After the anatomical scan they were presented with eight more tasks which started with another count-back task, followed by the neurofeedback task seven times with half a minute of rest in-between each of the tasks. After the last run they would have 5 min of rest without scanning. Then finally they had to perform one more count-back task before being taken out of the scanner.

Neurofeedback

Feedback was based on BOLD levels in left DLPFC. The neurofeedback software was written in MATLAB (MathWorks) and integrates functions of SPM8. Since the exact location of brain activity within the DLPFC varies per person, the first count-back task served to localize the most active area in the DLPFC region. To limit the ROI to the DLPFC we used a global DLPFC mask converted from MNI space to native space after the first task. Immediately after the task – while the participant was still in the scanner –the functional scans from the task were aligned, smoothed, a GLM including detrending was performed and a t-map was generated online. Then, the 200 most active voxels within the global DLPFC mask constituted a subject-specific ROI for the neurofeedback tasks.

To translate the BOLD signal within the ROI to a representation/position on the screen, the range of potential values needed to be determined. An additional problem is signal variation across persons, days and even scan runs [253,254]. For these reasons

neurofeedback related tasks were acquired in one single continuous run, starting with an initial count-back task that was used to determine the range of activation values, followed by the actual neurofeedback tasks. The neurofeedback tasks of 2.5 min each were interleaved with 30s periods of rest.

During the neurofeedback tasks functional images were retrieved straight from the scanner with the use of the Philips "Drin Data Dumper" tool. As soon as the software running on the task computer would detect a new task image it would be registered to the first image from the first scan run and smoothed (FWHM = 12 mm) in real-time. Subsequently, the BOLD signal of the voxels within the subject specific ROI were isolated and detrended, removing linear, quadratic and cubic trend from the time-series [255]. The mean was then taken and translated to the vertical position on the ladder using the upper and lower BOLD boundaries as reference for the top and bottom of the ladder.

Design

The first and last of the neurofeedback tasks served as pre- and post-test, while the five neurofeedback tasks in-between served as training. Both the experimental and control group received feedback on their DLPFC activity during the pre-and post-test. During training only the experimental group continued to receive feedback on their DLPFC activity, while the control group would receive sham-feedback, effectively only practicing counting backwards. The sham-feedback for each participant in the control group was taken from a different and at random selected experimental participant.

Each neurofeedback task resulted in a performance score (i.e. the number of apples picked). To test our hypothesis we used the scores on the neurofeedback tasks before and after training to test for differences within and between groups. Several characteristics of the BOLD signal were analyzed in order to examine the effect of practice on the ability to control DLPFC activity.

The first count-back task was – besides being used to determine the ROI for neurofeedback – also utilized to determine clusters of activation, the subsequent count-back tasks before and after neurofeedback were used to test examine the effect of neurofeedback on brain activity in the DLPFC and other brain regions.

Post-MRI analyses

The fMRI data from the count-back tasks was processed using SPM8 software. Analysis on DLPFC activity was performed in native space, the scans were corrected for motion and spatially smoothed with a Gaussian filter yielding a full-width at half-maximum (FWHM) of 12 mm in each direction. In order to investigate the effects on other brain regions, the motion-corrected scans were normalized to MNI space using DARTEL and also smoothed at 12 mm FWHM. Individual statistical activation maps were generated using a general linear model analysis. A single regressor was used to model activity for the count-back condition against baseline using a block design (20 s on, 20 s off). To identify other task-relevant brain regions

over subjects, a second level analysis was performed on the normalized beta estimation maps of the first count-back task. The resulting group map was thresholded at $p < .05$ (correcting for multiple comparisons using the false discovery rate method) to reveal a number of active clusters.

The behavioral effect of the training was determined using a one-tailed paired t-test ($\alpha = 0.05$), comparing the differences in pre and post-test apple pick scores within each group. To test for group differences we performed a mixed-design analysis of variance on the difference between the pre and post-test apple pick scores (one-tailed, $\alpha = 0.05$).

The influence of neurofeedback on brain activity in the DLPFC and other brain regions was tested using the regressor weights of the second and third count-back tasks, which were respectively before and after the neurofeedback. DLPFC effects were investigated in native space using the same ROI that was used for neurofeedback. The effect on other task-relevant brain regions was investigated in MNI space using the clusters defined by the first count-back task. To determine the direct effect of neurofeedback on the DLPFC we performed a two-tailed paired t-test ($\alpha = 0.05$) within each group and a mixed-design analysis of variance (two-tailed, $\alpha = 0.05$) to test between group differences. In order to investigate the interaction between the DLPFC and clusters we used a repeated measures ANOVA.

Performance and relation to feedback signal parameters

We calculated a number of parameters that describe the BOLD signal for each participant. These parameters reflect the activation velocity, the deactivation velocity, overshoot (over the upper boundary) and undershoot (under the lower boundary). Figure 2 (a) and (b) shows examples of such parameters. Every signal parameter was calculated separately for the pre- and post-test per participant. The signal elevation parameters were calculated by taking the BOLD signal's lowest point as the beginning of the trial, up till and including the first point above the upper boundary (top of the ladder) or the highest BOLD value after going above the upper boundary. Vice versa was done for the signal decline parameters. A mean was calculated over the elevating or declining segments and a linear slope was fitted. Another activation/deactivation parameter was generated by taking the average number of measurement points over the segments, and yet another parameter divides the signal change by the number of measurement points. The resulting slope parameters were regarded as the velocity of the decline or elevation.

To calculate the overshoot parameters we took the highest value, the AUC and the average of all points (i.e. scans) above the upper boundary (top of the ladder) of each trial and averaged these across trials. The same was done for the undershoot parameters but vice versa.
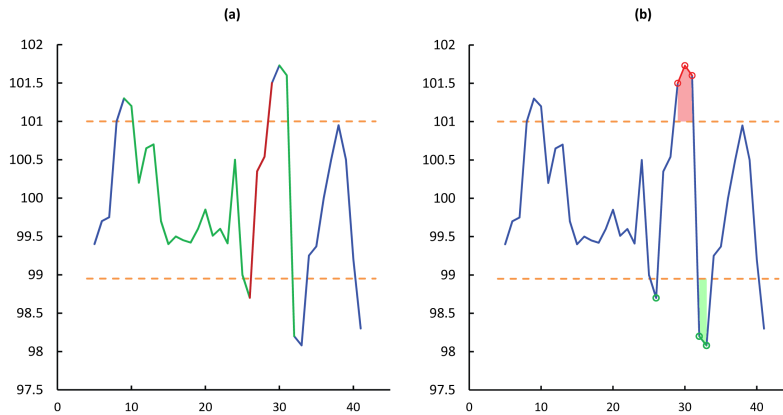
Figure 2. (a) Signal slopes, the signal is shown in blue, the upper and lower boundaries of the ladder in orange. The green indicates the part of the signal considered as decline, the red as elevation. (b) Signal over- and undershoots. The circles show measurement points which are used to calculate several over- or undershoot parameters. The red shaded area shows an example of an overshoot AUC, the green the undershoot.

For each parameter we deleted outliers (more than 3 interquartile ranges below the 1st quartile or above the 3rd quartile) pre–post pairwise. In some cases a parameter could not be calculated, for example when one of the runs held no successful apple pick trials or when no surface can be calculated from one overshoot point. In these cases, we also applied pre–post pair wise deletion for the missing parameter. Then, to validate each parameter we correlated the pre–post difference of the parameter to the pre–post difference in the task performance. Parameters that correlated highly to the apply pick performance were considered contributing factors and were used for further analysis. A two-tailed paired t -test (α = 0.05) was used on the pre and post-test signal parameters within each group and a mixed-design analysis of variance (two-tailed, α = 0.05) was used to test between group differences.

5.3 Results

Performance

The apple pick task performance within the experimental group improved significantly from 3.31 apples (SD: 1.44) before to 4.92 apples (SD: 2.49) after training (t(12) = −2.88, *p* = .007; see figure 3). In contrast, task performance within the control group did not change (t(10) = 0.00, *ns*) from an average of 4.00 apples (pre SD: 2.24, post SD: 2.49) picked. The difference in training effect between groups was significant (F (1, 22) = 3.38, *p* = .040).
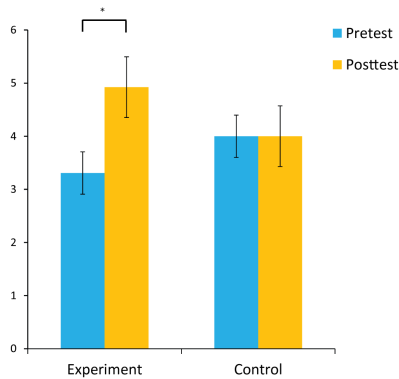
Figure 3. Neurofeedback behavioral results for the experiment (N = 14) and control (N = 11) group. The performance is measured in number of apples picked and shown for both the pre- and post-test run. (Bars denote the standard error; * significant at 0.05 level 1-tailed).

Brain activity

The DLPFC activity within the experimental group did not change after neurofeedback (pre vs post, t(12) = 1.669, *ns*), whereas the activity within the control group declined significantly (t(10) = 4.495, *p* = .001). However, this difference was not significant when comparing groups (F(1, 22) = 1.914, *ns*).
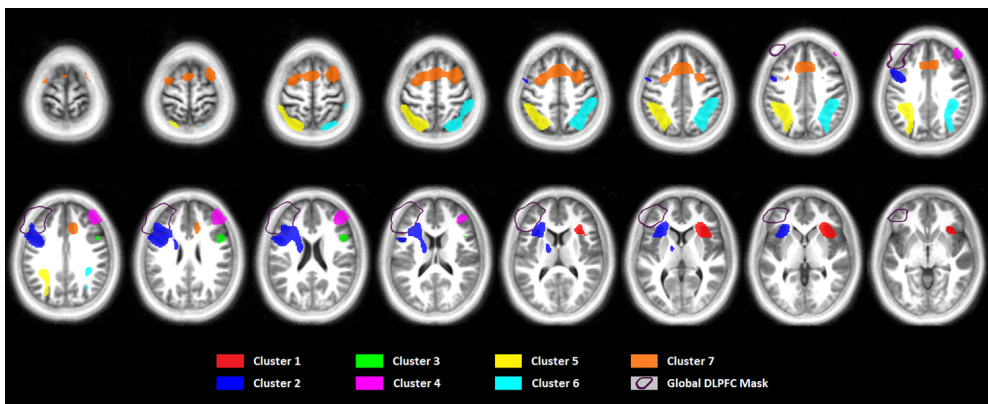
Figure 4. Group-activity (N = 24) in the first count-back task (neurological view, left = left). Clusters of activity with Bordmann area and number of voxels in MNI space at 1.5 mm isotropic: Cluster 1 – right inferior frontal gyrus (1629 voxels); Cluster 2 – left inferior frontal gyrus and hippocampal area (6789 voxels); Cluster 3 – right inferior frontal gyrus (417 voxels); Cluster 4 – right inferior frontal gyrus/Broca's (2101 voxels); Cluster 5 – left inferior parietal lobule (6590 voxels); Cluster 6 – right inferior parietal lobule (6609 voxels); Cluster 7 – anterior cingulate gyrus (8653 voxels).

A total of seven clusters were found in the first count-back task (see figure 4). A repeated measures ANOVA on ROIs (i.e. the DLPFC and clusters) before and after

neurofeedback comparing groups showed there is no 3-way interaction between the different ROIs, training and groups (F(4.13, 90.85) = 0.665, *ns*).

Parameter correlations

All four parameters describing the decline of the BOLD signal correlated with performance (p < .05, details in Table 2). Two of the signal elevation parameters –scans needed to pick apple and fitted slope till the highest point above the ladder – correlated with the task performance (r = 0.56, p = .015; r = 0.57, p = .022). Two of the under- and overshoot parameters – average value of undershoots and average value of overshoots – correlated with the apple pick performance (r = 0.42, p = .044; r = 0.47, p = .048).

Table 2. Correlations between feedback signal parameters and apple pick performance. Only parameters that correlate highly to the performance are considered valid contributors

Signal decline	
Slope of a linear fitted line based on trials mean (lowest point)	r = -.61, n = 20, **p = .004 ****
Mean number of scans until apple picked over trials	r = -.67, n = 21, **p = .001 ****
Slope based on the decrease (until below ladder) divided by the number of scans	r = -.69, n = 23, **p < .001 ****
Slope of a linear fitted line based on trials mean (first below ladder).	r = -.69, n = 18, **p = .001 ****
Signal elevation	
Slope of a linear fitted line based on trials mean (highest point)	r = -.20, n = 22, p = .364
Mean number of scans until apple picked over trials	r = -.56, n = 18, **p = .015 ***
Slope based on the decrease (until below ladder) divided by the number of scans	r = .29, n = 19, p = .226
Slope of a linear fitted line based on trials mean (first above ladder).	r = .57, n = 16, **p = .022 ***
Undershoot	
Average value of undershoots	r = .42, n = 23, **p = .044 ***
Average of deepest undershoots	r = .31, n = 24, p = .138
Average of undershoot area under curve	r = .02, n = 19, p = .941
Overshoot	
Average value of overshoots	r = .47, n = 18, **p = .048 ***
Average of highest overshoots	r = .28, n = 19, p = .252
Average of overshoot area under curve	r = .06, n = 16, p = .829

** Correlation is significant at the 0.01 level (2-tailed)
 * Correlation is significant at the 0.05 level (2-tailed)

Parameter tests

Tables 3 and 4 contain detailed statistics on all parameters that correlate to the performance. Three of the signal decline parameters –scans needed to pick apple, decrease divided by scans and the fitted slope till the first below ladder –show that the experimental group was able to decrease their BOLD signal significantly faster after practice (t(9) = 3.388, p = .008; t(11) = 2.861, p = 0.015; t(10) = 2.824, p = 0.018), while in the control group the same parameters showed no change (t (10) = −1.147, *ns*; t(10) = −1.106, *ns*; t(6) = −1.582, *ns*). The other signal decline parameter – fitted slope till the lowest point below ladder – showed no within-group effect in both the experimental group (t(11) = 2.099, *ns*) and control group

(t(7) = 0.708, *ns*). In the between-group analyses, three of the four signal decline parameters show a significant change in velocity for the experimental group when compared to the control group (F(1, 19) = 5.219, *p* = 0.034; F(1, 21) = 7.484, *p* = 0.012; F(1, 16) = 8.771, *p* = 0.009). These were the parameters based on the scans needed to pick apple, decrease divided by scans and the fitted slope till the first below ladder.

Table 3. Averages and standard deviations of the signal parameters which relate to apple pick performance

	Experimental group (N = 13)		Control group (N = 11)	
	Pre	Post	Pre	Post
Signal decline				
Slope of a linear fitted line based on trials mean(lowest point)	M: -0.54 SD: 0.25 N: 12	M: -0.74 SD: 0.33 N: 13	M: -0.45 SD: 0.20 N: 9	M: -0.52 SD: 0.13 N: 10
Mean number of scans until apple picked over trials	M: 9.93 SD: 1.98 N: 13	M: 6.54 SD: 2.25 N: 13	M: 8.75 SD: 4.23 N: 11	M: 11.49 SD: 6.48 N: 11
Slope based on the decrease (until below ladder) divided by the number of scans	M: -0.31 SD: 0.16 N: 13	M: -0.50 SD: 0.19 N: 13	M: -0.42 SD: 0.14 N: 11	M: -0.34 SD: 0.16 N: 11
Slope of a linear fitted line based on trials mean (first below ladder).	M: -0.03 SD: 0.03 N: 11	M: -0.22 SD: 0.22 N: 13	M: -0.20 SD: 0.14 N: 9	M: -0.10 SD: 0.10 N: 9
Signal elevation				
Mean number of scans until apple picked over trials	M: 11.27 SD: 5.26 N: 11	M: 7.93 SD: 3.78 N: 13	M: 5.81 SD: 2.83 N: 10	M: 6.57 SD: 3.01 N: 9
Slope of a linear fitted line based on trials mean (first above ladder).	M: 0.06 SD: 0.06 N: 10	M: 0.24 SD: 0.17 N: 13	M: 0.31 SD: 0.35 N: 8	M: 0.29 SD: 0.32 N: 8
Undershoot				
Average value of undershoots	M: 0.36 SD: 0.19 N: 13	M: 0.37 SD: 0.14 N: 13	M: 0.45 SD: 0.23 N: 11	M: 0.34 SD: 0.14 N: 11
Overshoot				
Average value of overshoots	M: 0.35 SD: 0.16 N: 11	M: 0.35 SD: 0.15 N: 13	M: 0.44 SD: 0.14 N: 10	M: 0.33 SD: 0.20 N: 9

Table 4. Test statistics on performance related feedback signal parameters. A paired t-test was used on the pre and post-test parameters within each group and a mixed-design analysis of variance was used to test between group differences

	Within group		Between
	Experimental	Control	group
Signal decline			
Slope of a linear fitted line based on trials mean (lowest point)	t(11) = 2.099, p =.060	t(7) = .708, p = .502	F(1,18) = .960, p = .340
Mean number of scans until apple picked over trials	t(9) = 3.388, p **=.008 **	t(10) = -1.147, p = .278	F(1,19) = 5.219, p **=.034 ***
Slope based on the decrease (until below ladder) divided by the number of scans	t(11) = 2.861, p **=.015 ***	t(10) = -1.106, p =.295	F(1,21) = 7.484, p **=.012 ***
Slope of a linear fitted line based on trials mean (first below ladder).	t(10) = 2.824, p **=.018 ***	t(6) = -1.582, p =.165	F(1,16) = 8.771, p **=.009 **
Signal elevation			
Mean number of scans until apple picked over trials	t(10) = 1.687, p = .122	t(6) = -.455, p = .665	F(1,16) = 2.100, p =.167
Slope of a linear fitted line based on trials mean (first above ladder).	t(9) = -2.925, p **=.017 ***	t(5) = .072, p =.945	F(1,14) = .890, p =.361
Undershoot			
Average value of undershoots	t(12) = -.295, p = .773	t(9) = 1.019, p = .335	F(1,21) = 1.321, p =.263
Overshoot			
Average value of overshoots	t(10) = .106, p = .918	t(6) = 2.249, p = .066	F(1,16) = 3.043, p =.100

** Significant at the 0.01 level (2-tailed)

* Significant at the 0.05 level (2-tailed)

Within-group analysis on the signal elevation parameters show that the fitted slope till the highest point above the ladder parameter changes significantly for the experimental group (t(9) = −2.925, p = 0.017) and not in the control group (t(5) = 0.072, p = 0.945). The elevation parameter – scans needed to pick apple – showed no significant changes in the experimental (t(10) = 1.687, *ns*) nor the control group (t(6) = −0.455; *ns*). Between group analysis of the elevation parameters show no difference of the experimental group in comparison to the control group (F(1,14) = 0.890, *ns*; F(1, 16) = 2.100, *ns*). See figure 5 (a) and (b).
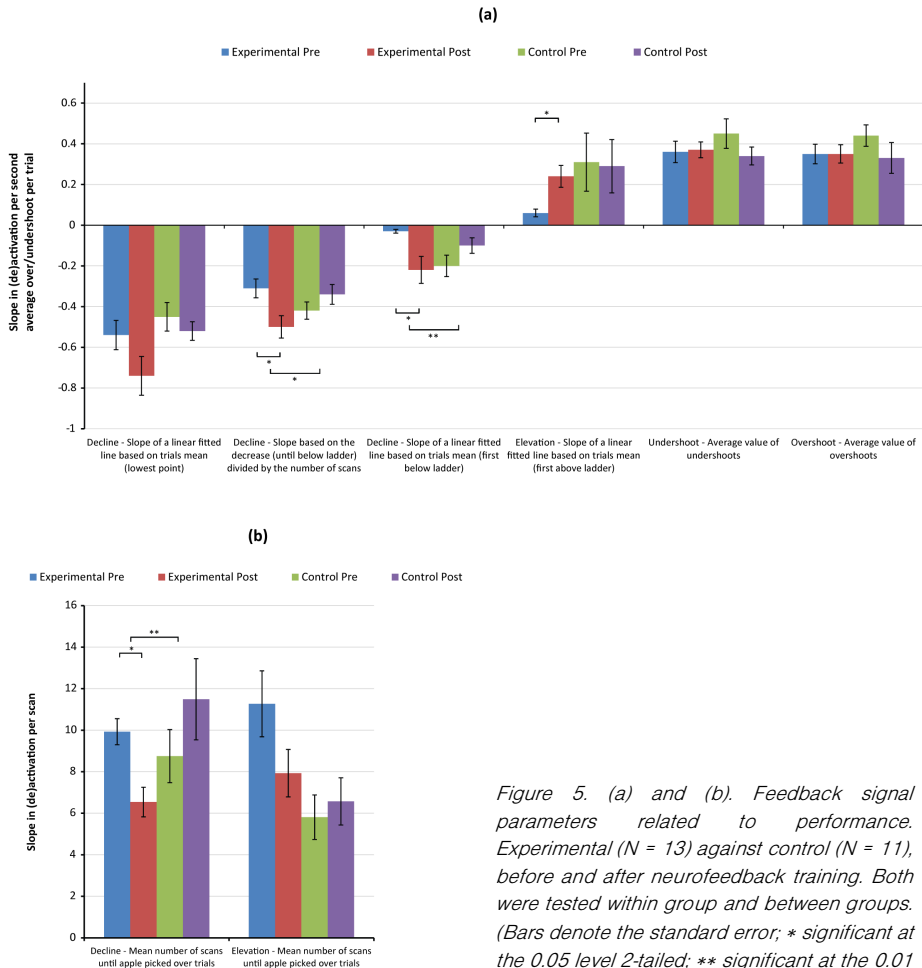
Figure 5. (a) and (b). Feedback signal parameters related to performance. Experimental (N = 13) against control (N = 11), before and after neurofeedback training. Both were tested within group and between groups. (Bars denote the standard error; ∗ significant at the 0.05 level 2-tailed; ∗∗ significant at the 0.01 level 2-tailed).

Both the undershoot parameter and the overshoot parameter showed no between-group effect ($F_{(1, 21)} = 1.321$, *ns*; $F_{(1, 16)} = 3.043$, *ns*) and no within-group effect in the experimental ($t_{(12)} = 0.295$, *ns*; $t_{(10)} = 0.106$, *ns*) nor the control group, ($t_{(9)} = 1.019$, *ns*; $t_{(6)} = 2.249$, *ns*).

5.4 Discussion

The goal of this fMRI study was to investigate whether people can learn to dynamically control activity of the DLPFC, a region that has been shown to be important for WM function [246–248], and has been associated with various psychiatric disorders. Results of this real-time neurofeedback study indicate that it is possible to acquire dynamic control of DLPFC after a 15-min training period. In-depth examination of the effect of training on the dynamic properties of the feedback signal showed a significant correlation between the speed of returning to baseline and neurofeedback performance. In particular, we observed a clear decline in the time needed to return DLPFC activity back to baseline levels, after training with neurofeedback. Although there are overshoot and undershoot parameters that correlate with the neurofeedback performance, they show no significant within- or between-group effect. From this, it can be concluded that improved performance was not simply the result of improved anticipation of the delay of the BOLD response. Other brain regions – including part of the left dorsolateral caudate nucleus and the lateral part of the left dorsomedial globus pallidus, both belonging to the dorsolateral prefrontal circuit – responded to the WM task, but were unaffected by neurofeedback on the DLPFC.

The elevation phase of the feedback signal in the experimental group did not show a significant change after practice compared to the control group. The absence of a practice effect on the elevation phase suggests that control over this phase is relatively difficult to improve with neurofeedback. This phase is mostly linked to the start and execution of the WM task, which immediately activates the left DLPFC and results in a maximum increase in the BOLD signal. As a result, there may not be much room for improvement in the speed of increasing activity. Another explanation could be the (relatively) low number of samples in the control group for the elevation parameters. Theoretically, a larger sample would result in more power and could show a significant effect in signal elevation. However, this scenario is unlikely as the means of the pre- and post-elevation parameter show little difference for the control group.

The training-induced reduction in the time to return to baseline suggests that it is possible to deliberately deactivate the DLPFC. Before training, DLPFC activity appears to linger on between the activity peak (top of the ladder) and dip (bottom of the ladder), which may be due to presence of context-irrelevant functions that cause the DLPFC to stay active. Through neurofeedback, subjects are able to discontinue such lingering and thereby reduce the time to return the DLPFC activity to baseline. In this context, it should be noted that DLPFC activity might not be the result of just manipulation and maintenance of information in WM, but could also be attributed to the selection of information [256] or an executive control network related to regulation itself [257,258]. This in turn raises the question how such a neurofeedback control mechanism would function: whether the DLPFC is (circularly) involved and learns to more efficiently switch off regulation (i.e. deactivate), or whether such a mechanism is more flexible and can function without DLPFC involvement to lower the activity faster. Regardless, it is conceivable that the neurofeedback enhances awareness of DLPFC activity and allows the trainee to acquire the skill to deactivate at will. This effect, we believe, warrants further

investigation into the potential benefits for therapeutic intervention where WM function is implicated.

Our results may provide several new insights. WM is characterized by a capacity constraint, imposing limitations for information processing [228,229]. Therefore, it is important that the WM capacity is used efficiently in order to optimize cognitive performance. Improved control over DLPFC may well constitute (a degree of) control over the WM system, thereby influencing WM function [250–252]. Improved control over WM, specifically an improved ability to return to rest after WM engagement, may result in better cognitive performance in situations where several tasks have to be performed, in terms of a more efficient allocation to the most pertinent task at hand. Improved control may also affect levels of stress during sustained cognitive demand. Several studies have indicated that cognitive effort elicits a stress response, including a reduced heart rate variability (HRV) [259–261]. A more rapid termination of activity in the WM system would facilitate (brief) rest states, thereby allowing for physiological energy replenishment [262], and possibly limiting mental fatigue.

In addition, although speculative, our results may have implications for treatment of brain disorders. In schizophrenia, for instance, WM function has been connected to cognitive deficits [230,232,263,264]. It has been shown that brain activity during WM tasks exhibits over-activation during low-demand WM tasks, whereas WM function and brain activity collapse at high demand, suggesting that schizophrenic patients suffer from inefficient use of WM function [230,263,265,266]. The notion that even brief feedback-training for dynamic control over DLPFC may improve efficiency of WM use, seems to warrant further investigation. Other brain disorders such as Huntington's disease and depression have also been associated with impaired WM [267–270] and the DLPFC, and could conceivably benefit from neurofeedback. For example, the left DLPFC is the target for a novel treatment of depression, involving repeated stimulation with transcranial magnetic stimulation [271].

The findings may also have implications for another emerging field, namely that of Brain Computer Interface (BCI) for people with severe communication disabilities (e.g. Locked-In Syndrome). Fora BCI, brain activity is detected and used to control external devices. Direct decoding from DLPFC activity has been shown to be feasible for this purpose [67], but it is unknown if DLPFC activity remains decodable after extensive use. Some WM studies have indicated that with practice of a WM task (no feedback), activity in the WM network can reduce substantially, even with very short periods of practice [100,101]. The repeated performance of a WM task to control a BCI could conceivably result in reduction of activity and consequently reduced BCI control. Our research shows that providing neurofeedback can in principle prevent this effect. A direct comparison with the controls, where DLPFC activity declined after sham feedback, was not significant, but it could be that the difference becomes more pronounced after longer training, given that WM activity is likely to continue to decline [101].

Multiple studies have shown that activity in a variety of brain areas can be influenced using neurofeedback and rt-fMRI [240–242,245,272–274], of which only a few studies addressed WM [250–252]. At least three studies [250–252] showed that it is possible to up-regulate activity in the left

DLPFC in a block-design neurofeedback task, and report an effect on subsequent WM function. One study [252] showed an improvement in verbal working memory, attributing it to the up-regulation of left DLPFC activation. On the same data, another study [251] showed changes in the functional connectivity due to the up-regulation of the left DLPFC as a new way to improve WM performance. Finally, a different study [250] showed improved performance on a custom-made WM task after neurofeedback training. In both studies the aim was to maximize self-induced velocity of DLPFC activation. The current study directly addresses the ability to control DLPFC activity dynamically, focusing on the ability to rapidly elevate and decline activity at will.

While we did show improved control over activity in left DLPFC after neurofeedback, we did not look for improvement in WM performance in our subjects. Given the results, investigation of the relationship between controllability (i.e. state shifts) and performance seems worthwhile. Since we allowed only for one session of training, we cannot draw conclusions about the duration of the training effect over time. Neither can we provide information about transferability to other tasks. However, results of previous neurofeedback studies targeting WM and using multiple sessions spread over multiple days indicate that improvement in WM control is indeed transferable over time and over WM tasks [250,252].

Our results show that it is feasible to accomplish dynamic control over DLPFC activity using neurofeedback. Detailed BOLD signal analyses indicated that training with neurofeedback predominantly resulted in improved ability to return DLPFC activity to a baseline level after activation. The finding that subjects learned to regulate DLPFC activity after a neurofeedback training period of only 15 min, suggests that this skill can be rapidly acquired with a real-time dynamic feedback task, and encourages investigation of potential therapeutic applications for patients with psychiatric and neurological disorders that have been associated with WM deficits.

5.5 Acknowledgments

Chapter 6

Summary and Discussion

6.1 Summary

Brain-computer interfaces (BCI) have the potential to improve and enhance our lives, enabling us to control devices with our thoughts and intentions. Currently, BCIs primarily aim to benefit a small patient population by, for example, providing an alternative communication channel for severely paralyzed people that are not able to speak, or enabling control over a prosthetic limb. While the current BCIs already deliver impressive results, the degree of control and the practical (daily) use is very limited. In terms of utilization of digitized brain activity, there is still much to explore and there are several challenges to overcome. This thesis aims to advance brain-computer interfacing by exploring the optimal utilization of brain activity in a diversity of brain functions and regions. Given the measurement techniques that are currently available, this thesis considers ECoG as the primary candidate for a daily home-use BCI while leveraging fMRI measurements to perform fundamental research that is transferable to ECoG-based BCI.

Most ECoG research on the decoding of finger movements or gestures is performed with patients who have a healthy moving hand [9,10,13,93,275]. However, BCIs are almost exclusively aimed at patients with paralysis or missing limbs. In **chapter 2,** we found that hand representations and their electrophysiological properties were retained in the sensorimotor cortex, even after long-term amputation of the contralateral arm. The physiological properties of attempted hand movement in this patient turned out to be almost identical to those of executed hand movement in people with a healthy hand, exhibiting a spatially focused increase of high-frequency band (HFB, 65–175 Hz) power over the hand region and a distributed decrease in low-frequency band (15–28 Hz) power. Representations of three different fingers (thumb, index and little) also proved to be distinguishable, with enough neural information present to differentiate the finger movements using machine learning algorithms at a classification accuracy of higher than 90%, based on the first 1–3 s of the HFB response. The distinguishability of finger representations, fast temporal onset and sustained decodability of attempted movements over time from just a small (13 x 13 mm) piece of the sensorimotor cortex, are encouraging for utilization in a BCI. These conclusions imply that despite potential deafferentation and plasticity of the brain, motor areas can continue to be used in a BCI over longer periods of time to drive neural prosthetic devices or communication devices.

In **chapter 3,** we have shown that the design (i.e. physical characteristics) and precise surgical placement of the electrode grid determine, to a large extent, how well neural information on hand movements is captured. Capturing the most relevant information, in turn, translates to the degree and reliability of control over a BCI. Using fMRI data-driven grid simulations, our study confirmed that most of the information encoding hand gestures resides in a densely packed area of the sensorimotor cortex. Although (additional) decodable

information is present outside of this informative area, any measuring capacity (i.e. electrodes in the case of ECoG) is best spent to measure from this relatively small informative area. Given the limited size (~22mm x ~22mm) of the relevant cortical area, there is a spatial trade-off between the number of electrodes, the spacing in-between electrodes, and the size of the electrodes. Having larger electrodes (up to 3mm in radius) improved decoding in fMRI models, which is likely the result of an increase in the signal-to-noise ratio (SNR) caused by averaging over more voxels per simulated electrode. A similar electrode size to SNR relationship likely applies to ECoG recordings [89,190]. In accordance with the widespread assumption that higher resolution sampling will provide more information, our simulations showed that a higher number (up to 5 x 5 electrodes) of densely-packed electrodes provides a more informative resolution for decoding hand gestures in general. However, very similar results can be achieved with fewer electrodes (e.g. 3 x 3) and an optimal inter-electrode distance (e.g. 8mm), which is more practical in terms of battery life, cost of implantable amplifiers, real-time processing and clinical invasiveness. Our simulations of electrode grid placements also show that the grid configuration and exact placement on the cortex can be more important than having more electrode sites. These results strongly argue in favor of fMRI data-driven simulations (such as described in the study) to be used pre-operatively to ensure the most optimal control over an implanted BCI.

In the context of a communication BCI for locked-in patients, some researchers suggest decoding hand gestures (from sign language) to spell letters, words, and sentences. Instead of using hand gestures, **Chapter 4** proposes visual imagery. We demonstrate that visually imagined characters (i.e. seeing a letter in the mind's eye) can be decoded from the early (V1, V2, V3) visual cortex with minimum training, providing an intuitive way of per-letter spelling in a BCI. We showed that prolonged visual imagery (of 3, 5 and 7 seconds) does not result in better classification over time, implying that. allowing more time to visually imagine does not contribute to the quality of the information present in early visual areas. However, prolonged imagery did extend decodability over time, suggesting sustained neuronal activity that can be utilized for BCI purposes. While the research here aims specifically at decoding discrete characters and understanding the temporal properties of imagery, these kinds of endeavors do not need to be limited to just characters. Decoding more complex shapes with advanced decoding models might provide a way for patients to convey information more efficiently.

Activity in the dorsolateral prefrontal cortex (DLPFC) can be voluntary controlled and provide input to a BCI when motor representations are impaired. In **chapter 5,** we showed that people can learn to dynamically control the activity in the left DLPFC, a working memory region, within a short period of time when provided with closed-loop neurofeedback. The neurofeedback predominantly improved the ability to return the activity in the DLPFC to baseline after peak activation. Speculatively, being able to control DLPFC activity might benefit patients with psychiatric or neurological disorders that are related to working memory deficits. In the context of BCIs, voluntary controlled DLPFC activity could be used directly as an input signal. However, a potential practice effect (i.e. automatization of the task) and the

associated decrease of activity in the WM network [100,101] might result in reduced control over a BCI. Our results suggest that by providing closed-loop feedback, we may be able to negate a practice effect over time and preserve the reliability of the DLPFC input signal.

6.2 Discussion

The BCI field has the collective goal to improve and enhance people's daily lives. The research in this thesis contributes towards this goal by investigating and optimizing BCI approaches.

We have shown that electrophysiological properties of hand representations in the sensorimotor cortex remain intact after long-term amputation of the contralateral arm, supporting the idea that conclusions from fundamental research in healthy participants are transferable to specific patient populations and vice versa. We investigated how to optimally extract hand gesture information from the brain and how (invasive) BCI performance can be improved by matching the grid design to the resolution of information within the cortex and more informed grid placement. We demonstrate the feasibility of using visual imagery, taking into account the temporal properties, to provide an intuitive way to control a BCI with an absolute minimum of prior training on behalf of the user. We show that DLPFC activity can be voluntarily controlled by providing closed-loop feedback and how feedback – at least in the DLPFC – negates a practice effect.

Although each of the studies in this thesis focuses on a specific brain function and area, I believe some of the insights can be generalized and applied in a broader sense. I will attempt to put the studies in this thesis into the context of the current developments in the field of BCI given the possibilities and challenges: I focus on the optimization of measurements, the feasibility and integration of brain functions, and finally elaborate on how BCI applications should be controlled.

6.3 Measurement optimization

Obtaining optimal information with (custom shaped) data-fitted electrode grids

As illustrated in chapters 2 and 3, only a small piece of the hand sensorimotor cortex is required to provide sufficient information for a BCI when sampled at an optimal resolution by a limited number of well-placed electrodes. In terms of coverage, the same applies to decoding of (motor) speech [51,89], facial expressions [183] and visual perception [276,277], and might be generalized to other primary systems. Considering the scale and resolution at which we want to extract information (e.g. separate fingers or wrist rotations, the visual field-of-view, articulator movements), the field of BCI is still in need of hardware that optimally matches neuronal representations. Large clinical ECoG grids with a typical electrode spacing of 1 cm center-to-center might not offer the optimal resolution to pick up the detailed information we need in a BCI application (as shown in chapter 3). On the other hand, intracortical MEAs

might have too high of a resolution for BCI purposes, retrieving information that could just as easily be obtained by measuring from small populations of neurons without precipitous loss of unit activity, heavy temporal resolution data processing and the need for regular recalibration due to electrode-tissue shifts. To solve the issues of intracortical MEAs and sparse sampling with clinical ECoG, the mesoscopic scale of high-density ECoG grids (with a typical spacing of 3 to 4 mm) might provide the required resolution, and are already being used in research where they are placed temporarily alongside clinical electrode grids.

In terms of the electrode grid shape, grids might be produced to fit the relevant region, fit the optimal resolution of information and can be irregular in layout. For instance, grid electrodes do not have to be laid out in equally spaced arrays or with the same electrode size, but could have electrodes in irregular patterns that match the relevant spatial properties of the information in the brain. Preferably, the design of such (custom) grids is driven by pre-operative fMRI measurements and simulations to optimally match the neuronal representation of the brain function that is to be decoded. In addition, distances between the electrodes could be optimized to take advantage of the temporal-spatial dynamics, in the same way that adding the temporal component increases hand decodability [14].

Acquisition of sulcal information

fMRI is able to measure below the outer superficial cortex and can therefore include information from the cortical sulci. ECoG is limited in that capability and mainly measures the electrical potential from the gyri of the brain. Although the brain's outer exposed surface already provides enough information for high decoding performances, there can be equally valuable information within the sulci, for example, on hand movements [13,134,163]. SEEG electrodes could be used to measure from those places where ECoG cannot. In the clinical setting, SEEG is used increasingly for the localization of epilepsy sources [278–280]. Like ECoG, SEEG also captures field potentials and – if placed strategically – can be used for control [281,282] or decoding [283]. Although the sparse, spatially in-line, sampling along each SEEG lead might pose some limitations for the purpose of BCI (i.e. a small ECoG grid on the surface might be more informative than having multiple depth electrodes covering a small sensorimotor area), there could be a benefit in combining surface and depth measurements to sample from both the gyri and sulci, possibly using a single (custom) implant. I propose that the placement of these types of BCI implants should be guided by fMRI imaging.

Future

Most of these technological optimizations depend on a small number of companies that are technologically capable to manufacture such custom electrode designs, certify them for in-human use, and are willing to serve a currently very small market. Luckily, some initiatives have recently emerged that might move the field forward and might push others to follow. As of yet, given the current technology, ECoG remains one of the best candidates when aiming

for a practical BCI to be used daily by patients or perhaps — in the future — even by healthy people.

6.4 Feasibility of brain function and the integration of multiple functions

Research and BCI development will continue to progress for several brain functions, such as hand or arm motor representations, visual imagery, or working memory. When considering the feasibility of brain functions and areas for a BCI, it is important to not only consider the capabilities of a brain function for a BCI at this moment in time (i.e. the current stage of research, which is often less than envisioned) but also to take into account the future potential (how a function is envisioned to be used). Some brain functions can be utilized more easily and are being utilized for BCIs at home or in a lab setting, while other brain functions can only be employed theoretically and require additional research, but carry great promise with them. In this paragraph, I will first consider the feasibility of each brain function for a BCI separately, followed by a perspective on the integration of multiple functions.

Hand/arm motor representations

As mentioned, the motor areas that drive hand and arm movement have a relatively large topographical representation on the cortex, which can be utilized with a variety of measurement techniques. For this reason, utilizing hand or arm-related activity from the sensorimotor cortex has been a popular and relatively far developed line of research.

Utilization of hand or arm movements to control a prosthetic hand or arm is feasible with a BCI. Finger movements can be decoded in patients with an amputated arm (see chapter 2; [145,284]), in a similar way as in healthy people [10,13]. In addition, research has shown that finger flexion can be decoded on a continuous scale in people with an intact hand [10,74,75,285], suggesting that gradual finger control is possible. In terms of equipment, compact and advanced prosthetic hands have already been developed and are being used. For upper arm amputees, the kinetics of the wrist and arm joints might still provide a challenge for reaching a target in 3D space. Much of the arm research aims to reach a 2D or 3D target using bulky robotic arms or exoskeletons, which can only be used in a laboratory setting. Implementation of this research for clinical purposes would have a high yield. A potential BCI driven by hand or arm motor activity would not only serve a small number of locked-in patients (est. prevalence of .73 per 100.000 in the Netherlands [286]) but could also benefit a much larger target population with limb amputation [287–289]. However, currently a myoelectric-controlled prosthesis (i.e. a prosthesis driven by muscles in the residual limb) might be more practical and appealing than one controlled by brain signals.

Utilizing hand or arm movements for a communication BCI might be less straightforward but still provides interesting opportunities. Hand or arm movement could be employed to control a cursor, but would in turn need to operate some form of a virtual letter, word or sentence board. Spelling by decoding sign-language hand gestures could provide a

fast and reliable alternative that better fits the purpose of communication. However, before such a communication BCI could be realized, more detailed decoding of finger movements is required, and the number of gestures would have to be scaled up.

An alleged threat to the utilization of attempted hand or arm movement could lie in the deafferentation and plasticity of the brain, causing the usability of the signal in the sensorimotor cortex to degrade. However, as shown in Chapter 2, the physiological properties of the hand remain intact for utilization over time in amputees. And a similar conclusion could be reached for the locked-in population that already uses hand movement to control a BCI [1,42,45].

Visual

The utilization of the visual system is relatively underexplored for the purpose of a BCI, especially given the extensive knowledge about this system. The activity in early visual areas (V1, V2, V3) could be used to control a BCI by a range of measurable visual properties in a very intuitive way. For instance, in paralyzed people, by decoding imagined characters (chapter 4), or attention [243,290] on virtual letter grids. Promising research on the decoding of visual perception from brain activity [76–81], the neural overlap in visual imagery and perception [199,201,215,225], and generative imagery decoding models based on in-silico training [277] or prior perceived stimuli [225] implies that some degree of decoding imagined scenes or objects from "the mind's eye" is not far off. When realized, this could provide a very efficient way to communicate information and is highly complementary to what can be decoded from the motor system.

While early visual areas show promise in the decoding of visual imagery, there are two practical issues. First, interfacing with the primary and secondary areas that underlie the visual system using invasive measurement techniques is difficult because of poor accessibility to these occipital regions. Part of the early visual cortex cannot be reached from the brain surface (i.e. located in the calcarine fissure) or is obstructed by large cerebral veins (e.g. superior sagittal sinus and internal occipital vein). Second, changes in the visual perception (i.e. the input to the retina) will result in stronger neuronal activity in the early visual regions than imagery and will "interfere" with the — much weaker — neuronal activity generated with visual imagery. Visual imagery would have to be performed while gazing at a plain surface or having the eyes closed. Feedback on typing can be auditory or be provided outside of a spelling time window in the visual periphery. While the interference of visual perception might be an issue, the difference in neuronal activation and signal strength between visual imagery and perception could, in fact, be exploited in a BCI to detect whether the patient intends to spell or is just looking around.

A different approach could decode visually imagined concepts or categories, like faces or houses, from higher-order visual areas (e.g. fusiform face area, lateral occipital cortex or the intraparietal sulcus). High-order visual areas have more frequent clinical coverage than early visual areas and can provide good decodability [208,291–296]. However, given

the abstraction of the representations and the large number of categories needed to provide communication, higher-order areas alone might not be suited for a communication BCI.

Dorsolateral prefrontal cortex

The DLPFC, one of the working memory areas, can be used directly as a voluntarily controlled input signal for a BCI. The closed-loop feedback that a BCI provides should negate a practice effect and allow a user to rapidly acquire dynamic control over DLPFC activity (Chapter 5). A DLPFC-based BCI can be a solution for when motor function is impaired [96–99] or when a mentally less fatiguing alternative to sensorimotor imagery is desired [68]. However, there is a good chance that performing another task (like remembering what to say or spelling a sentence in a communication BCI) would also evoke DLPFC activity and interfere with, or cause unwanted, BCI control. While such interference might make direct control of a BCI with the DLPFC impractical, DLPFC activity can still be invaluable when combined with other brain functions, as discussed later on.

Mouth motor representations

The research in this thesis on hand motor representations may also apply to mouth motor representations. Neural representations of mouth movements are preserved over time when people lose the ability to speak due to stroke [84] and it is believed that decoding articulator movements could restore speech in a communication BCI [54]. As such, an fMRI-based design of electrodes (Chapter 2) for decoding imagined speech may be equally valuable. Mouth motor representations could, in the same way as the hand motor, visual and working memory functions, be complementary to, and integrated with, other functions in a BCI.

Integrating multiple brain functions

While it is intuitive and tempting to tie one specific brain function to one specific purpose, it may be important to explore and integrate multiple brain functions. Motor representations of the hand or arm are relatively easy to utilize and could already in the near future provide a functional BCI, but the addition of other functions can prove beneficial.

One reason to combine brain functions is to enhance control to make it faster and more reliable. For instance, an object in 3D space might be targeted better with a robotic arm when sensorimotor-control is combined with visual attention information from the early visual cortex. In the same way as the visual dorsal stream likely provides such a mechanism for object location and motor control [297,298].

Another reason to combine brain functions is to offer multimodal control, to create a BCI that is not driven just by a single function. As with a car, you don't just want to be able to steer it in a particular direction, but also would like to have a gas pedal, a brake and the possibility to turn the car off. In the same way, when controlling a cursor on the screen, you also want to "click" or perhaps switch the control to something other than the cursor. When

considering the research in this thesis, the DLPFC activity in particular could be integrated with another brain function to detect the intention to use a BCI or prevent false positives. For example, the DLPFC could be used to detect whether a BCI user is passive or asleep [299,300] or whether a user is focusing on BCI control and should respond to the input of another brain function. Furthermore, it has been shown that an error-potential in the DLPFC can be used to detect unintended false positives in a hand motor-driven cursor control task [69], which could be translated to detection of misspelled letters in a communication BCI. A more extensive BCI could also allow for different functions to control several devices depending on the context. To speculate on future technology, people equipped with a BCI could choose to talk using speech motor representations, control a robotic arm with hand motor representations, control a wheelchair with leg representations, convey graphical concepts with visual imagery, and switch back to finger movement to control the cursor on their web-browser.

Given the variety of ways in which brain functions and regions could be integrated, and the relatively limited brain coverage and opportunity to measure in ECoG, fMRI could play a vital role in investigating such integrations prior to their implementation using ECoG. In order to achieve the integration of multiple brain functions, I think it is necessary to have multiple (fMRI optimized) implants, similar to the Utrecht NeuroProsthesis [1] with grids placed on both the sensorimotor cortex and the DLPFC.

6.5 Control and prior knowledge of BCI applications

Balancing freedom, reliability, speed and the use case

We can consider several types of BCI control. Translating brain input or features directly to one continuous dimension (like in Chapter 5) gives a BCI user a tremendous amount of control, where the degree of control and freedom can be increased significantly by simply having more dimensions. Two-dimensional continuous control is already enough to resemble how we use a mouse cursor on a screen, whereas three dimensions would resemble how we move our hand in space. In comparison, the type of BCI control that translates activity into a binary value (i.e. brain-clicks) or that classifies specific activity features into discrete classes might seem restrictive and limited in its possibilities. However, when we take into account the reliability of control and the use-case (i.e. the goal of a specific BCI), then a BCI that works with or includes brain-clicks or discrete brain states can turn out to be advantageous.

Despite the reasonable reliability of continuous control (e.g. 53-73% on two dimensions [170]), it is not as reliable as what we expect in real life when, for example, we are moving our cursor to click a link on a webpage, typing on a keyboard or trying to pick up a coffee cup. In use-cases where a paralyzed person is trying to communicate or wants to control a robotic arm, it can be frustrating if a BCI keeps misclicking, mistyping, or knocks over a drink. In time, advancements in the measurement techniques (see Chapter 6.3), optimal sampling of relevant information (see Chapter 3) and signal processing will allow for continuous multi-dimensional control to become increasingly reliable. But until continuous

control reaches a degree close to perfect, brain-clicks or classification of discrete brain states could provide a more reliable solution. Precisely because the degrees of freedom for control are small and the output options are limited, the chance of error in the output decreases and higher reliability can be achieved. In addition, having limited options can benefit the speed of BCI output, especially in use-cases where the output priority lies in a small number of frequently required options rather than more freedom of control.

Another reason to take different types of control into account is the use-case and specific (sub)goals of a BCI. Like in the example of the car in the 'integrating multiple brain functions' paragraph (in 6.4), two-dimensional control without a straightforward ability to click or select, or without the ability ever to switch the BCI off, might not be practical.

An example is the Utrecht NeuroProsthesis (UNP) [1], which currently provides BCI control to several locked-in patients using a permanent ECoG brain implant over the sensorimotor cortex. I was involved in this project since the first patient was implanted and have adjusted the working of this BCI to fit the patient's needs over a period of at least four years. The UNP provides the patient with an alarm function to call a caretaker (i.e. a nurse or relative) by keeping brain activity above a threshold (i.e. the brain-click "on") for a longer period of time. To at least one of the patients, this simple control functionality was very reliable, highly valued and comforting. Only secondary comes the (less reliable and more slow) ability to spell sentences by picking letters from a virtual letter grid. To illustrate, when the patient is asleep, only the alarm function is available. Only after the alarm is noticed by a caretaker, can the program be switched to spelling. While this example does not entail different control types, it does illustrate the importance of mode switching, reliability and speed at the expense of control freedom in a real-life use case.

In conclusion, at this point of BCI development, the type of control involves a balance between the degrees of freedom, reliability, speed, and use-case. While it is difficult enough to obtain reliable control over one feature, an approach where different types of BCI control and multiple brain functions are combined in a practical manner to satisfy the goals in a use-case should still be considered.

A-priori knowledge, training and neurofeedback

Most BCIs possess a certain degree of prior knowledge — in the broadest sense — to function. Already, different output types and their reliability and speed are related to different degrees of prior knowledge; for example a classifier requires knowledge of activity patterns before it can function. BCIs can be given additional prior knowledge to become even more reliable and fast at the expense of degrees of freedom that are not required. In a communication BCI, the knowledge of grammar constructions and the Bayesian probability of the following letter or the next word can be added (e.g. a vocabulary language model [40]). During movement, the kinetic restrictions of the arm and hand [301] or constraints in finger flexion [74] can be used. And in decoding visual cortical activity, prior information from encoding models [76,77,80] or theories of visual processing [277] can be applied. Over recent years, BCI decoding models became more complex by prior training on big datasets, largely driven by developments in

artificial neural networks. Ironically, these neural networks often are black-boxes in which processing layers contain such abstract pieces of information that — for humans — it is difficult to follow and match with fundamental processes in the brain. Regardless, neural network models might improve decoding performances [15,302–305] and perhaps similar models could be generated based on large amounts of fMRI data and applied in an ECoG-BCI application.

Finally, in the same way as (decoding) models can improve with considerable amounts of data, the quality of the data should be taken into account. In fMRI, head movements have a negative impact on the decodability of visual imagery (as shown in Chapter 4), and the classification accuracy of hand gestures from brain activity correlates significantly with the consistency of gesture execution [92]. In terms of consistency, a user might practice the execution of gestures beforehand to reinforce more similar neural representations, resulting in more reliable BCI control. Closed-loop feedback might have a similar effect in a more natural way because it provides the user with constant feedback on the "quality" or "correctness" of their neural representation. Therefore, it should be possible to learn and improve that representation and gain more reliable control. While we provided such feedback on a continuous dimension for DLPFC in Chapter 5, feedback can also be provided on categorical representations. Although I spent a lot of time and effort trying to achieve neurofeedback on visual imagery to reinforce more consistent neural representations during my PhD, these efforts did not become part of this thesis. The problem I encountered was that to investigate a positive effect of categorical neurofeedback, there has to be a very reliable classification model underlying the feedback; otherwise, the "wrong" neural representations on inaccurate classifications might get reinforced as well. For visual imagery, a reliable enough classification model proved too difficult at the time. Still, I believe this direction is worth pursuing, particularly because there is less activity during visual [277] and motor imagery [6,165,306] compared to actual perception and execution of movement, which leaves much opportunity for improvement. By bolstering neural representations of imagery either in amplitude or consistency, it is possible to take another next step towards more reliable, multifunctional BCI control.

6.6 Conclusion

In this thesis ECoG and fMRI were used to investigate the neural properties of sensorimotor, visual and working memory functions for utilization in a BCI. Each of these individual functions could provide control over a BCI, however, integration of multiple functions in the future is likely to offer a more complete, controllable and stable BCI. In addition, I recommend the use of electrode grids tailored specifically to optimally sample the most relevant information from the cortex, ideally driven by fMRI measurements. Given the current state of the field, ongoing research and pending initiatives, I see a bright future for brain-computer interfacing.

7. Bibliography

1. Vansteensel, M. J. *et al.* Fully Implanted Brain–Computer Interface in a Locked-In Patient with ALS. *New England Journal of Medicine* **375**, 2060–2066 (2016).

2. Pels, E. G. M. *et al.* Stability of a chronic implanted brain-computer interface in late-stage amyotrophic lateral sclerosis. *Clinical Neurophysiology* **130**, 1798–1803 (2019).

3. Crone, N. E. *et al.* Functional mapping of human sensorimotor cortex with electrocorticographic spectral analysis: I. Alpha and beta event-related desynchronization. *Brain* **121**, 2271–2299 (1998).

4. Crone, N. E., Miglioretti, D. L., Gordon, B. & Lesser, R. P. Functional mapping of human sensorimotor cortex with electrocorticographic spectral analysis: II. Event-related synchronization in the gamma band. *Brain* **121**, 2301–2315 (1998).

5. Miller, K. J. *et al.* Spectral changes in cortical surface potentials during motor movement. *Journal of Neuroscience* **27**, 2424–2432 (2007).

6. Miller, K. J. *et al.* Cortical activity during motor execution, motor imagery, and imagery-based online feedback. *Proceedings of the National Academy of Sciences of the United States of America* **107**, 4430–4435 (2010).

7. Manning, J. R., Jacobs, J., Fried, I. & Kahana, M. J. Broadband shifts in local field potential power spectra are correlated with single-neuron spiking in humans. *Journal of Neuroscience* **29**, 13613–13620 (2009).

8. Shenoy, P., Miller, K. J., Ojemann, J. G. & Rao, R. P. N. Finger movement classification for an electrocorticographic BCI. in *Proceedings of the 3rd International IEEE EMBS Conference on Neural Engineering* 192–195 (2007). doi:10.1109/CNE.2007.369644.

9. Miller, K. J., Zanos, S., Fetz, E. E., Den Nijs, M. & Ojemann, J. G. Decoupling the cortical power spectrum reveals real-time representation of individual finger movements in humans. *Journal of Neuroscience* **29**, 3132–3137 (2009).

10. Kubánek, J., Miller, K. J., Ojemann, J. G., Wolpaw, J. R. & Schalk, G. Decoding flexion of individual fingers using electrocorticographic signals in humans. *Journal of Neural Engineering* **6**, 066001 (2009).

11. Chestek, C. A. *et al.* Hand posture classification using electrocorticography signals in the gamma band over human sensorimotor brain areas. *Journal of Neural Engineering* **10**, 26002–26013 (2013).

12. Blakely, T. M., Olson, J. D., Miller, K. J., Rao, R. P. N. & Ojemann, J. G. Neural correlates of learning in an electrocorticographic motor-imagery brain-computer interface. *Brain-Computer Interfaces* **1**, 147–157 (2014).

13. Siero, J. C. W. *et al.* BOLD matches neuronal activity at the mm scale: A combined 7T fMRI and ECoG study in human sensorimotor cortex. *NeuroImage* **101**, 177–184 (2014).

14. Branco, M. P. *et al.* Decoding hand gestures from primary somatosensory cortex using high-density ECoG. *NeuroImage* **147**, 130–142 (2017).

15. Volkova, K., Lebedev, M. A., Kaplan, A. & Ossadtchi, A. Decoding Movement From Electrocorticographic Activity: A Review. *Frontiers in Neuroinformatics* vol. 13 74 (2019).

16. Rosen, B. R. & Savoy, R. L. FMRI at 20: Has it changed the world? *NeuroImage* vol. 62 1316–1324 (2012).

17. Uludağ, K., Müller-Bierl, B. & Uğurbil, K. An integrative model for neuronal activity-induced signal changes for gradient and spin echo functional imaging. *NeuroImage* **48**, 150–165 (2009).

18. Buxton, R. B. Interpreting oxygenation-based neuroimaging signals: the importance and the challenge of understanding brain oxygen metabolism. *Frontiers in Neuroenergetics* **2**, 8 (2010).

19. Logothetis, N. K., Pauls, J., Augath, M., Trinath, T. & Oeltermann, A. Neurophysiological investigation of the basis of the fMRI signal. *Nature* **412**, 150–157 (2001).

20. Mukamel, R. *et al.* Neuroscience: Coupling between neuronal firing, field potentials, and fMRI in human auditory cortex. *Science* **309**, 951–954 (2005).

21. Conner, C. R., Ellmore, T. M., Pieters, T. A., di Sano, M. A. & Tandon, N. Variability of the relationship between electrophysiology and BOLD-fMRI across cortical regions in humans. *Journal of Neuroscience* **31**, 12855–12865 (2011).

22. Hermes, D. *et al.* Neurophysiologic correlates of fMRI in human motor cortex. *Human Brain Mapping* **33**, 1689–1699 (2012).

23. Hermes, D. *et al.* Cortical theta wanes for language. *NeuroImage* **85**, 738–748 (2014).

24. Vansteensel, M. J. *et al.* Spatiotemporal characteristics of electrocortical brain activity during mental calculation. *Human Brain Mapping* **35**, 5903–5920 (2014).

25. Siero, J. C. *et al.* BOLD consistently matches electrophysiology in human sensorimotor cortex at increasing movement rates: A combined 7T fMRI and ECoG study on neurovascular coupling. *Journal of Cerebral Blood Flow and Metabolism* **33**, 1448–1456 (2013).

26. Winawer, J. *et al.* Asynchronous broadband signals are the principal source of the bold response in human visual cortex. *Current Biology* **23**, 1145–1153 (2013).

27. Jacques, C. *et al.* Corresponding ECoG and fMRI category-selective signals in human ventral temporal cortex. *Neuropsychologia* **83**, 14–28 (2016).

28. Hermes, D., Nguyen, M. & Winawer, J. Neuronal synchrony and the relation between the blood-oxygen-level dependent response and the local field potential. *PLoS Biology* **15**, e2001461 (2017).

29. Collinger, J. L. *et al.* High-performance neuroprosthetic control by an individual with tetraplegia. *The Lancet* **381**, 557–564 (2013).

30. Bouton, C. E. *et al.* Restoring cortical control of functional movement in a human with quadriplegia. *Nature* **533**, 247–250 (2016).

31. Benabid, A. L. *et al.* An exoskeleton controlled by an epidural wireless brain–machine interface in a tetraplegic patient: a proof-of-concept demonstration. *The Lancet Neurology* **18**, 1112–1122 (2019).

32. Sellers, E. W. & Donchin, E. A P300-based brain–computer interface: Initial tests by ALS patients. *Clinical Neurophysiology* **117**, 538–548 (2006).

33. Parker, R. A., Davis, T. S., House, P. A., Normann, R. A. & Greger, B. The functional consequences of chronic, physiologically effective intracortical microstimulation. in *Progress in Brain Research* vol. 194 145–165 (Elsevier, 2011).

34. Prasad, A. & Sanchez, J. C. Quantifying long-term microelectrode array functionality using chronic in vivo impedance testing. *Journal of Neural Engineering* **9**, 026028 (2012).

35. Chestek, C. A. *et al.* Long-term stability of neural prosthetic control signals from silicon cortical arrays in rhesus macaque motor cortex. *Journal of Neural Engineering* **8**, 045005 (2011).

36. Linderman, M. D. *et al.* Neural recording stability of chronic electrode arrays in freely behaving primates. in *Annual International Conference of the IEEE Engineering in Medicine and Biology - Proceedings* 4387–4391 (2006). doi:10.1109/IEMBS.2006.260814.

37. Santhanam, G. *et al.* HermesB: A continuous neural recording system for freely behaving primates. *IEEE Transactions on Biomedical Engineering* **54**, 2037–2050 (2007).

38. Perge, J. A. *et al.* Intra-day signal instabilities affect decoding performance in an intracortical neural interface system. *Journal of Neural Engineering* **10**, 036004 (2013).

39. Jorfi, M., Skousen, J. L., Weder, C. & Capadona, J. R. Progress towards biocompatible intracortical microelectrodes for neural interfacing applications. *Journal of Neural Engineering* vol. 12 011001 (2015).

40. Willett, F. R., Avansino, D. T., Hochberg, L. R., Henderson, J. M. & Shenoy, K. v. High-performance brain-to-text communication via handwriting. *Nature* **593**, 249–254 (2021).

41. Jarosiewicz, B. *et al.* Virtual typing by people with tetraplegia using a self-calibrating intracortical brain-computer interface. *Science Translational Medicine* **7**, 14 (2015).

42. Pandarinath, C. *et al.* High performance communication by people with paralysis using an intracortical brain-computer interface. *eLife* **6**, (2017).

43. Ajiboye, A. B. *et al.* Restoration of reaching and grasping movements through brain-controlled muscle stimulation in a person with tetraplegia: a proof-of-concept demonstration. *The Lancet* **389**, 1821–1830 (2017).

44. Kim, S. P., Simeral, J. D., Hochberg, L. R., Donoghue, J. P. & Black, M. J. Neural control of computer cursor velocity by decoding motor cortical spiking activity in humans with tetraplegia. *Journal of Neural Engineering* **5**, 455–476 (2008).

45. Bacher, D. *et al.* Neural point-and-click communication by a person with incomplete locked-in syndrome. *Neurorehabilitation and Neural Repair* **29**, 462–471 (2015).

46. Aflalo, T. *et al.* Decoding motor imagery from the posterior parietal cortex of a tetraplegic human. *Science* **348**, 906–910 (2015).

47. Hochberg, L. R. *et al.* Reach and grasp by people with tetraplegia using a neurally controlled robotic arm. *Nature* **485**, 372–375 (2012).

48. Hochberg, L. R. *et al.* Neuronal ensemble control of prosthetic devices by a human with tetraplegia. *Nature* **442**, 164–171 (2006).

49. Penfield, W. & Boldrey, E. Somatic motor and sensory representation in the cerebral cortex of man as studied by electrical stimulation. *Brain* **60**, 389–443 (1937).

50. Brandman, D. M., Cash, S. S. & Hochberg, L. R. Review: Human Intracortical Recording and Neural Decoding for Brain-Computer Interfaces. *IEEE Transactions on Neural Systems and Rehabilitation Engineering* **25**, 1687–1696 (2017).

51. Salari, E. *et al.* Classification of Articulator Movements and Movement Direction from Sensorimotor Cortex Activity. *Scientific Reports* **9**, 1–12 (2019).

52. Rabbani, Q., Milsap, G. & Crone, N. E. The Potential for a Speech Brain–Computer Interface Using Chronic Electrocorticography. *Neurotherapeutics* vol. 16 144–165 (2019).

53. Moses, D. A. *et al.* Neuroprosthesis for Decoding Speech in a Paralyzed Person with Anarthria. *New England Journal of Medicine* **385**, 217–227 (2021).

54. Ramsey, N. F. *et al.* Decoding spoken phonemes from sensorimotor cortex with high-density ECoG grids. *NeuroImage* **180**, 301–311 (2018).

55. Emmerling, T. C., Zimmermann, J., Sorger, B., Frost, M. A. & Goebel, R. Decoding the direction of imagined visual motion using 7 T ultra-high field fMRI. *NeuroImage* **125**, 61–73 (2016).

56. Kamitani, Y. & Tong, F. Decoding the visual and subjective contents of the human brain. *Nature Neuroscience* **8**, 679–685 (2005).

57. Harrison, S. A. & Tong, F. Decoding reveals the contents of visual working memory in early visual areas. *Nature* **458**, 632–635 (2009).

58. Albers, A. M., Kok, P., Toni, I., Dijkerman, H. C. & de Lange, F. P. Shared representations for working memory and mental imagery in early visual cortex. *Current Biology* **23**, 1427–1431 (2013).

59. Cichy, R. M., Heinzle, J. & Haynes, J. D. Imagery and perception share cortical representations of content and location. *Cerebral Cortex* **22**, 372–380 (2012).

60. Stokes, M., Thompson, R., Cusack, R. & Duncan, J. Top-down activation of shape-specific population codes in visual cortex during mental imagery. *The Journal of neuroscience* **29**, 1565–1572 (2009).

61. Stokes, M., Saraiva, A., Rohenkohl, G. & Nobre, A. C. Imagery for shapes activates position-invariant representations in human visual cortex. *NeuroImage* **56**, 1540–1545 (2011).

62. Sereno, M. I. *et al.* Borders of multiple visual areas in humans revealed by functional magnetic resonance imaging. *Science (New York, N.Y.)* **268**, 889–893 (1995).

63. DeYoe, E. *et al.* Mapping striate and extrastriate visual areas in human cerebral cortex. *Proc Natl Acad Sci* **93**, 2382–6 (1996).

64. Engel, S. A. *et al.* FMRI of human visual cortex. *Nature* vol. 369 525 (1994).

65. Engel, S. A., Glover, G. H. & Wandell, B. A. Retinotopic organization in human visual cortex and the spatial precision of functional MRI. *Cerebral Cortex* **7**, 181–192 (1997).

66. Ramsey, N. F., van de Heuvel, M. P., Kho, K. H. & Leijten, F. S. S. Towards human BCI applications based on cognitive brain systems: An investigation of neural signals recorded from the dorsolateral prefrontal cortex. in *IEEE Transactions on Neural Systems and Rehabilitation Engineering* vol. 14 214–217 (2006).

67. Vansteensel, M. J. *et al.* Brain-computer interfacing based on cognitive control. *Annals of Neurology* **67**, 809–816 (2010).

68. Leinders, S. *et al.* Dorsolateral prefrontal cortex-based control with an implanted brain–computer interface. *Scientific Reports* **10**, 1–10 (2020).

69. Freudenburg, Z. *et al.* The dorsolateral pre-frontal cortex bi-polar error-related potential in a locked-in patient implanted with a daily use brain–computer interface. *Control Theory and Technology* 1–11 (2021) doi:10.1007/s11768-021-00062-y.

70. Sanchez, J. C., Gunduz, A., Carney, P. R. & Principe, J. C. Extraction and localization of mesoscopic motor control signals for human ECoG neuroprosthetics. *Journal of Neuroscience Methods* **167**, 63–81 (2008).

71. Pistohl, T., Ball, T., Schulze-Bonhage, A., Aertsen, A. & Mehring, C. Prediction of arm movement trajectories from ECoG-recordings in humans. *Journal of Neuroscience Methods* **167**, 105–114 (2008).

72. Schalk, G. *et al.* Decoding two-dimensional movement trajectories using electrocorticographic signals in humans. *Journal of neural engineering* **4**, 264–275 (2007).

73. Acharya, S., Fifer, M. S., Benz, H. L., Crone, N. E. & Thakor, N. V. Electrocorticographic amplitude predicts finger positions during slow grasping motions of the hand. *Journal of Neural Engineering* **7**, 046002 (2010).

74. Wang, Z., Ji, Q., Miller, K. J. & Schalk, G. Prior knowledge improves decoding of finger flexion from electrocorticographic signals. *Frontiers in Neuroscience* **5**, 127 (2011).

75. Flamary, R. & Rakotomamonjy, A. Decoding finger movements from ECoG signals using switching linear models. *Frontiers in Neuroscience* **6**, 29 (2012).

76. Schoenmakers, S., Barth, M., Heskes, T. & van Gerven, M. Linear reconstruction of perceived images from human brain activity. *NeuroImage* **83**, 951–961 (2013).

77. Miyawaki, Y. *et al.* Visual Image Reconstruction from Human Brain Activity using a Combination of Multiscale Local Image Decoders. *Neuron* **60**, 915–929 (2008).

78. Shen, G., Horikawa, T., Majima, K. & Kamitani, Y. Deep image reconstruction from human brain activity. *PLoS Computational Biology* **15**, e1006633 (2019).

79. Wen, H. *et al.* Neural encoding and decoding with deep learning for dynamic natural vision. *Cerebral Cortex* **28**, 4136–4160 (2018).

80. Naselaris, T., Prenger, R. J., Kay, K. N., Oliver, M. & Gallant, J. L. Bayesian Reconstruction of Natural Images from Human Brain Activity. *Neuron* **63**, 902–915 (2009).

81. Nishimoto, S. *et al.* Reconstructing visual experiences from brain activity evoked by natural movies. *Current Biology* **21**, 1641–1646 (2011).

82. Yanagisawa, T. *et al.* Electrocorticographic control of a prosthetic arm in paralyzed patients. *Annals of Neurology* **71**, 353–361 (2012).

83. Kellis, S. *et al.* Decoding spoken words using local field potentials recorded from the cortical surface. *Journal of Neural Engineering* **7**, 56007–56017 (2010).

84. Brumberg, J. S., Wright, E. J., Andreasen, D. S., Guenther, F. H. & Kennedy, P. R. Classification of intended phoneme production from chronic intracortical microelectrode recordings in speech-motor cortex. *Frontiers in Neuroscience* **5**, 1–12 (2011).

85. Mugler, E. M. *et al.* Direct classification of all American English phonemes using signals from functional speech motor cortex. *Journal of Neural Engineering* **11**, 035015 (2014).

86. Herff, C. *et al.* Brain-to-text: Decoding spoken phrases from phone representations in the brain. *Frontiers in Neuroscience* **9**, 217 (2015).

87. Stavisky, S. D. *et al.* Decoding Speech from Intracortical Multielectrode Arrays in Dorsal "Arm/Hand Areas" of Human Motor Cortex. in *Proceedings of the Annual International Conference of the IEEE Engineering in Medicine and Biology Society, EMBS* vols. 2018-July 93–97 (Institute of Electrical and Electronics Engineers Inc., 2018).

88. Conant, D. F., Bouchard, K. E., Leonard, M. K. & Chang, E. F. Human Sensorimotor Cortex Control of Directly Measured Vocal Tract Movements during Vowel Production. *Journal of Neuroscience* **38**, 2955–2966 (2018).

89. Ibayashi, K. *et al.* Decoding speech with integrated hybrid signals recorded from the human ventral motor cortex. *Frontiers in Neuroscience* **12**, 221 (2018).

90. Anumanchipalli, G. K., Chartier, J. & Chang, E. F. Speech synthesis from neural decoding of spoken sentences. *Nature* **568**, 493–498 (2019).

91. Sun, P., Anumanchipalli, G. K. & Chang, E. F. Brain2Char: A deep architecture for decoding text from brain recordings. *Journal of Neural Engineering* **17**, 066015 (2020).

92. Bleichner, M. G., Jansma, J. M., Sellmeijer, J., Raemaekers, M. & Ramsey, N. F. Give me a sign: Decoding complex coordinated hand movements using high-field fMRI. *Brain Topography* **27**, 248–257 (2014).

93. Bleichner, M. G. *et al.* Give me a sign: decoding four complex hand gestures based on high-density ECoG. *Brain Structure and Function* **221**, 203–216 (2016).

94. van den Boom, M. A., Miller, K. J., Ramsey, N. F. & Hermes, D. Functional MRI based simulations of ECoG grid configurations for optimal measurement of spatially distributed hand-gesture information. *Journal of Neural Engineering* **18**, 026013 (2021).

95. Li, Y. *et al.* Gesture Decoding Using ECoG Signals from Human Sensorimotor Cortex: A Pilot Study. *Behavioural Neurology* **2017**, (2017).

96. Patterson, J. R. & Grabois, M. Locked-in syndrome: A review of 139 cases. *Stroke* **17**, 758–764 (1986).

97. Lacourse, M. G., Cohen, M. J., Lawrence, K. E. & Romero, D. H. Cortical potentials during imagined movements in individuals with chronic spinal cord injuries. *Behavioural Brain Research* **104**, 73–88 (1999).

98. Chang, J. L. *et al.* A voxel-based morphometry study of patterns of brain atrophy in ALS and ALS/FTLD. *Neurology* **65**, 75–80 (2005).

99. Mohammadi, B., Kollewe, K., Samii, A., Dengler, R. & Münte, T. F. Functional neuroimaging at different disease stages reveals distinct phases of neuroplastic changes in amyotrophic lateral sclerosis. *Human Brain Mapping* **32**, 750–758 (2011).

100. Jansma, J. M., Ramsey, N. F., Slagter, H. A. & Kahn, R. S. Functional Anatomical Correlates of Controlled and Automatic Processing. *Journal of Cognitive Neuroscience* **13**, 730–743 (2001).

101. Ramsey, N. F., Jansma, J. M., Jager, G., van Raalten, T. & Kahn, R. S. Neurophysiological factors in human information processing capacity. *Brain : a journal of neurology* **127**, 517–25 (2004).

102. Cohen, L. G., Bandinelli, S., Findley, T. W. & Hallett, M. Motor reorganization after upper limb amputation in man: A study with focal magnetic stimulation. *Brain* **114**, 615–627 (1991).

103. Röricht, S., Meyer, B. U., Niehaus, L. & Brandt, S. A. Long-term reorganization of motor cortex outputs after arm amputation. *Neurology* **53**, 106–111 (1999).

104.   Elbert, T. *et al.* Extensive reorganization of the somatosensory cortex in adult humans after nervous system injury. *NeuroReport* **5**, 2593–2597 (1994).

105.   Dettmers, C. *et al.* Increased excitability in the primary motor cortex and supplementary motor area in patients with phantom limb pain after upper limb amputation. *Neuroscience Letters* **307**, 109–112 (2001).

106.   Lotze, M., Flor, H., Grodd, W., Larbig, W. & Birbaumer, N. Phantom movements and pain an fMRI study in upper limb amputees. *Brain* **124**, 2268–2277 (2001).

107.   Qi, H. X., Stepniewska, I. & Kaas, J. H. Reorganization of primary motor cortex in adult macaque monkeys with long-standing amputations. *Journal of Neurophysiology* **84**, 2133–2147 (2000).

108.   Kambi, N. *et al.* Large-scale reorganization of the somatosensory cortex following spinal cord injuries is due to brainstem plasticity. *Nature Communications* **5**, 1–10 (2014).

109.   Hugdahl, K. *et al.* Common pathways in mental imagery and pain perception: An fMRI study of a subject with an amputated arm. *Scandinavian Journal of Psychology* **42**, 269–275 (2001).

110.   Turner, J. A. *et al.* Somatotopy of the motor cortex after long-term spinal cord injury or amputation. *IEEE Transactions on Neural Systems and Rehabilitation Engineering* **9**, 154–160 (2001).

111.   Roux, F. E. *et al.* Cortical Areas Involved in Virtual Movement of Phantom Limbs: Comparison with Normal Subjects. *Neurosurgery* **53**, 1342–1353 (2003).

112.   Kikkert, S. *et al.* Revealing the neural fingerprints of a missing hand. *eLife* **5**, (2016).

113.   Wesselink, D. B. *et al.* Obtaining and maintaining cortical hand representation as evidenced from acquired and congenital handlessness. *eLife* **8**, (2019).

114.   Flesher, S. N. *et al.* Intracortical microstimulation of human somatosensory cortex. *Science Translational Medicine* **8**, 361ra141-361ra141 (2016).

115.   Salas, M. A. *et al.* Proprioceptive and cutaneous sensations in humans elicited by intracortical microstimulation. *eLife* **7**, (2018).

116.   Bruno, V., Ronga, I., Fossataro, C., Capozzi, F. & Garbarini, F. Suppressing movements with phantom limbs and existing limbs evokes comparable electrophysiological inhibitory responses. *Cortex* **117**, 64–76 (2019).

117.   Yanagisawa, T. *et al.* BCI training to move a virtual hand reduces phantom limb pain: A randomized crossover trial. *Neurology* **95**, E417–E426 (2020).

118.   Krushelnytskyy, M. D. *et al.* Chronic subdural cortical stimulation for phantom limb pain: report of a series of two cases. *Acta Neurochirurgica* **161**, 925–934 (2019).

119.   Hanakawa, T., Parikh, S., Bruno, M. K. & Hallett, M. Finger and Face Representations in the Ipsilateral Precentral Motor Areas in Humans. *Journal of Neurophysiology* **93**, 2950–2958 (2005).

120.   Verstynen, T., Diedrichsen, J., Albert, N., Aparicio, P. & Ivry, R. B. Ipsilateral motor cortex activity during unimanual hand movements relates to task complexity. *Journal of Neurophysiology* **93**, 1209–1222 (2005).

121.   Hlushchuk, Y. & Hari, R. Transient suppression of ipsilateral primary somatosensory cortex during tactile finger stimulation. *Journal of Neuroscience* **26**, 5819–5824 (2006).

122.   Horenstein, C., Lowe, M. J., Koenig, K. A. & Phillips, M. D. Comparison of unilateral and bilateral complex finger tapping-related activation in premotor and primary motor cortex. *Human Brain Mapping* **30**, 1397–1412 (2009).

123.   Diedrichsen, J., Wiestler, T. & Krakauer, J. W. Two distinct ipsilateral cortical representations for individuated finger movements. *Cerebral Cortex* **23**, 1362–1377 (2013).

124.   Valyear, K. F. *et al.* Interhemispheric transfer of post-amputation cortical plasticity within the human somatosensory cortex. *NeuroImage* **206**, (2020).

125.   Evarts, E. v. Motor cortex reflexes associated with learned movement. *Science* **179**, 501–503 (1973).

126. Cheney, P. D. & Fetz, E. E. Corticomotoneuronal cells contribute to long-latency stretch reflexes in the rhesus monkey. *The Journal of Physiology* **349**, 249–272 (1984).

127. Welch, P. D. The Use of Fast Fourier Transform for the Estimation of Power Spectra: A Method Based on Time Averaging Over Short, Modified Periodograms. *IEEE Transactions on Audio and Electroacoustics* **15**, 70–73 (1967).

128. Nuttall, A. H. Some Windows with Very Good Sidelobe Behavior. *IEEE Transactions on Acoustics, Speech, and Signal Processing* **29**, 84–91 (1981).

129. Miller, K. J., Sorensen, L. B., Ojemann, J. G. & den Nijs, M. Power-law scaling in the brain surface electric potential. *PLoS Computational Biology* **5**, 1000609 (2009).

130. Bishop, C. M. *Machine Learning and Pattern Recoginiton. Information Science and Statistics* (Springer-Verlag New York, 2006).

131. Combrisson, E. & Jerbi, K. Exceeding chance level by chance: The caveat of theoretical chance levels in brain signal classification and statistical assessment of decoding accuracy. *Journal of Neuroscience Methods* **250**, 126–136 (2015).

132. Davison, A. C. & Hinkley, D. v. *Bootstrap Methods and their Application. Bootstrap Methods and their Application* (1997). doi:10.1017/cbo9780511802843.

133. Dechent, P. & Frahm, J. Functional somatopy of finger representations in human primary motor cortex. *Human Brain Mapping* **18**, 272–283 (2003).

134. Schellekens, W., Petridou, N. & Ramsey, N. F. Detailed somatotopy in primary motor and somatosensory cortex revealed by Gaussian population receptive fields. *NeuroImage* **179**, 337–347 (2018).

135. Huber, L. *et al.* Sub-millimeter fMRI reveals multiple topographical digit representations that form action maps in human motor cortex. *NeuroImage* **208**, 116463 (2020).

136. Freudenburg, Z. v. *et al.* Sensorimotor ECoG Signal Features for BCI Control: A Comparison Between People With Locked-In Syndrome and Able-Bodied Controls. *Frontiers in Neuroscience* **13**, (2019).

137. Bai, O., Lin, P., Huang, D., Fei, D. Y. & Floeter, M. K. Towards a user-friendly brain-computer interface: Initial tests in ALS and PLS patients. *Clinical Neurophysiology* **121**, 1293–1303 (2010).

138. Riva, N. *et al.* Cortical activation to voluntary movement in amyotrophic lateral sclerosis is related to corticospinal damage: Electrophysiological evidence. *Clinical Neurophysiology* **123**, 1586–1592 (2012).

139. Proudfoot, M. *et al.* Altered cortical beta-band oscillations reflect motor system degeneration in amyotrophic lateral sclerosis. *Human Brain Mapping* **38**, 237–254 (2017).

140. Kasahara, T. *et al.* The correlation between motor impairments and event-related desynchronization during motor imagery in ALS patients. *BMC Neuroscience* **13**, 1–10 (2012).

141. Höhne, J. *et al.* Motor imagery for severely motor-impaired patients: Evidence for brain-computer interfacing as superior control solution. *PLoS ONE* **9**, e104854 (2014).

142. Hermes, D. *et al.* Dissociation between neuronal activity in sensorimotor cortex and hand movement revealed as a function of movement rate. *Journal of Neuroscience* **32**, 9736–9744 (2012).

143. Papadelis, C., Kourtidou-Papadeli, C., Bamidis, P. & Albani, M. Effects of imagery training on cognitive performance and use of physiological measures as an assessment tool of mental effort. *Brain and Cognition* **64**, 74–85 (2007).

144. Jacquet, T. *et al.* Mental fatigue induced by prolonged motor imagery increases perception of effort and the activity of motor areas. *Neuropsychologia* **150**, 107701 (2020).

145. Bruurmijn, M. L. C. M., Pereboom, I. P. L., Vansteensel, M. J., Raemaekers, M. A. H. & Ramsey, N. F. Preservation of hand movement representation in the sensorimotor areas of amputees. *Brain* **140**, 3166–3178 (2017).

146. Smirnakis, S. M. *et al.* Lack of long-term cortical reorganization after macaque retinal lesions. *Nature* **435**, 300–307 (2005).

147. Yang, T. T. *et al.* Sensory maps in the human brain [13]. *Nature* vol. 368 592–593 (1994).

148. Flor, H., Nikolajsen, L. & Jensen, T. S. Phantom limb pain: A case of maladaptive CNS plasticity? *Nature Reviews Neuroscience* vol. 7 873–881 (2006).

149. Flor, H. *et al.* Phantom-limb pain as a perceptual correlate of cortical reorganization following arm amputation. *Nature* **375**, 482–484 (1995).

150. Birbaumer, N. *et al.* Effects of regional anesthesia on phantom limb pain are mirrored in changes in cortical reorganization. *Journal of Neuroscience* **17**, 5503–5508 (1997).

151. Karl, A., Birbaumer, N., Lutzenberger, W., Cohen, L. G. & Flor, H. Reorganization of motor and somatosensory cortex in upper extremity amputees with phantom limb pain. *Journal of Neuroscience* **21**, 3609–3618 (2001).

152. Diers, M., Christmann, C., Koeppe, C., Ruf, M. & Flor, H. Mirrored, imagined and executed movements differentially activate sensorimotor cortex in amputees with and without phantom limb pain. *Pain* **149**, 296–304 (2010).

153. Giraux, P. & Sirigu, A. Illusory movements of the paralyzed limb restore motor cortex activity. in *NeuroImage* **20**, S107–S111 (Academic Press Inc., 2003).

154. Moseley, G. L. Graded motor imagery for pathologic pain: A randomized controlled trial. *Neurology* **67**, 2129–2134 (2006).

155. Brodie, E. E., Whyte, A. & Niven, C. A. Analgesia through the looking-glass? A randomized controlled trial investigating the effect of viewing a 'virtual' limb upon phantom limb pain, sensation and movement. *European Journal of Pain* **11**, 428–436 (2007).

156. Chan, B. L. *et al.* Mirror Therapy for Phantom Limb Pain. *New England Journal of Medicine* **357**, 2206–2207 (2007).

157. MacIver, K., Lloyd, D. M., Kelly, S., Roberts, N. & Nurmikko, T. Phantom limb pain, cortical reorganization and the therapeutic effect of mental imagery. *Brain* **131**, 2181–2191 (2008).

158. Makin, T. R. *et al.* Phantom pain is associated with preserved structure and function in the former hand area. *Nature Communications* **4**, 1–8 (2013).

159. Kikkert, S., Johansen-Berg, H., Tracey, I. & Makin, T. R. Reaffirming the link between chronic phantom limb pain and maintained missing hand representation. *Cortex* **106**, 174–184 (2018).

160. Makin, T. R., Scholz, J., Henderson Slater, D., Johansen-Berg, H. & Tracey, I. Reassessing cortical reorganization in the primary sensorimotor cortex following arm amputation. *Brain* **138**, 2140–2146 (2015).

161. Flor, H., Diers, M. & Andoh, J. The neural basis of phantom limb pain. *Trends in Cognitive Sciences* vol. 17 307–308 (2013).

162. Makin, T. R. & Flor, H. Brain (re)organisation following amputation: Implications for phantom limb pain. *NeuroImage* **218**, 116943 (2020).

163. Yanagisawa, T. *et al.* Induced sensorimotor brain plasticity controls pain in phantom limb patients. *Nature communications* **7**, 13209 (2016).

164. Miller, K. J., Abel, T. J., Hebb, A. O. & Ojemann, J. G. Reorganization of large-scale physiology in hand motor cortex following hemispheric stroke. *Neurology* **76**, 927–929 (2011).

165. Hermes, D. *et al.* Functional MRI-based identification of brain areas involved in motor imagery for implantable brain-computer interfaces. in *Journal of Neural Engineering* vol. 8 025007 (2011).

166. Zanos, S., Miller, K. J. & Ojemann, J. G. Electrocorticographic spectral changes associated with ipsilateral individual finger and whole hand movement. in *Proceedings of the 30th Annual International Conference of the IEEE Engineering in Medicine and Biology Society, EMBS'08 - "Personalized Healthcare through Technology"* 5939–5942 (IEEE Computer Society, 2008). doi:10.1109/iembs.2008.4650569.

167. Talelli, P., Waddingham, W., Ewas, A., Rothwell, J. C. & Ward, N. S. The effect of age on task-related modulation of interhemispheric balance. *Experimental Brain Research* **186**, 59–66 (2008).

168. Talelli, P., Ewas, A., Waddingham, W., Rothwell, J. C. & Ward, N. S. Neural correlates of age-related changes in cortical neurophysiology. *NeuroImage* **40**, 1772–1781 (2008).

169. Freeman, W. J. Mesoscopic neurodynamics: From neuron to brain. in *Journal of Physiology Paris* vol. 94 303–322 (Elsevier, 2000).

170. Schalk, G. *et al.* Two-dimensional movement control using electrocorticographic signals in humans. *Journal of Neural Engineering* **5**, 75–84 (2008).

171. Buzsáki, G., Anastassiou, C. A. & Koch, C. The origin of extracellular fields and currents-EEG, ECoG, LFP and spikes. *Nature Reviews Neuroscience* **13**, 407–420 (2012).

172. Miller, K. J., Hermes, D. & Staff, N. P. The current state of electrocorticography-based brain-computer interfaces. *Neurosurgical Focus* **49**, E2 (2020).

173. Pistohl, T., Schulze-Bonhage, A., Aertsen, A., Mehring, C. & Ball, T. Decoding natural grasp types from human ECoG. *NeuroImage* **59**, 248–260 (2012).

174. Oldfield, R. C. The assessment and analysis of handedness: The Edinburgh inventory. *Neuropsychologia* **9**, 97–113 (1971).

175. Dale, A. M., Fischl, B. & Sereno, M. I. Cortical surface-based analysis: I. Segmentation and surface reconstruction. *NeuroImage* **9**, 179–194 (1999).

176. Andersson, J. L. R., Skare, S. & Ashburner, J. How to correct susceptibility distortions in spin-echo echo-planar images: Application to diffusion tensor imaging. *NeuroImage* **20**, 870–888 (2003).

177. Kriegeskorte, N., Goebel, R. & Bandettini, P. Information-based functional brain mapping. *Proceedings of the National Academy of Sciences of the United States of America* **103**, 3863–3868 (2006).

178. Desikan, R. S. *et al.* An automated labeling system for subdividing the human cerebral cortex on MRI scans into gyral based regions of interest. *NeuroImage* **31**, 968–980 (2006).

179. Beisteiner, R. *et al.* Finger somatotopy in human motor cortex. *NeuroImage* **13**, 1016–1026 (2001).

180. Hlustik, P., Solodkin, A., Gullapalli, R. P., Noll, D. C. & Small, S. L. Somatotopy in Human Primary Motor and Somatosensory Hand Representations Revisited. *Cerebral Cortex* **11**, 312–321 (2001).

181. Olman, C. A., Pickett, K. A., Schallmo, M. P. & Kimberley, T. J. Selective BOLD responses to individual finger movement measured with fMRI at 3T. *Human Brain Mapping* **33**, 1594–1606 (2012).

182. Bundy, D. T., Pahwa, M., Szrama, N. & Leuthardt, E. C. Decoding three-dimensional reaching movements using electrocorticographic signals in humans. *Journal of Neural Engineering* **13**, 026021 (2016).

183. Salari, E., Freudenburg, Z. V., Vansteensel, M. J. & Ramsey, N. F. Classification of Facial Expressions for Communication of Emotions Using BCI. *Annals of Neurology* (2020).

184. Freeman, W. J., Rogers, L. J., Holmes, M. D. & Silbergeld, D. L. Spatial spectral analysis of human electrocorticograms including the alpha and gamma bands. *Journal of Neuroscience Methods* **95**, 111–121 (2000).

185. Slutzky, M. W. *et al.* Optimal spacing of surface electrode arrays for brain-machine interface applications. *Journal of Neural Engineering* **7**, 026004 (2010).

186. Chang, E. F. *et al.* Categorical speech representation in human superior temporal gyrus. *Nature Neuroscience* **13**, 1428–1432 (2010).

187. Edelstein, W. A., Glover, G. H., Hardy, C. J. & Redington, R. W. The intrinsic signal-to-noise ratio in NMR imaging. *Magnetic Resonance in Medicine* **3**, 604–618 (1986).

188. Parrish, T. B., Gitelman, D. R., LaBar, K. S. & Mesulam, M. M. Impact of signal-to-noise on functional MRI. *Magnetic Resonance in Medicine* **44**, 925–932 (2000).

189. Toda, H. *et al.* Simultaneous recording of ECoG and intracortical neuronal activity using a flexible multichannel electrode-mesh in visual cortex. *NeuroImage* **54**, 203–212 (2011).

190. Kanth, S. T. & Ray, S. Electrocorticogram (ECoG) Is Highly Informative in Primate Visual Cortex. *The Journal of neuroscience : the official journal of the Society for Neuroscience* **40**, 2430–2444 (2020).

191. Beauchamp, M. S. *et al.* Dynamic Stimulation of Visual Cortex Produces Form Vision in Sighted and Blind Humans. *Cell* **181**, 774-783.e5 (2020).

192. Leuthardt, E. C., Freudenberg, Z., Bundy, D. & Roland, J. Microscale recording from human motor cortex: Implications for minimally invasive electrocorticographic brain-computer interfaces. *Neurosurgical Focus* **27**, E10 (2009).

193. Reisch, R., Stadie, A., Kockro, R. A. & Hopf, N. The keyhole concept in neurosurgery. *World Neurosurgery* **79**, S17.e9-S17.e13 (2013).

194. Wong, C. H. *et al.* Risk factors for complications during intracranial electrode recording in presurgical evaluation of drug resistant partial epilepsy. *Acta Neurochirurgica* **151**, 37–50 (2009).

195. American Congress of Rehabilitation Medicine. Recommendations for use of uniform nomenclature pertinent to patients with severe alterations in consciousness. *Archives of Physical Medicine and Rehabilitation* **76**, 205–209 (1995).

196. Spataro, R., Ciriacono, M., Manno, C. & la Bella, V. The eye-tracking computer device for communication in amyotrophic lateral sclerosis. *Acta Neurologica Scandinavica* **130**, 40–45 (2014).

197. Wolpaw, J. R., Birbaumer, N., McFarland, D. J., Pfurtscheller, G. & Vaughan, T. M. Brain-computer interfaces for communication and control. *Clinical Neurophysiology* , **113**, 767–791 (2002).

198. Chaudhary, U., Birbaumer, N. & Ramos-Murguialday, A. Brain-computer interfaces for communication and rehabilitation. *Nature Reviews Neurology* **12**, 513–525 (2016).

199. Ganis, G., Thompson, W. L. & Kosslyn, S. M. Brain areas underlying visual mental imagery and visual perception: An fMRI study. *Cognitive Brain Research* **20**, 226–241 (2004).

200. Kosslyn, S. M., Thompson, W. L. & Alpert, N. M. Neural systems shared by visual imagery and visual perception: A positron emission tomography study. *NeuroImage* **6**, 320–334 (1997).

201. Kosslyn, S. M., Thompson, W. L. & Ganis, Giorgio. *The Case for Mental Imagery*. (Oxford University Press, 2006).

202. Kosslyn, S. M., Thompson, W. L., Klm, I. J. & Alpert, N. M. Topographical representations of mental images in primary visual cortex. *Nature* **378**, 496–498 (1995).

203. Klein, I. *et al.* Retinotopic organization of visual mental images as revealed by functional magnetic resonance imaging. *Cognitive Brain Research* **22**, 26–31 (2004).

204. Slotnick, S. D., Thompson, W. L. & Kosslyn, S. M. Visual mental imagery induces retinotopically organized activation of early visual areas. *Cerebral Cortex* **15**, 1570–1583 (2005).

205. Thirion, B. *et al.* Inverse retinotopy: Inferring the visual content of images from brain activation patterns. *NeuroImage* **33**, 1104–1116 (2006).

206. Johnson, M. R. & Johnson, M. K. Decoding individual natural scene representations during perception and imagery. *Frontiers in Human Neuroscience* **8**, 59 (2014).

207. Naselaris, T., Olman, C. A., Stansbury, D. E., Ugurbil, K. & Gallant, J. L. A voxel-wise encoding model for early visual areas decodes mental images of remembered scenes. *NeuroImage* **105**, 215–228 (2015).

208. Reddy, L., Tsuchiya, N. & Serre, T. Reading the mind's eye: Decoding category information during mental imagery. *NeuroImage* **50**, 818–825 (2010).

209. Triantafyllou, C. *et al.* Comparison of physiological noise at 1.5 T, 3 T and 7 T and optimization of fMRI acquisition parameters. *NeuroImage* **26**, 243–250 (2005).

210. Wang, L., Mruczek, R. E. B., Arcaro, M. J. & Kastner, S. Probabilistic maps of visual topography in human cortex. *Cerebral Cortex* **25**, 3911–3931 (2015).

211. Nichols, T. E. & Holmes, A. P. Nonparametric Permutation Tests for functional Neuroimaging Experiments: A Primer with examples. *Human Brain Mapping* **15**, 1–25 (2001).

212. LaConte, S. *et al.* The evaluation of preprocessing choices in single-subject BOLD fMRI using NPAIRS performance metrics. *NeuroImage* **18**, 10–27 (2003).

213. Benjamini, Y. & Hochberg, Y. Controlling the False Discovery Rate: a Practical and Powerful Approach to Multiple Testing. *Journal of the Royal Statistical Society* **57**, 289–300 (1995).

214. Cui, X., Jeter, C. B., Yang, D., Montague, P. R. & Eagleman, D. M. Vividness of mental imagery: Individual variability can be measured objectively. *Vision Research* **47**, 474–478 (2007).

215. Dijkstra, N., Bosch, S. E. & van Gerven, M. A. J. Vividness of Visual Imagery Depends on the Neural Overlap with Perception in Visual Areas. *The Journal of Neuroscience* **37**, 1367–1373 (2017).

216. Kosslyn, S. M., Thompson, W. L., Kim, I. J., Rauch, S. L. & Alpert, N. M. Individual differences in cerebral blood flow in area 17 predict the time to evaluate visualized letters. *Journal of Cognitive Neuroscience* **8**, 78–82 (1996).

217. Bergmann, J., Genç, E., Kohler, A., Singer, W. & Pearson, J. Smaller primary visual cortex is associated with stronger, but less precise mental imagery. *Cerebral Cortex* **26**, 3838–3850 (2016).

218. Pylyshyn, Z. W. What the mind's eye tells the mind's brain: A critique of mental imagery. *Psychological Bulletin* **80**, 1–24 (1973).

219. Kosslyn, S. M. *Image and Brain: The Resolution of the Imagery Debate. MIT Press, Cambridge (MA).* (Cambridge: MIT Press, 1994). doi:10.1162/jocn.1995.7.3.415.

220. Pearson, J. & Kosslyn, S. M. The heterogeneity of mental representation: Ending the imagery debate. *Proceedings of the National Academy of Sciences* **112**, 10089–10092 (2015).

221. Liu, J. & Wandell, B. A. Specializations for Chromatic and Temporal Signals in Human Visual Cortex. *Journal of Neuroscience* **25**, 3459–3468 (2005).

222. Horiguchi, H., Nakadomari, S., Misaki, M. & Wandell, B. A. Two temporal channels in human V1 identified using fMRI. *NeuroImage* **47**, 273–280 (2009).

223. Gaglianese, A. *et al.* Correspondence between fMRI and electrophysiology during visual motion processing in human MT+. *NeuroImage* **155**, 480–489 (2017).

224. Vetter, P., Smith, F. W. & Muckli, L. Decoding sound and imagery content in early visual cortex. *Current Biology* **24**, 1256–1262 (2014).

225. Senden, M., Emmerling, T. C., van Hoof, R., Frost, M. A. & Goebel, R. Reconstructing imagined letters from early visual cortex reveals tight topographic correspondence between visual mental imagery and perception. *Brain Structure and Function* **224**, 1167–1183 (2019).

226. Baddeley, A. Working memory: looking back and looking forward. *Nature Reviews Neuroscience* **4**, 829–839 (2003).

227. Baddeley, A. D. & Hitch, G. Working memory. *Psychology of learning and motivation* **8**, 47–89 (1974).

228. Cowan, N. Metatheory of storage capacity limits. *Behavioral and Brain Sciences* **24**, 154–176 (2001).

229. Miller, G. The magical number seven, plus or minus two: some limits on our capacity for processing information. *Psychological review* **101**, 343–352 (1956).

230. Jansma, J. M., Ramsey, N. F., van der Wee, N. J. A. & Kahn, R. S. Working memory capacity in schizophrenia: A parametric fMRI study. *Schizophrenia Research* **68**, 159–171 (2004).

231. Potkin, S. G. *et al.* Working memory and DLPFC inefficiency in schizophrenia: The FBIRN study. *Schizophrenia Bulletin* **35**, 19–31 (2009).

232. van Raalten, T. R., Ramsey, N. F., Jansma, J. M., Jager, G. & Kahn, R. S. Automatization and working memory capacity in schizophrenia. *Schizophrenia Research* **100**, 161–171 (2008).

233. Harvey, P. O. *et al.* Cognitive control and brain resources in major depression: An fMRI study using the n-back task. *NeuroImage* **26**, 860–869 (2005).

234. Wagner, G. *et al.* Cortical Inefficiency in Patients with Unipolar Depression: An Event-Related fMRI Study with the Stroop Task. *Biological Psychiatry* **59**, 958–965 (2006).

235. Berlim, M. T., van den Eynde, F., Tovar-Perdomo, S. & Daskalakis, Z. J. Response, remission and drop-out rates following high-frequency repetitive transcranial magnetic stimulation (rTMS) for treating

major depression: A systematic review and meta-analysis of randomized, double-blind and sham-controlled trials. *Psychological Medicine* **44**, 225–239 (2014).

236. Berlim, M. T., van den Eynde, F. & Daskalakis, Z. J. Clinically meaningful efficacy and acceptability of low-frequency repetitive transcranial magnetic stimulation (rTMS) for treating primary major depression: a meta-analysis of randomized, double-blind and sham-controlled trials. *Neuropsychopharmacology* **38**, 543–551 (2013).

237. Goldstein, R. Z. & Volkow, N. D. Dysfunction of the prefrontal cortex in addiction: neuroimaging findings and clinical implications. *Nature reviews. Neuroscience* **12**, 652–69 (2011).

238. Thibault, R. T., Lifshitz, M. & Raz, A. The self-regulating brain and neurofeedback: Experimental science and clinical promise. *Cortex* vol. 74 247–261 (2016).

239. Weiskopf, N. Real-time fMRI and its application to neurofeedback. *NeuroImage* **62**, 682–692 (2012).

240. Hamilton, J. P., Glover, G. H., Hsu, J. J., Johnson, R. F. & Gotlib, I. H. Modulation of subgenual anterior cingulate cortex activity with real-time neurofeedback. *Human Brain Mapping* **32**, 22–31 (2011).

241. Zotev, V. *et al.* Self-Regulation of Amygdala Activation Using Real-Time fMRI Neurofeedback. *PLoS ONE* **6**, e24522 (2011).

242. Sitaram, R. *et al.* Acquired Control of Ventral Premotor Cortex Activity by Feedback Training An Exploratory Real-Time fMRI and TMS Study. *Neurorehabilitation and Neural Repair* **26**, 256–265 (2012).

243. Andersson, P. *et al.* Real-Time Decoding of Brain Responses to Visuospatial Attention Using 7T fMRI. *PLoS ONE* **6**, e27638 (2011).

244. Andersson, P., Pluim, J. P. W., Viergever, M. A. & Ramsey, N. F. Navigation of a Telepresence Robot via Covert Visuospatial Attention and Real-Time fMRI. *Brain Topography* **26**, 177–185 (2012).

245. Haller, S., Birbaumer, N. & Veit, R. Real-time fMRI feedback training may improve chronic tinnitus. *European Radiology* **20**, 696–703 (2010).

246. D'Esposito, M. *et al.* The neural basis of the central executive system of working memory. *Nature* **378**, 279–281 (1995).

247. Jansma, J. M. *et al.* fMRI guided rTMS evidence for reduced left prefrontal involvement after task practice. *PLoS ONE* **8**, e80256 (2013).

248. Wager, T. D. & Smith, E. E. Neuroimaging studies of working memory: a meta-analysis. *Cognitive, Affective & Behavioral neuroscience* **3**, 255–274 (2003).

249. Shen, J., Zhang, G., Yao, L. & Zhao, X. Real-time fMRI training-induced changes in regional connectivity mediating verbal working memory behavioral performance. *Neuroscience* **289**, 144–152 (2015).

250. Sherwood, M. S., Kane, J. H., Weisend, M. P. & Parker, J. G. Enhanced control of dorsolateral prefrontal cortex neurophysiology with real-time functional magnetic resonance imaging (rt-fMRI) neurofeedback training and working memory practice. *NeuroImage* **124**, 214–223 (2016).

251. Zhang, G., Yao, L., Shen, J., Yang, Y. & Zhao, X. Reorganization of functional brain networks mediates the improvement of cognitive performance following real-time neurofeedback training of working memory. *Human Brain Mapping* **36**, 1705–1715 (2015).

252. Zhang, G., Yao, L., Zhang, H., Long, Z. & Zhao, X. Improved Working Memory Performance through Self-Regulation of Dorsal Lateral Prefrontal Cortex Activation Using Real-Time fMRI. *PLoS ONE* **8**, e73735 (2013).

253. McGonigle, D. J. *et al.* Variability in fMRI: An Examination of Intersession Differences. *NeuroImage* **11**, 708–734 (2000).

254. Zandbelt, B. B. *et al.* Within-subject variation in BOLD-fMRI signal changes across repeated measurements: Quantification and implications for sample size. *NeuroImage* **42**, 196–206 (2008).

255. Tarvainen, M. P., Ranta-Aho, P. O. & Karjalainen, P. A. An advanced detrending method with application to HRV analysis. *IEEE transactions on bio-medical engineering* **49**, 172–175 (2002).

256. Rowe, J. B. & Passingham, R. E. Working memory for location and time: Activity in prefrontal area 46 relates to selection rather than maintenance in memory. *NeuroImage* **14**, 77–86 (2001).

257. Emmert, K. *et al.* Meta-analysis of real-time fMRI neurofeedback studies using individual participant data: How is brain regulation mediated? *NeuroImage* **124**, 806–812 (2016).

258. Ninaus, M. *et al.* Neural substrates of cognitive control under the belief of getting neurofeedback training. *Frontiers in Human Neuroscience* **7**, (2013).

259. Kennedy, D. O. & Scholey, A. B. Glucose administration, heart rate and cognitive performance: Effects of increasing mental effort. *Psychopharmacology* **149**, 63–71 (2000).

260. Thayer, J. F., Hansen, A. L., Saus-Rose, E. & Johnsen, B. H. Heart rate variability, prefrontal neural function, and cognitive performance: The neurovisceral integration perspective on self-regulation, adaptation, and health. *Annals of Behavioral Medicine* **37**, 141–153 (2009).

261. Wood, R., Maraj, B., Lee, C. M. & Reyes, R. Short-term heart rate variability during a cognitive challenge in young and older adults. *Age and Ageing* **31**, 131–135 (2002).

262. Raichle, M. E. & Gusnard, D. A. Appraising the brain's energy budget. *Proceedings of the National Academy of Sciences of the United States of America* **99**, 10237–10239 (2002).

263. Callicott, J. H. *et al.* Complexity of prefrontal cortical dysfunction in schizophrenia: More than up or down. *American Journal of Psychiatry* **160**, 2209–2215 (2003).

264. Karlsgodt, K. H. *et al.* The relationship between performance and fMRI signal during working memory in patients with schizophrenia, unaffected co-twins, and control subjects. *Schizophrenia Research* **89**, 191–197 (2007).

265. Glahn, D. C. *et al.* Beyond hypofrontality: A quantitative meta-analysis of functional neuroimaging studies of working memory in schizophrenia. in *Human Brain Mapping* **25**, 60–69 (Wiley Subscription Services, Inc., A Wiley Company, 2005).

266. Ramsey, N. F. *et al.* Excessive recruitment of neural systems subserving logical reasoning in schizophrenia. *Brain : a journal of neurology* **125**, 1793–1807 (2002).

267. Elliott, R. Executive functions and their disorders. *British Medical Bulletin* vol. 65 49–59 (2003).

268. Goldman-Rakic, P. S. Working memory dysfunction in schizophrenia. *The Journal of Neuropsychiatry and Clinical Neurosciences* **6**, 348–357 (1994).

269. Rose, E. J. & Ebmeier, K. P. Pattern of impaired working memory during major depression. *Journal of Affective Disorders* **90**, 149–161 (2006).

270. Wolf, R. C., Vasic, N., Schönfeldt-Lecuona, C., Ecker, D. & Landwehrmeyer, G. B. Cortical dysfunction in patients with Huntington's disease during working memory performance. *Human Brain Mapping* **30**, 327–339 (2009).

271. George, M. S. & Short, E. B. The Expanding Evidence Base for rTMS Treatment of Depression. *Curr Opin Psychiatry* **26**, 13–18 (2014).

272. deCharms, R. C. *et al.* Learned regulation of spatially localized brain activation using real-time fMRI. *NeuroImage* **21**, 436–443 (2004).

273. Haller, S. *et al.* Dynamic reconfiguration of human brain functional networks through neurofeedback. *NeuroImage* **81**, 243–252 (2013).

274. Rota, G., Handjaras, G., Sitaram, R., Birbaumer, N. & Dogil, G. Reorganization of functional and effective connectivity during real-time fMRI-BCI modulation of prosody processing. *Brain and Language* **117**, 123–132 (2011).

275. Samiee, S., Hajipour, S. & Shamsollahi, M. B. Five-class finger flexion classification using ECoG signals. *2010 International Conference on Intelligent and Advanced Systems, ICIAS 2010* (2010) doi:10.1109/ICIAS.2010.5716225.

276. Miller, K. J., Schalk, G., Hermes, D., Ojemann, J. G. & Rao, R. P. N. Spontaneous Decoding of the Timing and Content of Human Object Perception from Cortical Surface Recordings Reveals

Complementary Information in the Event-Related Potential and Broadband Spectral Change. *PLoS Computational Biology* **12**, e1004660 (2016).

277. Breedlove, J. L., St-Yves, G., Olman, C. A. & Naselaris, T. Generative Feedback Explains Distinct Brain Activity Codes for Seen and Mental Images. *Current Biology* **30**, 2211-2224.e6 (2020).

278. Cardinale, F. *et al.* Stereoelectroencephalography: Surgical methodology, safety, and stereotactic application accuracy in 500 procedures. *Neurosurgery* **72**, 353–366 (2013).

279. Vadera, S. *et al.* Stereoelectroencephalography following subdural grid placement for difficult to localize epilepsy. *Neurosurgery* **72**, 723–729 (2013).

280. Katz, J. S. & Abel, T. J. Stereoelectroencephalography Versus Subdural Electrodes for Localization of the Epileptogenic Zone: What Is the Evidence? *Neurotherapeutics* **16**, 59–66 (2019).

281. Vadera, S., Marathe, A. R., Gonzalez-Martinez, J. & Taylor, D. M. Stereoelectroencephalography for continuous two-dimensional cursor control in a brain-machine interface. *Neurosurgical Focus* **34**, E3–E3 (2013).

282. Murphy, B. A., Miller, J. P., Gunalan, K. & Bolu Ajiboye, A. Contributions of subsurface cortical modulations to discrimination of executed and imagined grasp forces through stereoelectroencephalography. *PLoS ONE* **11**, e0150359 (2016).

283. Bouton, C. *et al.* Decoding Neural Activity in Sulcal and White Matter Areas of the Brain to Accurately Predict Individual Finger Movement and Tactile Stimuli of the Human Hand. *Frontiers in Neuroscience* **15**, 2021.04.06.21255006 (2021).

284. Gharabaghi, A. *et al.* Epidural electrocorticography of phantom hand movement following long-term upper-limb amputation. *Frontiers in Human Neuroscience* **8**, 285 (2014).

285. Wang, Z., Ji, Q., Miller, K. J. & Schalk, G. Decoding finger flexion from electrocorticographic signals using a sparse gaussian process. in *Proceedings - International Conference on Pattern Recognition* 3756–3759 (2010). doi:10.1109/ICPR.2010.915.

286. Pels, E. G. M., Aarnoutse, E. J., Ramsey, N. F. & Vansteensel, M. J. Estimated Prevalence of the Target Population for Brain-Computer Interface Neurotechnology in the Netherlands. *Neurorehabilitation and Neural Repair* **31**, 677–685 (2017).

287. Østlie, K., Skjeldal, O. H., Garfelt, B. & Magnus, P. Adult acquired major upper limb amputation in Norway: Prevalence, demographic features and amputation specific features. A population-based survey. *Disability and Rehabilitation* **33**, 1636–1649 (2011).

288. Andersen-Ranberg, F. & Ebskov, B. Major upper extremity amputation in Denmark. *Acta Orthopaedica* **59**, 321–322 (1988).

289. Ziegler-Graham, K., MacKenzie, E. J., Ephraim, P. L., Travison, T. G. & Brookmeyer, R. Estimating the Prevalence of Limb Loss in the United States: 2005 to 2050. *Archives of Physical Medicine and Rehabilitation* **89**, 422–429 (2008).

290. Ekanayake, J. *et al.* Real-time decoding of covert attention in higher-order visual areas. *NeuroImage* **169**, 462–472 (2018).

291. Horikawa, T. & Kamitani, Y. Generic decoding of seen and imagined objects using hierarchical visual features. *Nature Communications 2017* **8**, 1–15 (2017).

292. Kriegeskorte, N. *et al.* Matching Categorical Object Representations in Inferior Temporal Cortex of Man and Monkey. *Neuron* **60**, 1126–1141 (2008).

293. Tsao, D. Y., Freiwald, W. A., Tootell, R. B. H. & Livingstone, M. S. A cortical region consisting entirely of face-selective cells. *Science* **311**, 670–674 (2006).

294. Huang, W. *et al.* Long short-term memory-based neural decoding of object categories evoked by natural images. *Human Brain Mapping* **41**, 4442–4453 (2020).

295. Cox, D. D. & Savoy, R. L. Functional magnetic resonance imaging (fMRI) "brain reading": detecting and classifying distributed patterns of fMRI activity in human visual cortex. *NeuroImage* **19**, 261–270 (2003).

296. Haxby, J. V. *et al.* Distributed and overlapping representations of faces and objects in ventral temporal cortex. *Science* **293**, 2425–2430 (2001).

297. Mishkin, M., Ungerleider, L. G. & Macko, K. A. Object vision and spatial vision: two cortical pathways. *Trends in Neurosciences* **6**, 414–417 (1983).

298. Goodale, M. A., Milner, A. D., Jakobson, L. S. & Carey, D. P. A neurological dissociation between perceiving objects and grasping them. *Nature 1991 349:6305* **349**, 154–156 (1991).

299. Vijayan, S., Lepage, K. Q., Kopell, N. J. & Cash, S. S. Frontal beta-theta network during REM sleep. *eLife* **6**, (2017).

300. Muzur, A., Pace-Schott, E. F. & Hobson, J. A. The prefrontal cortex in sleep. *Trends in Cognitive Sciences* **6**, 475–481 (2002).

301. Branco, M. P., de Boer, L. M., Ramsey, N. F. & Vansteensel, M. J. Encoding of kinetic and kinematic movement parameters in the sensorimotor cortex: A Brain-Computer Interface perspective. *European Journal of Neuroscience* **50**, 2755–2772 (2019).

302. Xie, Z., Schwartz, O. & Prasad, A. Decoding of finger trajectory from ECoG using deep learning. *Journal of Neural Engineering* **15**, 036009 (2018).

303. Du, A., Yang, S., Liu, W. & Huang, H. Decoding ECoG Signal with Deep Learning Model Based on LSTM. *IEEE Region 10 Annual International Conference, Proceedings/TENCON* **2018-October**, 430–435 (2019).

304. Roy, Y. *et al.* Deep learning-based electroencephalography analysis: a systematic review. *Journal of Neural Engineering* **16**, 051001 (2019).

305. Pan, G. *et al.* Rapid decoding of hand gestures in electrocorticography using recurrent neural networks. *Frontiers in Neuroscience* **12**, 555 (2018).

306. Munzert, J., Lorey, B., reviews, K. Z.-B. research & 2009, undefined. Cognitive motor processes: the role of motor imagery in the study of motor representations. *Elsevier* (2009) doi:10.1016/j.brainresrev.2008.12.024.

Nederlandse samenvatting

Brein-Computer Interfaces (BCI) hebben de potentie om onze levens te verbeteren door ons in staat te stellen om apparaten te bedienen met onze gedachten en intenties. Op dit moment richten BCIs zich voornamelijk op een kleine patiënt populatie. Bijvoorbeeld, op ernstig verlamde mensen die niet meer kunnen praten (b.v. mensen met ALS) en met ingebeelde handbewegingen een alternatief communicatiemiddel kunnen aansturen. Of op mensen met een missend ledemaat, die met hersensignalen een prothese kunnen bedienen. Hoewel huidige BCIs al indrukwekkende resultaten geven, zijn ze beperkt in bediening en het praktisch (dagelijks) gebruik. Om gedigitizeerde hersenactiviteit handig aan te kunnen wenden is er nog veel te ontdekken met verschillende uitdagingen. Deze thesis richt zich op het bevorderen van brein computer koppelingen door de neuronale activiteit van verschillende hersenfuncties en gebieden optimaal te benutten.

Deze thesis bouwt op twee – complementaire – technieken om de hersenactivatie te meten: electrocorticografie (ECoG) en functionele Magnetische Resonantie Imaging (fMRI). Bij ECoG wordt een strip of raster van elektroden onder het schedel op het hersenoppervlak geplaatst waarbij elke elektrode het gecombineerd elektrisch potentiaal van een groep onderliggende neuronen meet. Dit levert informatie met een hoge temporele resolutie en een stabiel signaal over de jaren heen. Daarnaast zijn ECoG-BCIs compact en esthetisch prettig (want geïmplanteerd). Om deze redenen wordt ECoG hier beschouwd als een van de weinige technieken die geschikt is voor een BCI die door patiënten dagelijks thuis gebruikt kan worden. Het nadeel van ECoG is dat het invasief is en een hersenoperatie vereist; mede hierdoor is ECoG onderzoek en zijn ECoG-BCIs relatief schaars. fMRI, daarentegen, meet op een niet-invasieve veilige manier het volledige brein en heeft ons de afgelopen decennia grote hoeveelheden informatie over de werking van het brein verschaft. Bij fMRI worden lokale hemodynamische veranderingen, welke gerelateerd zijn aan de activiteit van neuronen, in het brein gemeten. fMRI kan op een hoge spatiele resolutie indirect hersenactivatie meten, maar metingen kunnen alleen in een grote MRI scanner plaatsvinden. Als gevolg hiervan is fMRI niet geschikt voor een thuis-BCI, maar wel voor (fundamenteel) onderzoek dat weer bruikbaar en vertaalbaar is naar een ECoG-BCI.

Onderzoek naar het decoderen vinger-bewegingen wordt voornamelijk uitgevoerd op mensen met een bewegende hand. Echter, BCIs richten zich bijna exclusief op mensen met verlamde of verloren ledematen. **Hoofdstuk 2** laat zien dat, zelfs lang na amputatie van de contralaterale arm, hand representaties en de bijbehorende elektrofysiologische eigenschappen in de sensorimotor cortex behouden blijven. De fysiologische eigenschappen van gepoogde handbewegingen in een patiënt met een verloren arm bleken vrijwel identiek aan die van uitgevoerde handbewegingen bij mensen met een gezonde hand, met een spatiale lokale verhoging van de hoge-frequentie band (HFB, 65-175 Hz) power in de hand regio en een breed verspreidde verlaging in de lage-frequentie band (LFB, 15-28Hz) power. De representaties van drie verschillende vingers (duim, wijsvinger en pink) bleken

onderscheidbaar, met voldoende neuronale informatie om met meer dan 90% classificatie-nauwkeurigheid vingerbewegingen te kunnen onderscheiden m.b.v. machine learning algoritmes op de eerste 1-3 s van de HFB respons. De onderscheidbaarheid van vinger representaties, de vroege mogelijkheid tot decoderen en voortdurende decodeerbaarheid vanaf slechts een klein (13 x 13 mm) stuk sensorimotor cortex zijn bemoedigend voor benutting in een BCI. Dit impliceert dat, ondanks mogelijke deafferatie en brein plasticiteit, motor gebieden nog altijd gebruikt kunnen worden, ver na amputatie of (mogelijk) verlamming, om neuronale prothese of communicatie apparaten aan te sturen.

In hoofdstuk 3 laten we zien dat het ontwerp (i.e. fysieke eigenschappen) en precieze chirurgische plaatsing van ECoG-elektroden op het brein voor een groot deel bepalen hoe goed de neuronale informatie van handgebaren gemeten wordt. Het meten van de meest relevante informatie vertaalt zich naar de mate en betrouwbaarheid van sturing over een BCI. Door met fMRI electrode configuraties en plaatsingen te simuleren, bevestigt onze studie dat het meeste van de handgebaar informatie gecodeerd zit in een dicht opeengepakte regio in de sensorimotor cortex. Hoewel (extra) informatie aanwezig is buiten dit informatieve gebied, kan meet-capaciteit (i.e. elektrodes in het geval van ECoG) het best ingezet worden op dit gebied. Gegeven het beperkte oppervlakte (~22mm x ~22mm) van het relevante corticale gebied moet er een balans worden gevonden tussen het aantal elektroden, de ruimte tussen elektroden en de grootte van de elektroden. Grote elektroden (tot 3mm in radius) verbeterden de decodeerbaarheid in fMRI modellen, waarschijnlijk door een toename in de signaal-tot-ruis verhouding (SNR) veroorzaakt door het middelen over meer voxels per gesimuleerde electrode. Een vergelijkbare relatie tussen electrode grootte en SNR is waarschijnlijk ook aanwezig in ECoG metingen. Over het algemeen, en in overeenstemming met de wijdverspreide aanname dat hoger resolutie metingen meer informatie verschaffen, lieten onze simulaties zien dat een hoger aantal (tot 5 x 5 elektroden) van dicht opeengepakte elektroden de meeste informatie resolutie geeft voor het decoderen van hand gebaren. Echter, vergelijkbare resultaten kunnen bereikt worden met minder elektroden (bv. 3 x 3) en een optimale inter-elektrode afstand (bv. 8mm), wat meer praktisch is in batterijduur, kosten van implanteerbare versterkers, real-time verwerking en klinische invasiviteit. Daarnaast laten onze simulaties van de elektroden-plaatsingen zien dat de configuratie en de exacte plaatsing op de cortex veel belangrijker kunnen zijn dan het hebben van meer elektroden. Deze resultaten pleiten dan ook sterk voor het gebruik van data-gedreven simulaties in fMRI (zoals beschreven in de studie) voorafgaand aan ECoG implantatie zodat de meest optimale controle over een BCI kan worden bereikt.

In de context van een communicatie-BCI voor locked-in patiënten opperen sommige onderzoekers voor het decoderen van hand gebaren (uit de gebarentaal) om zo letters, woorden en zinnen te spellen. In plaats van handgebaren stelt hoofdstuk 4 visuele inbeelding voor. Wij demonstreren dat visueel ingebeelde karakters (die je in je geestesoog ziet) gedecodeerd kunnen worden van de vroege (V1, V2, V3) visuele cortex met minimale oefening, en zo een intuïtieve manier van per-letter spelling in een BCI kunnen bieden. Wij laten zien dat langdurige visuele inbeelding (van 3, 5 en 7 seconden) niet in beter classificatie

resulteert, wat impliceert dat meer tijd om visueel in te beelden niet bijdraagt aan de kwaliteit van informatie in de vroeg visuele gebieden. Echter, langdurige inbeelding verlengde wel de decodeerbaarheid. Dit suggereert een constante neuronale activatie, welke geëxploiteerd kan worden voor BCI doeleinden. Terwijl het onderzoek zich hier specifiek richt op het decoderen van discrete karakters en het begrijpen van de temporele eigenschappen van inbeelding, hoeven dit soort ondernemingen niet beperkt te worden tot karakters. Het decoderen van complexere vormen met geavanceerde modellen kan wellicht een pad bieden waarmee patiënten informatie meer efficiënt kunnen overdragen.

De activatie in de dorsolaterale prefrontale cortex (DLPFC) kan vrijwillig gereguleerd worden, en zodanig fungeren als input voor een BCI wanneer motor representaties verzwakt of niet bruikbaar zijn. In **hoofdstuk 5** laten we zien dat men de activiteit in de DLPFC, een werkgeheugen gebied, dynamisch kan leren te reguleren binnen een korte tijd met behulp van closed-loop neurofeedback. Neurofeedback verbetert voornamelijk het vermogen om de activatie in de DLPFC na een piek terug te brengen naar de basis activatie. Hoewel speculatief, kan het reguleren van DLPFC activatie ten goede komen aan patiënten met psychiatrische en neurologische aandoeningen die gerelateerd zijn aan stoornissen van het werkgeheugen. In de context van BCIs kan vrijwillig gereguleerde DLPFC activiteit direct gebruikt worden als een input signaal. Echter, een potentieel oefen-effect (waarbij de taak automatiseert) en de daaraan gerelateerde daling in activatie in het werkgeheugen-netwerk kan resulteren in verminderde controle over een BCI. Onze resultaten suggereren dat door closed-loop feedback te verschaffen, een mogelijk oefen-effect teniet gedaan kan worden en de betrouwbaarheid van het DLPFC signaal behouden blijft.

Deze thesis onderzocht de neuronale eigenschappen van sensorimotor, visuele en werkgeheugen functies voor optimale benutting in een BCI. Samengenomen dragen deze hoofdstukken bij aan het fundament voor een thuis-BCIs met de potentie om levens te verbeteren. Elk van de individuele functies kan controle bieden over een BCI, echter, het integreren van meerdere functies in de toekomst kan leiden tot een meer complete, beter bestuurbaardere en stabielere BCI. Daarnaast pleit ik voor het gebruik van op maat gemaakt elektroden configuraties om zo optimaal de meest relevante informatie van de cortex te meten. Zulke ontwerpen zouden idealiter gedreven worden door fMRI metingen. Gegeven de huidige staat van het veld, de lopende onderzoeken en de komende initiatieven zie ik een glansrijke toekomst voor brein-computer interfaces tegemoet.

Acknowledgements / Dankwoord

So... here we are... a journey finally over after many years of research! It has been an intense ride, with "work" effortlessly spilling over into my personal life. But, dear reader, it was also a memorable time. I am grateful for having had this opportunity to pursue my research interests. There are people who helped me along the way, and those who knowingly or unknowingly made this journey more bearable. Here, I would like to take a moment to thank some of these people.

First and foremost, thank you Nick, for the opportunity to do my PhD in your group, for your trust and your guidance. I could not have wished for a more patient and experienced professor. You gave me enough freedom to (stubbornly) pursue my own ideas, make my own mistakes and learn from them; And thank you for continuing to tirelessly advise me. It took a while, but I kept my word and did finish this thesis!

And of course, Dora! I am also very grateful to you. I have no illusions that I would have never completed my PhD without your support and supervision. Thank you for welcoming me to your lab at Mayo. Being there from the very start and participating in setting it up meant a lot to me. You inspired me to reconsider my thoughts about leaving academia back in 2019: your views, your sharp mind, the efforts you make to improve scientific practices and your good advice kept me interested in the work I did. You are a great example of a scholar, and I have learned a lot from you.

Elmar(ius), Mark(us), Efraim and also Sacha! You were not only my office-mates for all these years but also my accomplices in many adventures at summer schools and trips abroad. It was fantastic to have had each one of you around. Thank you for your friendship, the daily laughs and moments of relaxation during and outside of work. Sharing the good and the bad definitely kept me sane. See you around, *et bene pendentes!*

Mariska, thank you for being such an approachable and comforting person when it felt like things were going south. Special thanks to you for helping me – particularly at the beginning of my PhD – with my writing: that must have been a tedious process, and I am grateful you took the time and effort. Martijn, you were my very first mentor in the research group in Utrecht. It is rare to find a person who enjoys discussions and confrontation as much as I do. Thank you for being there when I took my first steps in science. I appreciate your critical mind and deep knowledge of statistics. It has always been a pleasure to meet again on trips and catch up. Matthijs, thank you for occasionally sparring with me on seemingly insurmountable fMRI and methodological problems. It has been invaluable to have such an expert to consult. Erik! Thank you for your patience while working with me on several projects, for sharing your stories and experiences, and for being – besides me – the only other person who refuses to take the stairs up. Zac, you are infamous for explaining complex ideas in an even more complex way. Even so, you helped me more than you might suspect with methodological and statistical solutions. And I am glad you often joined on conferences and out-of-work adventures. Annemiek, our organizational (and charming) mastermind! Thanks

for taking care of me all these years and for being such an authentic, fun person. Mariana! It has been fun doing my PhD at the same time as you did yours. Thank you for being a good colleague, for teaching me tangerine sharing etiquette, and for keeping me in tune during my guest performances with the Gamma band. Benny, my relaxed and down-to-earth buddy. I couldn't have wished for a better person to share the burden of the UNP with. Vincent, thanks for keeping our systems up and running; I have enjoyed the ease of working with you on many of our projects. Anouk and Anouck, I very much appreciate your friendship at and outside of work. Francisco, my more recent office mate. Hang in there, a couple more years and you will be defending your PhD as well. Meron, it was always good when you were able to join us on socials! Sander, you busy man, glad to have had you around and joining us for an occasional drink. Gert, long time no see, but I remember some fun moments we had while you were in Utrecht! Wouter, so pink, yet so good. Always a pleasure. Julia, Miek, Jinne, Anna and Gio, it has been great knowing you and having you around. Also, Sandra, I am thankful that I have gotten to know you and that we kept in touch.

Melissa, you did great work as a master's student, and I am glad there was an opportunity to supervise you. Joosje en Maria, although I was not your official supervisor, I have really enjoyed supporting you in your research.

This research required many hours of working with an MRI scanner. I wish to thank the flow managers with whom I spent many afternoons and late Tuesday evenings scanning the brains of research participants. Thank you Bart, Philippe, Milan, Maxim and Maike.

Tim, thank you for including me in your neurofeedback project. And you, Nadia, for helping us and making these collaborative moments even more fun. I enjoyed working with you both and definitely didn't mind spending the extra evenings at the hospital to run tests or scan participants (and having pizza afterwards).

A large share of my PhD thesis was written during my stay in the US, and I would like to thank the people who played a role in this later stage. Kai, you are an inspiring person. I am grateful for your support and the generous feedback you provided on my paper drafts. It is always fascinating to hear about your research projects and to see the enthusiasm you have for science. Harvey, Gaby, Michael, Zeeshan, Tal and Sam. I am thankful for having you around, you have made the day-to-day more fun. Tom! Thank you for keeping me in shape with tennis and introducing me to pickleball and frisbee games. On top of that, you are one of those few people who can explain complex concepts in an intelligible way, can cook an amazing meal, and are probably the only person who has read this thesis entirely. Thanks! Dorien, I am happy we had a couple of months overlap in the US so that we got to hang out, play volleyball and even live in same house for a bit! On the social side of Rochester MN, thank you Vladimir, Filip, Tim, Vaclav, Gian-Marco, Louis, Amy, Kamila, Petr, Nunzia, Sylvia, Delphine, Ayssa, Margherita (and more recent, Nick, Jackie, Ellen, Giuseppe, Malin, Gabri, Patri, Diederik, Daan and Jose) for making the long Midwestern winters bearable and the summers fun!

I consider myself lucky to have a great many beautiful people in my life who knowingly or unknowingly aided me during my PhD. Simply by being who you are :) You allowed me to relax, recharge, see things from a different perspective or just have plain fun.

Om maar te beginnen met jullie rakkers uit Leiden: Thomas, Alex en Benjamin! Isabel, Mikel, Marc en Melanie! Samen bootje varen, feestjes, weekend tripjes en velerlei andere avonturen. En ook jullie, Ties en Joni, blij dat ik jullie heb leren kennen! Bedankt! Mijn collegecrew: Joram, Merel, Hanne en Jonne! Van de collegebanken in het Gorleaus tot het hier en nu. Fijn dat jullie er zijn en dat we elkaar nog altijd zien, ik hoop dat dat nog lang zo blijft! Hetairoi, lieve Asopos-genoten, in het bijzonder Goof en Nico! Bedankt voor jullie vriendschap! Marika, Johan en Loes, ik ben blij dat jullie er zijn, en bedankt voor alle leuke tijden samen. De vrije jongens en meisjes uit Amsterdam: Sven, Federica, Ruud, Frank, Herman, Sanneke en Pieteke. Jullie lieten me zomaar even zien hoe sommige dingen in het leven ook anders kunnen :) Dat we nog veel mogen beleven, ik dank jullie!

Karlijn, fijn dat je al zo lang in mijn leven bent, dat waardeer ik en onze gesprekken doen me altijd glunderen. Plus jij bent degene die me ooit op het neurowetenschappelijke pad hebt gezet! Sanne, bedankt voor de vele avonturen, je bent een mooi mens. Pelin, bedankt voor de leuke tijden tijdens en na onze studie. Rosa!, bedankt voor je gezelschap en alle goeie gesprekken samen! Mijn homies van Orgie-D uit de beginjaren van mijn PhD, het was altijd fijn om na een lange dag werken op het ziekenhuis thuis te komen en zoveel enthousiasme en leven te vinden (en meer dan eens een bord eten). Emilie, Sanne, Bram, Sietse, Alex, Smiet, Sara, Edwin, Henric, Marit, Char, Marianne, Job, Margriet, Marion, Niels, Nick en Sebastiaan, bedankt voor die tijd! Marc, en Paultje, bedankt voor de vriendschap over de vele jaren. Niek, Saskia en Jeff, altijd mooi om jullie weer te zien! De jongens uit Roosendaal, oud oud oud huisgenoten en vertrouwde karakters waarmee ik nog altijd bourgondisch kan genieten en mezelf kan zijn. Bedankt Eddie, Mario, Pan, Dave, Martijn, Ewout, Dion, Mike, Tom, Jorde en Maiky.

Lieve familie, paake (Hans) en moeke (Sybeline), Tom, Eefje, Lisanne en Bart. Bedankt dat jullie er altijd voor mij zijn geweest en me op de een of andere manier hier hebben gebracht. En mijn uitbundige neefjes, Bram, Lars en Dex, jullie zijn altijd een feest!

En ten slotte jij, canım, bedankt, voor wie je bent, je steun en je geduld. Het leven is simpelweg leuker met jou en ik kijk uit naar al dat nog komen gaat.

Publications

Van den Boom, M., Miller, K.J., Gregg, N.M., Valencia, G.O., Lee, K.H., Richner, T.J., Ramsey, N.F., Worrell, G.A. and Hermes, D., 2021. Typical somatomotor physiology of the hand is preserved in a patient with an amputated arm: An ECoG case study. *NeuroImage: Clinical*, *31*, p.102728.

Van den Boom, M.A., Miller, K.J., Ramsey, N.F. and Hermes, D., 2021. Functional MRI based simulations of ECoG grid configurations for optimal measurement of spatially distributed hand-gesture information. *Journal of neural engineering*, *18*(2), p.026013.

Van den Boom, M.A., Vansteensel, M.J., Koppeschaar, M.I., Raemaekers, M.A. and Ramsey, N.F., 2019. Towards an intuitive communication-BCI: decoding visually imagined characters from the early visual cortex using high-field fMRI. *Biomedical physics & engineering express*, *5*(5), p.055001.

Van den Boom, M.A., Jansma, J.M. and Ramsey, N.F., 2018. Rapid acquisition of dynamic control over DLPFC using real-time fMRI feedback. *European Neuropsychopharmacology*, *28*(11), pp.1194-1205.

Vansteensel, M.J., Pels, E.G., Bleichner, M.G., Branco, M.P., Denison, T., Freudenburg, Z.V., Gosselaar, P., Leinders, S., Ottens, T.H., **Van den Boom, M.A.** and Van Rijen, P.C., 2016. Fully implanted brain–computer interface in a locked-in patient with ALS. *New England Journal of Medicine*, *375*(21), pp.2060-2066.

Freudenburg, Z., Kohneshin, K., Aarnoutse, E., Vansteensel, M., Branco, M., Leinders, S., **Van den Boom, M.**, Pels, E.G. and Ramsey, N., 2021. The dorsolateral pre-frontal cortex bi-polar error-related potential in a locked-in patient implanted with a daily use brain–computer interface. *Control Theory and Technology*, *19*(4), pp.444-454.

Vansteensel, M.J., Pels, E.G.M., Branco, M.P., Denison, T., Freudenburg, Z.V., Leinders, S., **Van den Boom, M.A.**, Aarnoutse, E.J. and Ramsey, N.F., 2017. Fully implanted brain signal recording device for communication in severe paralysis reveals feasibility of chronic home use of neuronal activity. *European Neuropsychopharmacology*, *27*, p.S556.

Stevenson, C.E., Alberto, R.A., V**an den Boom, M.A.** and de Boeck, P.A., 2014. Visual relations children find easy and difficult to process in figural analogies. *Frontiers in Psychology*, *5*, p.827.

Conference abstracts

Van den Boom, M.A., Van Blooijs, D., Gregg, N.M., Ojeda Valencia, G., Lundstrom, B.N., Worrell, G.A., Van der Aar, J.F., Huiskamp, G.J.M., Miller, K.J., Leijten, F.S.S. and Hermes, D. A validated BIDS app for the automated detection of early evoked responses and mapping of connectivity in IEEG. *Society for Neuroscience Meeting 2021*

Van den Boom, M.A., Vermaas, M., Aarnoutse, E.J., Leinders, S., Pels, E.G.M., Freudenburg, Z.V., Branco, M.P., Vansteensel, M.J. and Ramsey, N.F. Utrecht Neuroprosthesis: From brain signal to independent control. *The 7th Graz Brain-Computer Interface Conference 2017*

Van den Boom, M.A., Pels, E.G.M, Branco, M.P., Aarnoutse, E.J., Leinders, S., Freudenburg, Z.V., Vansteensel, M.J. and Ramsey, N.F. DLPFC activity as a control signal in a fully implanted Brain Computer Interface. *Annual Meeting of the Organization for Human Brain Mapping 2017*

Van den Boom, M.A., Vansteensel, M.J., Raemaekers, M. and Ramsey, N.F. Visual mental imagery in high-field fMRI. *Society for Neuroscience Meeting 2016*

Van den Boom, M.A., Vansteensel, M.J. and Ramsey, N.F. Decoding visual mental imagined symbols using high-field fMRI. *Annual Meeting of the Organization for Human Brain Mapping 2016*

Van den Boom, M.A., Jansma, J.M. and Ramsey, N.F. Enhanced working memory activity shifting through fMRI neurofeedback. *BCI society - 6th International BCI meeting*

Van den Boom, M.A., Jansma, J.M. and Ramsey, N.F. Regulation of working memory activity through fMRI neurofeedback. *Society for Neuroscience Meeting 2015*

Vansteensel, M.J., Pels, E.G.M., Branco, M.P., Denison, T., Freudenburg, Z.V., Leinders, S., **Van den Boom, M.A.**, Aarnoutse, E.J. amd Ramsey, N.F. Fully implanted brain signal recording device for communication in severe paralysis reveals feasibility of chronic home use of neuronal activity. *30th ECNP Congress of Applied and Translational Neuroscience*

Leinders, S., Luppi, J., Branco, M.P., Freudenburg, Z.V., Pels, E.G.M., **Van den Boom, M.A.**, Aarnoutse, E.J., Vansteensel, M. and Ramsey, N.F. Case Study: Eye Movement Related Motor Activity Overlaps with Hand-Knob Area in Late Stage ALS. *BCI society - 7th International BCI meeting*

Curriculum Vitae

Max van den boom was born on August 17th, 1984, in Breda, The Netherlands. He grew up in Roosendaal and later moved to Breda to obtain a Bachelor's degree in Computer Science at Avans University. After spending several years working abroad, he continued his education at Leiden University. He received a Bachelor of Science degree in Psychology in 2012 and a Research Master of Science degree in Cognitive Neuroscience in 2014. Immediately after, he embarked on a PhD program at the University Medical Center Utrecht (Utrecht University) in the research group of Prof. dr. Nick Ramsey. He completed his PhD thesis at Mayo Clinic (Rochester, MN, USA) as part of the Multimodal Neuroimaging Lab of dr. Dora Hermes, where he is currently working as a research fellow.